ANNUAL REPORT 1996

Department
of
Optoelectronics

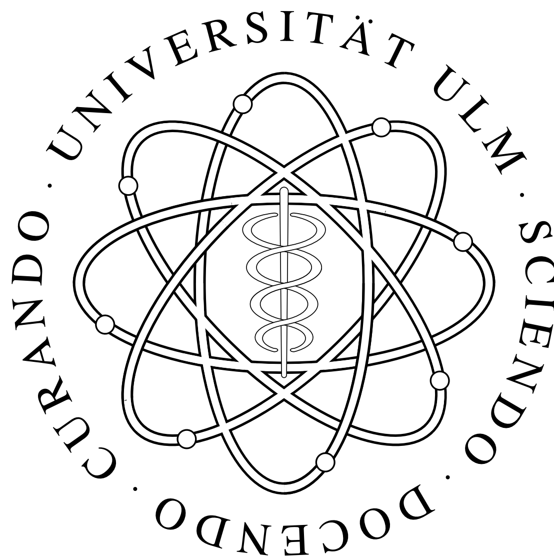

University of Ulm

Contents

Strengthening Competitiveness 1

Articles **3**

GSMBE of SC-InGaAsP MQW lasers 3

Long-Wavelength Vertical-Cavity Surface-Emitting Lasers 8

Wafer Fusion for 1.55 μm VCSELs 14

Improvement of the Operation Characteristics of VCSELs by Carbon Doping 18

Carbon Doped 850 nm Wavelength GaAs VCSELs 22

High Efficiency Wide Temperature Range GaAs VCSELs 26

Improvement of Oxide-Confined VCSELs for High Frequency Applications 31

Broad-Area High-Power Top Surface Emitting Laser Diodes 36

Measurement of Ultrafast Oscillations in VCSELs after Pulse Perturbation 42

Bias-Free Data Transmission Using Single-Mode GaAs VCSELs 46

A Model of an Optical Communication System 50

Microcavity Light Emitting Diodes 54

Thermal Analysis in High-Power Semiconductor Laser Amplifiers 59

High-Power InGaAs/AlGaAs Traveling-Wave Amplifiers 64

Fabrication and Mounting of Broad-Area Laser Diodes for High-Power Operation . . . 69

GaN-Based Light Emitting Diodes Grown by Low Pressure MOVPE 75

Homoepitaxial GaN Films and LEDs 79

Electrical and Optical Properties of GaN Light Emitting Diodes 86

Fabrication of GaN LEDs 92

Chemically-assisted ion-beam etching of GaN 96

Lists of Publications **99**

Ph.D. Theses 99

Diploma Theses and Semester Projects 100

Talks and Seminars 102

Publications and Conference Contributions 104

Department of Optoelectronics University of Ulm

Albert-Einstein-Allee 45, D-89069 Ulm, Germany
Fax: +49–731/502–6049
Phone: +49–731/502–

Head of Department:

Prof. Dr.	Karl Joachim Ebeling	–6051	karl.ebeling@e-technik.uni-ulm.de

Assistant Head of Department:

Prof. Dr.	Peter Unger	–6054	unger@sunrise.e-technik.uni-ulm.de

Cleanroom Management:

Dr.-Ing.	Jürgen Mähnß	–6053	juergen.maehnss@e-technik.uni-ulm.de

Senior Research Assistant:

Dr.-Ing.	Rainer Michalzik	–6048	rainer.michalzik@e-technik.uni-ulm.de

Secretaries:

	Christine Bunk	–6050	karl.ebeling@e-technik.uni-ulm.de
	Sükran Kilic	–6059	

Research Staff:

Dipl.-Phys.	Hin Yiu Anthony Chung	–6043	hin-yin.chung@e-technik.uni-ulm.de
M.S.	Zheng Dai	–6044	zheng.dai@e-technik.uni-ulm.de
Dipl.-Ing.	Franz Eberhard	–6039	franz.eberhard@e-technik.uni-ulm.de
Dipl.-Ing.	Martin Grabherr	–6036	martin.grabherr@e-technik.uni-ulm.de
Dipl.-Ing.	Jörg Heerlein	–6046	joerg.heerlein@e-technik.uni-ulm.de
Dipl.-Phys.	Roland Jäger	–6040	roland.jaeger@e-technik.uni-ulm.de
Dipl.-Ing.	Jürgen Joos	–6035	juergen.joos@e-technik.uni-ulm.de
Dipl.-Phys.	Günter Jost	–6046	guenter.jost@e-technik.uni-ulm.de
Dipl.-Phys.	Christian Jung	–6036	christian.jung@e-technik.uni-ulm.de
Dr.rer.nat.	Markus Kamp	–6454	kamp@sunrise.e-technik.uni-ulm.de
Dipl.-Ing.	Roger King	–6035	roger.king@e-technik.uni-ulm.de
Dipl.-Ing.	Christoph Kirchner	–6040	christoph.kirchner@e-technik.uni-ulm.de
Dipl.-Phys.	Markus Mayer	–6452	markus.mayer@e-technik.uni-ulm.de
Dipl.-Phys.	Arthur Pelzmann	–6452	arthur.pelzmann@e-technik.uni-ulm.de
Dipl.-Phys.	Gernot Reiner	–6048	gernot.reiner@e-technik.uni-ulm.de
Dipl.-Phys.	Markus Schauler	–6039	markus.schauler@e-technik.uni-ulm.de
Dipl.-Ing.	Wolfgang Schmid	–6044	wolfgang.schmid@e-technik.uni-ulm.de
Dipl.-Phys.	Peter Schnitzer	–6037	peter.schnitzer@e-technik.uni-ulm.de
Dr.-Ing.	Georgi Stareev	–6043	georgi.stareev@e-technik.uni-ulm.de
Dipl.-Ing.	Dirck Sowada	–6043	dirck.sowada@e-technik.uni-ulm.de
Dipl.-Phys.	Bernhard Weigl	–6036	bernhard.weigl@e-technik.uni-ulm.de
Dipl.-Ing.	Dieter Wiedenmann	–6037	dieter.wiedenmann@e-technik.uni-ulm.de

Technical Staff:

	Margit Kohler	–6041
	Sophie Pfetsch	–6041
	Susanne Menzel	–6041
	Rudolf Rösch	–6038
	Josef Theisz	–6030

Strengthening Competitiveness

During 1996 research activities in the Department have been continuing in the areas vertical-cavity surface-emitting laser diodes (VCSELs), optical interconnect systems, GaN based wide bandgap semiconductor devices, and high-power laser diodes. Considerable progress has been achieved. Selectively oxidized VCSELs emitting around 850 nm wavelength show record high 57 % electrical-to-optical conversion efficiency and unexceeded 180 mW at 980 nm continuous wave output power. High performance VCSELs have been employed in fiber based optical busses to demonstrate for the first time bias-free 1 Gbit/s data transmission. For 1.5 μm long wavelength VCSELs wafer fusion has been successfully implemented and using gas source MBE for crystal growth, state-of-the-art strain compensated broad area edge emitting InGaAsP laser diodes were fabricated. Steady advances are observed in high-power laser diodes, where optical amplifiers now reach more than 2 W continuous wave output power with well controlled beam profile. Work on GaN has been more demanding than originally expected. Nevertheless we were able to obtain our first blue light emitting diodes both with MBE and MOVPE grown material after carefully solving the p-doping problem and using dry etching for defining contact geometries. More details on various research projects are to be found in the following articles.

There have been 12 semester projects and 15 diploma theses completed in the Department. Three members of the Department, Thomas Kummetz, Markus Sickmöller and Rainer Michalzik received their Ph.D. degrees. Thomas and Markus (both from Prof. Kowalsky's former group, now at the Technical University of Braunschweig) have now interesting jobs in industry. Rainer has a permanent position in the Department taking care of its financial affairs aside from his teaching and VCSEL research activities. Eberhard Zeeb, who got his promotion last year, now was awarded the Ph.D. Dissertation Prize of the Ulmer Universitätsgesellschaft. Finally, Torsten Wipiejewski left us for joining Siemens AG at Berlin being involved in optical interconnects.

The Department further intensified the already close cooperation with industry. Daimler-Benz Research and German Telekom have supported three Ph.D. students. A new contract was established with Siemens AG. In the latter case new experience has been gained in trying to transfer an extremely successful research device, namely the VCSEL, to reliable mass production. These important efforts will be extended in the future.

Apart from industry the research projects of the Department are generously supported by the German Science Foundation, the Federal Ministry of Research and Technology, the ACTS and MEL-ARI Programs of the European Community, the Volkswagenstiftung, and a special research program of the Government of Baden-Württemberg, all of which is gratefully acknowledged. The Department was happy to receive again so many distinguished visitors from abroad. Bart van Zeghbroeck, Colorado State University, spent several weeks with us as a guest professor supporting our GaN work.

In late spring Markus Kamp co-organized the first European GaN Workshop at Rigi-Kulm Switzerland. This inspiring meeting was the start of a new conference series now to be held every year at another place in Europe. Quite generally, life in the Department in 1996 has to be characterized by lots of desired or undesired traveling for visiting conferences or attending

national and international joint research project meetings. Unfortunately, due to his commitments as one of the Vice-Presidents of the University, the Head of the Department has maybe not been able to take part in traveling and to support research as much as he would like to.

Research achievements and activities show that there is a prospective basis to look optimistically into the future.

K.J. Ebeling, January 1997

Gas source molecular beam epitaxy of strain compensated InGaAsP MQW laser diodes emitting at 1.5 μm

Hin Yiu Anthony Chung, Dirck Sowada, Georgi Stareev

We report on the growth investigations and results of strain compensated InGaAsP multiple quantum well (MQW) laser diodes emitting at 1.5 μm. Growth conditions for bulk InGaAsP layers and strain compensated (SC) InGaAsP MQW structures with gas source molecular beam epitaxy are discussed. Separate confinement heterostructure laser diodes with SC-InGaAsP MQWs have been grown and processed into broad-area laser diodes. A threshold current density of 190 Acm^{-2} per quantum well and a characteristic temperature of 50 K are obtained.

1. Introduction

In the past few years, great interest has been paid to the application of strain compensated multiple quantum wells as the active layer of lasers operating at 1.5 μm. It is believed that strain compensated MQWs are attractive for high frequency laser modulation because the valence band discontinuity between barrier and well is expected to decrease. By using strain compensation technique, the number of strained quantum wells in the active region of the laser can be increased freely without having to face with the problem of crystal relaxation. This enables a greater flexibility in optimizing the laser performance. In this paper, we report the growth of lattice matched InGaAsP bulk layers and strain compensated InGaAsP MQWs by gas source molecular beam epitaxy (GSMBE). The layers were characterized by X-ray diffraction and photoluminesence (PL). Laser diodes containing strain compensated InGaAsP MQWs were grown and processed into broad area laser bars. The performances of the laser diodes with respect to threshold current density and characteristical temperature have been investigated.

2. Epitaxial growth

The growth of epitaxial layers was carried out in a Riber 32 R&D Gas source MBE system using elemental In and Ga as the group-III source materials. Pure AsH_3 and PH_3, precracked at 900 °C, were used as the group-V precursors. Be and Si were used as the p- and n-type dopants. All layers were grown on (100) InP substrates, 2° off towards the nearest $(1\bar{1}0)$ direction. The substrate temperature during growth was 500 °C for all the layers and was measured by an Accufiber pyrometer.

A) Bulk single layers

One of the prerequisites of producing laser diodes with good performances in the 1.5 μm regime is the ability to grow InP layers and InGaAsP layers with various compositions in high quality. Therefore bulk InP and InGaAsP layers were first optimized. The bulk InP layers are

grown at a rate of 0.5 μmh^{-1}. The beam equivalent pressure of precracked PH_3 is chosen to be 1.10$\times$10^{-5}mbar. All InP layers show mirror-like surfaces and have an unintentionally As-incooperation of less than $\pm$200 ppm. Hall measurements indicate that all the InP layers have a background n-type doping of around 5$\times$10^{14}cm^{-3} and a electron-mobility of around 5000 cm^{2}V^{-1}s^{-1} at room temperature. Bulk InGaAsP layers with various compositions, lattice-matched to InP, were also grown. The growth rates are between 1 μmh^{-1} and 0.7 μmh^{-1}. In Fig. 1 and Fig. 2 the corresponding flux ratios for the quarternary layers are shown. The layers were characterised by x-ray diffraction and photoluminesence (PL). The lattice-matchings of the quarternary layers are reproducible down to $\pm$400 ppm. All layers show strong room temperature PL signals. In the case of InGaAsP layers with a band gap energy corresponding to a wavelength of 1.3 μm, a PL peak with a full width half maximum (FWHM) of 55 meV is observed at room temperature. At 10 K the FWHM of the PL peak reduces to 11 meV. These results indicated that the InGaAsP layers grown by our GSMBE are of considerably high quality.

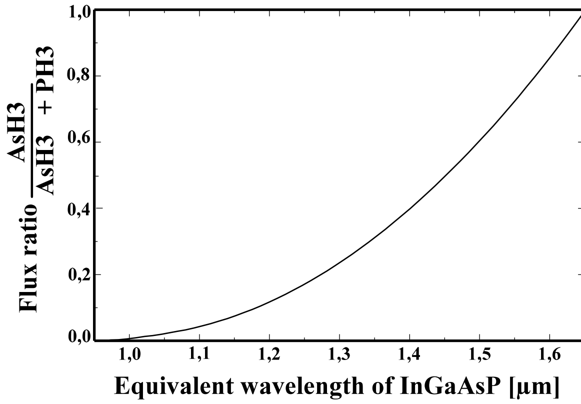

Fig. 1. Group V flux ratio for the growth of InGaAsP quaternary epilayers.

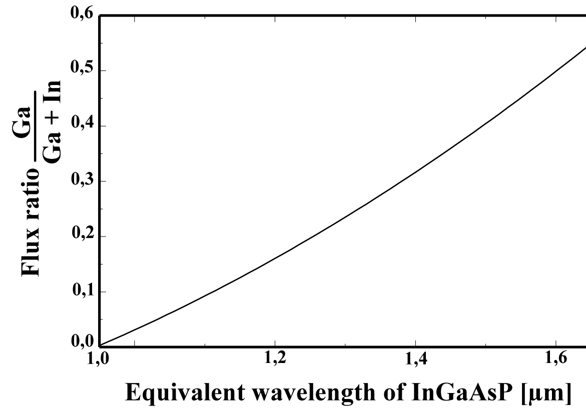

Fig. 2. Group III flux ratio for the growth of InGaAsP quaternary epilayers.

B) Strain compensated MQWs

The MQW structures we investigated consist of four 7.5 nm $In_{0.71}Ga_{0.29}As_{0.82}P_{0.18}$ compressively strained quantum wells (QWs). The strain in each QW is about 1.3 %. The QWs are seperated by $In_{0.71}Ga_{0.29}As_{0.40}P_{0.60}$ quantum barriers (QBs) which are under tensile strain. The thickness of the QBs is adjusted so that a zero net-strain is achieved. In Fig. 3, X-ray rocking curve of a MQW structure under nearly zero net-strain is shown. Sharp satellite peaks located symmetrically on the two sides of the InP substrate peak indicate the high crystal quality of the MQWs. In Fig. 4, PL spectra of a strain compensated MQW structure are shown. At 300 K, a sharp PL peak with a FWHM of 52 meV is obtained. At 10 K, the FWHM of the PL peak reduces to 21 meV.

C) Laser structure: growth and processing

The laser structures we have grown consist of a 1 μm thick n-type InP buffer, a 100 nm InGaAsP (λ_{gap}=1.18 μm) wave-guiding layer, four periods strain compensated InGaAsP MQW, a 1 μm

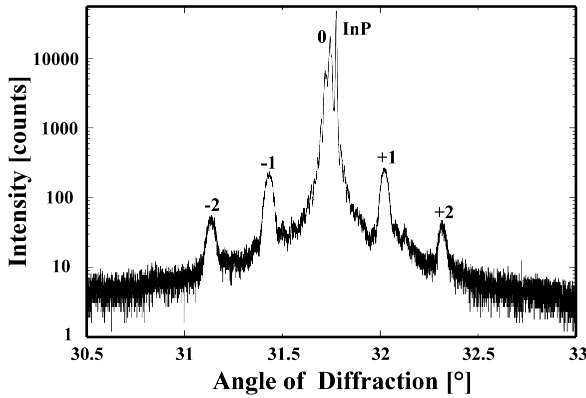

Fig. 3. X-ray rocking curve of a strain compensated MQWs with 4 periods of 7.5 nm compressively strained(1.36 %) InGaAsP QW and 11 nm tensily strained (1 %) InGaAsP QB.

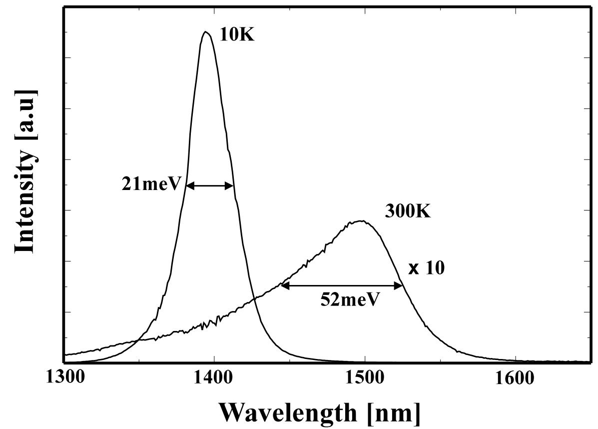

Fig. 4. PL-spectral of 4 periods of strain compensated MQWs measured at room temperature and 10 K.

thick p-type InP cladding and a heavily p-type doped InGaAs contact layer. The structure of the epilayers in the laser is shown in Fig. 5. After the epitaxy, Ti/Pt/Au p-contacts were evaporated onto the top of the samples followed by a lift-off step. After the metal patterning, stripes with widths of 10 μm to 50 μm were formed by wet chemical etching. The etch-process was stopped immediately after the p-type cladding was reached. A Ge/Ni/Au layer was evaporated onto the bottom of the sample as n-side contact. Finally, the sample was cleaved into laser diodes with cavity lengths of 400 μm to 1000 μm.

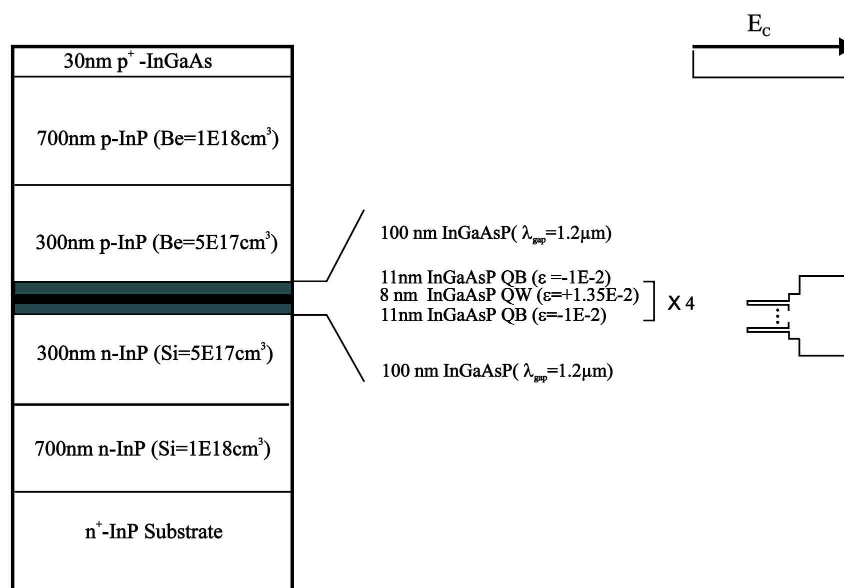

Fig. 5. Layer structure and the corresponding conducting band offsets of the SC-MQW laser diode.

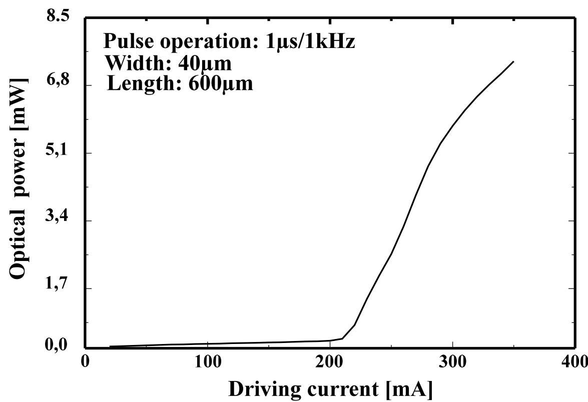

Fig. 6. Output power vs current characteristic of a SC-MQW laser diode.

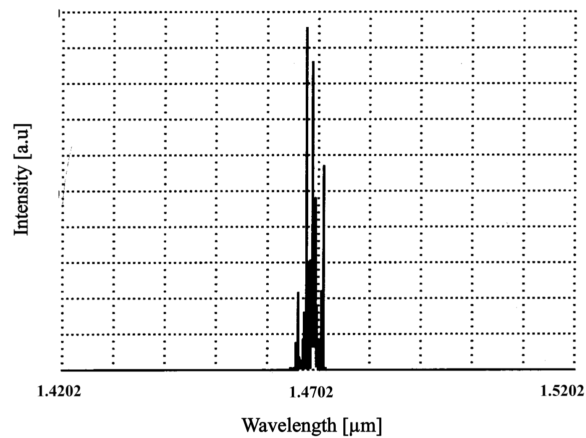

Fig. 7. Optical spectrum of a SC-MQW laser diode.

3. Laser performance

In Fig 6, the power vs current characteristic of a 40 μm wide and 600 μm long laser bar is shown. The laser was operated under pulsed excitation (1 μs pulse width, 1 kHz repetition rate) at room temperature. The emission spectrum of the laser bar, driven at 1.4 times the threshold current, is shown in Fig. 7. Here we observe that the emission wavelength of the laser diode is at 1.47 μm. The threshold current densities, j_{th}, for laser bars with different widths and lengths were also measured and are shown in Fig. 8. Laser bars with a width of 50 μm are found to have the lowest threshold current densities amount all the samples. For laser diodes with a width of 50 μm and an infinitely long cavity, a threshold current density, j_{th}, of 190 Acm^{-2} per QW was estimated. this relatively low value for j_{th} indicates that our laser structures are of high quality. In order to determine the temperature sensitivity of the laser bars, the theshold current density of a laser with a width of 50 μm and a length of 600 μm was measured as a function of ambient temperature and is shown in Fig. 9. From the slope of the graph, a characteristical temperature, T_0, of 50 K is obtained.

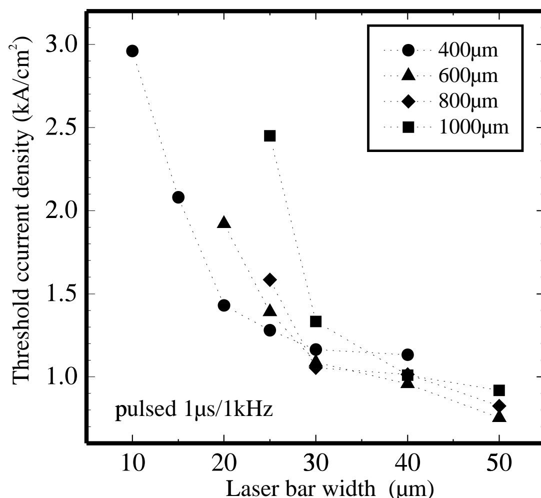

Fig. 8. Threshold current densities, j_{th}, for laser bars with different widths and lengths.

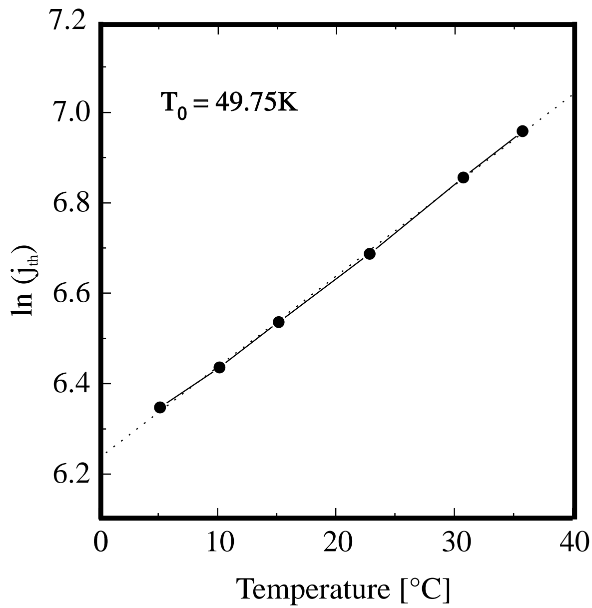

Fig. 9. Threshold current density of a laser with a width of 50 μm and a length of 600 μm as a function of ambiant temperature.

4. Conclusion

High quality InP, InGaAsP and strain compensated InGaAsP MQWs are sucessfully grown by GSMBE. Broad area laser diodes with separate confinement strain compensated InGaAsP MQWs as the active region were grown and processed. A j_{th} of 190 Acm^{-2} per QW and a T_0 of 50 K is obtained which indicate that our laser diodes are of good quality.

High-Reflecting Mirrors and Current Confinement by wet Oxidation for Long-Wavelength VCSELs

Dirck Sowada, Georgi Stareev, Hin Yiu Anthony Chung, Torsten Wipiejewski

Vertical-cavity surface-emitting lasers operating in the 1.3 μm and 1.5 μm wavelength range are highly attractive for telecommunication applications. However, they are far less well developed than devices operating at shorter wavelengths. Long growth times are required for highly-reflecting epitaxial mirrors. In this report we discuss dielectric Al_2O_3/α*-Si mirrors and enhanced oxidized* $In_{0.52}Al_{0.48}As$ *layers on InP substrates. Reflection measurements of evaporated and sputtered* Al_2O_3/α*-Si mirrors show good agreement with simulated results. We can measure a maximum reflectivity of about 99% for 5 pairs DBR at resonance wavelength of 1.55 μm. The measured absorption coefficient is better than* $1050\,cm^{-1}$ *at 1.55 μm.*

The enhanced native oxidation of $In_{0.52}Al_{0.48}As$ *layers with thin AlAs monolayers can increase the oxidation rates of mirror structures. The oxide shows no volume shrinkage but interfacial porosities between semiconductor and oxide. The refractive index of the oxide is n=1.7 at 1.3 μm and n=1.57 at 1.55 μm, the absorption coefficient is negligible.*

1. Introduction

Vertical-cavity surface-emitting lasers (VCSELs) have generated a lot of interest for optical systems due to their surface-emitting nature. Their benefits include simple integration into 2-D arrays, on-wafer testing, and efficient fiber coupling. The first near room-temperature (14 °C) cw operation of an electrically pumped VCSEL at 1.3 μm [1] and low-threshold-current room-temperature pulsed lasing at 1.5 μm [2] have been achieved recently. Both structures employ two dielectric reflectors, which require removal of the substrate. Recently, very encouraging results have been reported using wafer fusion of AlGaAs-based Bragg reflectors and InP-based active material. Room-temperature continuous-wave operation of 1.54 μm double-fused vertical-cavity lasers was demonstrated with a minimum threshold current of 2.3 mA and highest cw operating temperature of 33 °C [3, 4].

There are several requirements for distributed Bragg reflectors (DBRs) used in VCSELs. First of all they must have a very high reflectivity (above 99%) to satisfy the laser threshold condition with the small optical gain of the extremely thin active material in quantum well structures. The reflectors must also exhibit a good thermal conductivity to provide heat sinking of the active region. This property is required at least for one of the two laser mirrors. Furthermore, the DBR should be electrically conductive, because the injection of laser current through the mirror simplifies the laser structure and the fabrication process. With no conductivity lateral current injection is required which is harder to achieve and can cause problems like current crowding at the edge of the active area.

In this report we discuss the enhanced oxidation of InAlAs/InP mirrors with thin AlAs-Layers on InP-substrates and dielectric Al_2O_3/α-Si mirrors for long-wavelength VCSELs.

2. Enhanced Oxidation of $In_xAl_{1-x}As$ layers

A relatively simple technique called native oxidation ("wet" chemical oxidation via H_2O vapor + N_2) was proposed recently for the preparation of index-guided laser structures on GaAs substrates [5]. Wet oxidation of InAlAs lattice matched to InP was employed to fabricate long wavelength InAlAs-InP-InGaAsP gain-guided native-oxide-defined stripe-geometry laser diodes [6]. If the Al content x of the confining layers is high enough ($x > 0.5$), the layer can be transformed into a stable native metal-oxide by heating in water vapour. This simple technique for current blocking and optical confinement offers a promising alternative to buried heterostructure lasers based on multiple epitaxial growth.

In our experiments we used epitaxial (MBE) grown $In_{0.52}Al_{0.48}As$ layers of different thicknesses lattice matched to InP-substrate. We determine the vertical and lateral oxidation rates by looking at the oxidation fronts of cleaved facets in a scanning electron microscope (SEM).

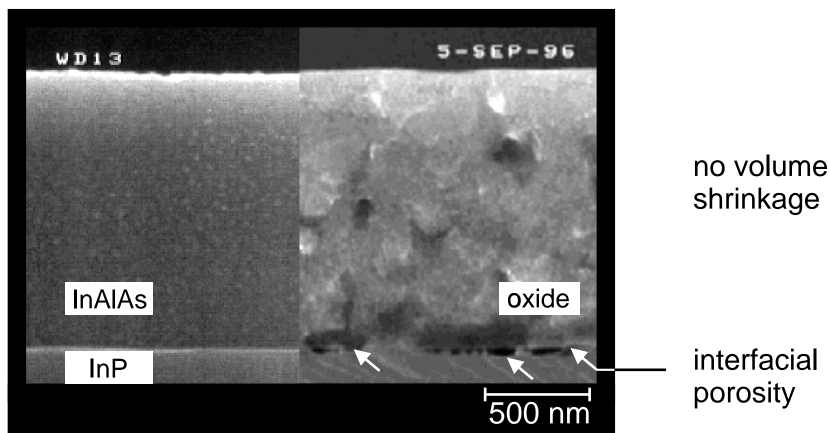

Fig. 1. SEM image of a 1.3 μm thick $In_{0.52}Al_{0.48}As$ layer before (left) and after (right) oxidation. The image shows no volume shrinkage but interfacial porosity between semiconductor and oxide.

Fig. 1 shows the SEM image of a 1.3 μm-thick InAlAs layer before oxidation (left side) and after oxidation (right side). After oxidation the oxide-layer has nearly the same volume as the InAlAs-layer. We assume no shrinkage. The oxide is essentially amorphous and shows small crystalline granules with diameters of about 4–8 nm. Because of the different lattice parameters of semiconductor and oxide, the strain induced interfacial porosities with diameters up to 150 nm.

At fixed Al content the oxidation rates increases markedly with the temperature suggesting an exponential law. This is confirmed by the plot of the Arrhenius law

$$r = r_0 \exp\left(\frac{-E_a}{kT}\right) \tag{1}$$

as a function of inverse temperature where E_a is the activation energy. The data fit a straight line and gives a r_0 value of 162.2×10^9 nm/h and an activation energy of 1.326 eV. A 120 nm thick InAlAs-layer shows at 520 °C an oxidation rate of about 600 nm/h. In comparison a 27 nm thick AlAs layer (x=100%) has a 48 times larger r_0 value of 7.75×10^9 μm/h. The measured oxidation depth as a function of the time, for oxidation conducted between 480 °C and 540 °C, is nearly linear. Refractive indices of n=1.7±0.02 at 1300 nm and n=1.57±0.02 nm at 1550 nm wavelength, respectively, were determined in our oxidized InAlAs layers by spectroscopy.

To accelarate the oxidation rate of $\lambda/4$ thick InAlAs layers in Bragg reflectors for VCSELs we tested the oxidation of thin AlAs monolayer between two $\lambda/8$ InAlAs layers (Fig. 2). The fast

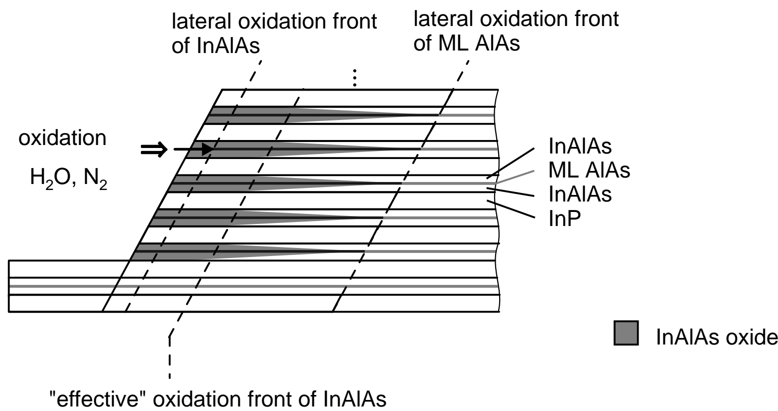

Fig. 2. Model of the lateral and vertical oxidation rate in InAlAs/InP DBRs including thin monolayers of AlAs demonstrated near the side wall of an etched stripe structure.

lateral oxidation rate of the film should also accelarate the lateral oxidation rate of the thick InAlAs layer with lower Al content because of the additional vertical rate. So the effective oxidation rate of InAlAs is much greater than the lateral oxidation rate. The oxidation time for the total structure depends on the mesa diameter and the InAlAs and AlAs layer thicknesses. Thin layers of lattice mismatched AlAs induced a strong strain but with optimized growth conditions and strain compensated InAlAs/AlAs/InAlAs structures the strain produce no crystal defects!

The ratio between the lateral oxidation rate of AlAs monolayers and InAlAs shows Fig. 3. At a temperature of 480 °C InAlAs with 15 monolayers (ML) of AlAs show a 3.3 times larger oxidation rate than $\lambda/4$ thick InAlAs. The ratio decreases with decreasing AlAs layer thickness and increasing temperature. Fig. 4 shows the absolute lateral oxidation over inverse temperature. In this view the rate of InAlAs shows a good agreement with the Arrhenius law (1). The curve and the porosity is suggested by the linear reaction kinetics of the oxidation process by allowing gas-phase transport of reactants through the layers. The reason for smaller oxidation rates of thick AlAs layers at high temperature could be a saturation effect.

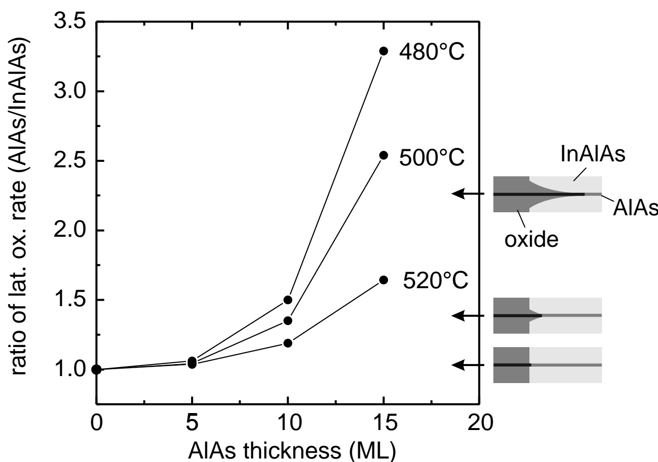

Fig. 3. Ratio of the lateral oxidation rates between monolayers AlAs and $\lambda/8$ thick InAlAs layers as a function of temperature.

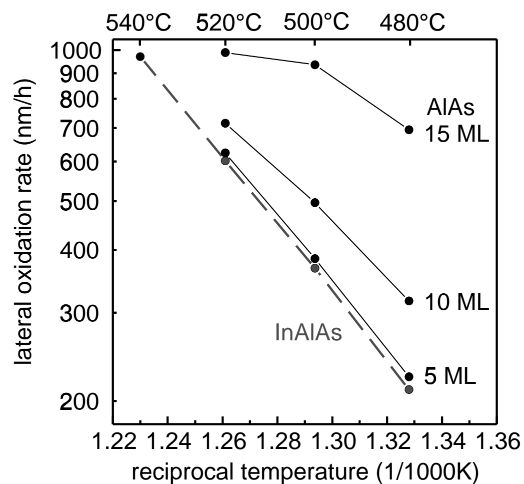

Fig. 4. Plot of absolute oxidation rates of thin AlAs layers embeded in $\lambda/8$ InAlAs layers.

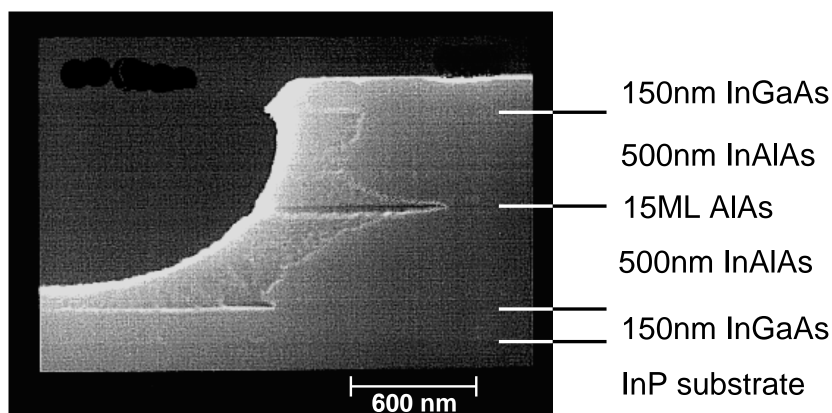

Fig. 5. Scanning electron microscope image of an oxidized 1 μm thick $In_{0.52}Al_{0.48}As$ layer with a 15 ML AlAs layer. The oxidation rates at the interfaces are increased.

The Fig. 5 shows a SEM image of the cleaved facet of a 1 μm thick InAlAs layer with a 15 monolayers thick AlAs layer at 0.5 μm. The oxidation conditions are 500 °C, 60 l/h nitrogen flow rate and 70 min oxidation time. Because of the interfacial porosities we assume a 2-15% increased oxidation rate at both InAlAs/InGaAs interfaces.

In future work we will grow InAlAs/InP DBRs (1 to 5 pairs). With oxidation of the InAlAs it should be possible to fabricate VCSELs mirrors with a reflectivity up to 99.5%.

3. Dielectric Al_2O_3/α-Si Mirrors

For top mirrors in VCSELs we investigated the materials Al_2O_3 and amorphous Si. The advantage of these materials are the nearly same coefficient of thermal expansion to InP substrate and a high index contrast. In former times we explored the MgO/α-Si material system, but MgO is strong hydrophil and so it's difficult to evaporate and preserve the mirror. Additionally there is a memory effect in the coating chamber.

In our Bragg reflectors we used e-beam-evaporated and sputtered material. Deposition conditions are a pressure of less than 5×10^{-6} torr and low evaporation rates of 0.2 to 0.5 nm/s for e-beam-evaporation and sputtering rates of 0.1 nm/s.

Amorphous Si with the high refractive index is not an ideal material, because of its low thermal conductivity of λ_c=0.026 W/cmK (compared to InP: λ_c=0.68 W/cmK) and its relative high optical loss at 1.3 μm and 1.55 μm wavelength. At 1.55 μm wavelength, α-Si has a refractive index of nearly 3.48. Fig. 6 shows the absorption measurement of two α-Si layers with different thicknesses. At 1.55 μm the layers show an absorption coefficient of 1050 cm^{-1}, much higher than the literature value of 600–800 cm^{-1} [7]. For the fabrication of high quality mirrors it seems to be necessary to heat the substrate up to 350 °C. This could reduce the optical loss of the α-Si. Al_2O_3 has nearly the same thermal conductivity (λ_c = 0.025 W/cmK) as α-Si. At 1.55 μm wavelength, the measured refractive index is about 1.6±0.02, the absorption loss is negligible and depends on the deposition conditions and limits the maximum achievable reflectivity from such a mirror. The combination of both materials for dielectric mirrors results in good optical and thermal properties.

For the measurement of the reflectivity of the DBRs we used a standard spectrometer (λ=500-2000 nm, accuracy ±1%) and a multireflection spectrometer (1.55 μm, accuracy better ±0.1%).

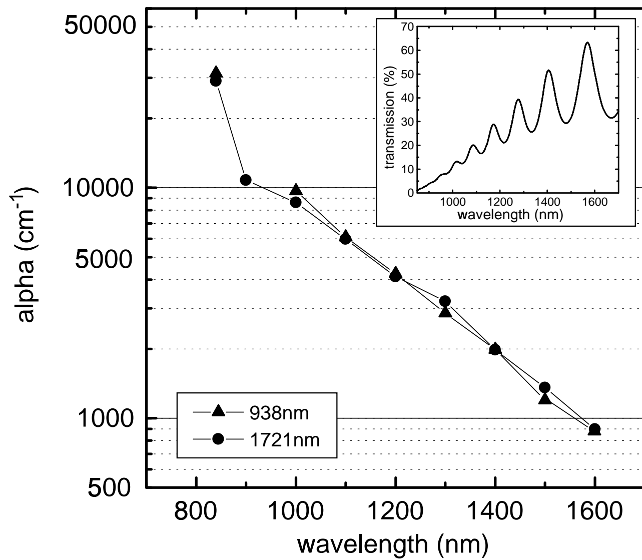

Fig. 6. Absorption measurement of 938 nm and 1721 nm thick α-Si layers at several wavelengths. For the calculation of the absorption coefficient the measurement of the transmission coefficient (small picture) is used.

Fig. 7 shows the measured reflectivity at the resonance wavelength of $1.55\,\mu$m for Al_2O_3/α-Si mirrors as a function of layer pairs. The reflectivities of the multilayer stack were numerical calculated with the transfer matrix theory described in [8]. For the calculation we used the ideal refractive index of $n_{Al_2O_3}$=1.6 and $n_{\alpha-Si}$=3.48. The measured reflectivity from Fig. 7 indicate an absorption coefficient of about $1500\,cm^{-1}$. In our Bragg reflectors the refractive index of non-ideal α-Si is about 2.9 to 3.35 and so the absorption must be smaller. The absorbtion measurement (Fig. 6) gives a coefficient of $1050\,cm^{-1}$.

Due to the large refractive index difference we obtain a high reflectivity already for a few DBR periods. The absorption in the α-Si limits the maximum reflectivity. If we assume an absorption coefficient of $800\,cm^{-1}$, we obtain a maximum reflectivity of about 99.2%.

To obtain a higher reflectivity we intent to fabricate hybrid mirrors consisting of a Al_2O_3/α-Si DBR and a metal reflector i.e. Ag.

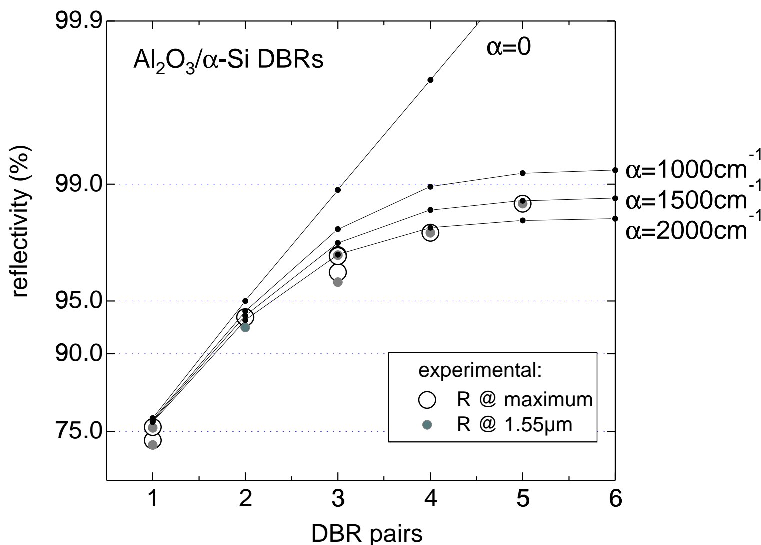

Fig. 7. Measured reflectivity of different pairs of Al_2O_3/α-Si DBRs at resonance wavelength of $1.55\,\mu$m. The straight lines show the calculated reflectivity at different absorption of α-Si.

References

[1] T. Baba, Y. Yogo, K. Suzuki, and K. Iga, "Near room temperature continous wave lasing characteristics of GaInAsP/InP surface emitting laser", *Electron. Lett.*, vol. 29, pp. 913–914, 1993.

[2] K. Uomi, S. J. B. Yoo, A. Scherer, R. Bhat, N. C. Andreadakis, C. E. Zah, M. A. Koza, and T. P. Lee, "Low threshold, room temperature pulsed operation of 1.5-μm vertical-cavity surface-emitting lasers with an optimized multi-quantum well active layer", *IEEE Photon. Technol. Lett.*, vol. 6, pp. 317–319, 1994.

[3] D. I. Babic, J. J. Dudley, K. Streubel, R. P. Mirin, B. I. Miller, J. E. Bowers, and E. L. Hu, "Double-fused 1.52 μm vertical-cavity lasers", *Appl. Phys. Lett.*, vol. 66, pp. 1030–1032, 1995.

[4] D. I. Babic, K. Streubel, R. P. Mirin, N. M. Margalit, J. E. Bowers, and E. L. Hu, "Room-temperature continous-wave operation of 1.54-μm vertical-cavity lasers", IOOC 1995, PDI-5, Hongkong.

[5] K. L. Lear, K. D. Choquette, R. P. Schneider, Jr., S. P. Kilcoyne, and K. M. Geib, "Selectively Oxidised Vertical Cavity Surface Emitting Lasers with 50% Power Conversion Efficiency", *Electron. Lett.*, vol. 31, pp. 208–209, 1995.

[6] S. J. Caracci, M. R. Krames, N. Holonyak, Jr., M. J. Ludowise, and A. Fischer-Colbrie, "Long wavelength ($\lambda \approx 1.5$ μm) native-oxide-defined InAlAs-InP-InGaAsP quantum well heterostructure laser diodes", *J. Appl. Phys.*, vol. 75, pp. 2706–2708, 1994.

[7] E. D. Palik, *Handbook of Optical Constants of Solids*. New York: Academic Press, Inc., 1985.

[8] P. Yeh, *Optical Waves in Layered Media*. New York: John Wiley & Sons, 1988.

Wafer Fusion for 1.55 μm VCSELs

Jürgen Joos, Torsten Wipiejewski

Wafer fusion is a promising technique in semiconductor technology. It allows combining lattice mismatched material such as GaAs and InP. This report introduces wafer fusion as basic method for fabricating vertical-cavity surface-emitting lasers (VCSELs) emitting at 1.55 μm.

1. Introduction

The concept of a VCSEL emitting at 1.55 μm is still an important aim in optical communications. It combines the advantage of working at the minimum absorption of silica glass fibers with high coupling efficiency obtainable by use of a vertically emitting laser. The active layer of a long wavelength laser consists of InP-based InGaAs(P). Unfortunately it is nearly impossible to fabricate Bragg reflectors with a sufficient reflectivity with this material. Due to the small difference in the refractive indices of InP and InGaAs a very high number of layers is necessary such that absorption becomes considerably high. The way out of this dilemma lays in using Al(Ga)As/GaAs reflectors, which is a well known and approved material. Yet there is a lattice mismatch between GaAs and InP and epitaxy of strained layers can only take place as long as they are below the critical thickness which is in this case only a few nanometers. Instead of growing AlGaAs/GaAs mirrors directly on active InGaAsP/InP layers we use the technique of wafer fusion to get epitaxially grown layers together.

2. Processing

A) Preparation

One of the most important aspects in wafer fusion is the preparation of the surfaces. Particles at the fused interface lead to unfused areas. But the main problem is not only contamination. Native oxide that emerges at semiconductor surfaces when being exposed to air raises the electrical resistance of the interface dramatically. We use several steps to clean the surfaces from contaminations and from oxides. Firstly acetone and methanol clean from organic residues of previous steps. Then a combination of ammonia solution and hydrofluoric acid removes oxide layers.

B) Fusion Process

The clean samples are fixed onto each other by means of a graphite fixture which allows to adjust a defined mechanical pressure. Now the fixture is put into the reactor which consists of a quartz tube that is evacuated, refilled with nitrogen, and heated up. The reactor setup is drafted in Fig. 1.

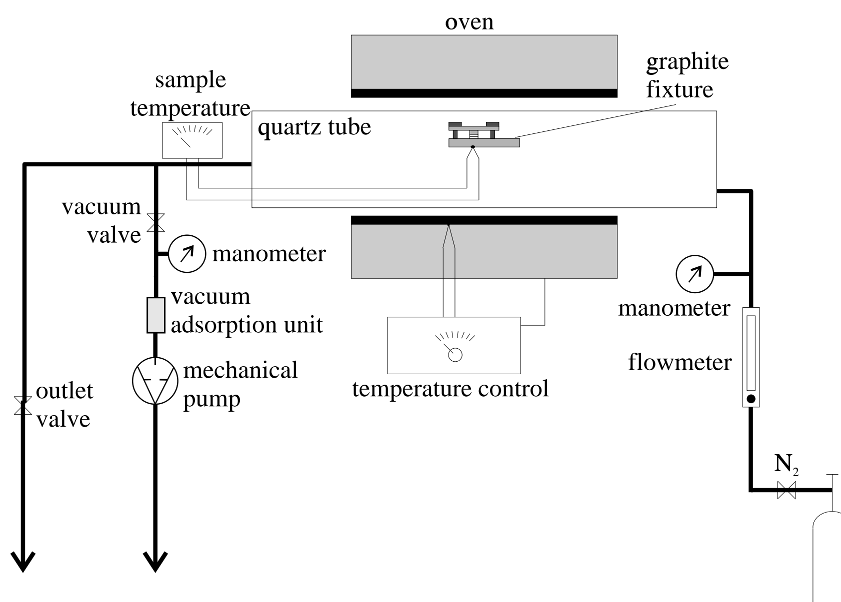

Fig. 1. Fusion reactor setup.

Although others use hydrogen as fusing atmosphere [1, 2] we obtained very good results using a constant nitrogen flow during the fusion process. The fusion takes place at a temperature of 650° C. With this process we are able to fuse InP and GaAs with an area of 8 mm × 8 mm reproducibly.

3. Characterization

Considering Fig. 2 where a transmission electron microscope (TEM) photograph of a fused interface of GaAs on InP is shown atoms are seen as bright dots. There is a perfect junction without any oxide layer between the GaAs crystal in the upper half and the InP crystal in the lower half. As one watches the atom rows carefully diagonally under a flat angle it can be found that two rows of atoms in the GaAs crystal do not run across the interface continuing in the InP crystal but are cut off at the interface. The two rows are located at the white areas. With the lattice constants of GaAs $a_{\mathrm{GaAs}} = 0.5653\,\mathrm{nm}$ and InP $a_{\mathrm{InP}} = 0.5869\,\mathrm{nm}$ the distance d between two of those dislocations caused by the lattice mismatch can be calculated as

$$d = \frac{a_{\mathrm{InP}} \cdot a_{\mathrm{GaAs}}}{a_{\mathrm{InP}} - a_{\mathrm{GaAs}}} = 15.3\,\mathrm{nm} \qquad (1)$$

which is in good agreement with the TEM photograph.

First results seem to show a moderately lower photoluminesence intensity of the active material which is assumed to be caused by outdiffusion of dopants. There also seems to be a voltage drop of at least 3 V at the fusion interface depending on the doping material.

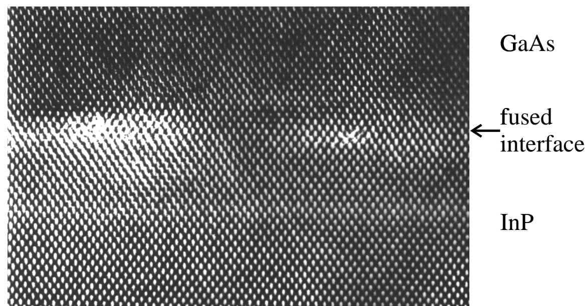

Fig. 2. TEM photograph of fused interface performed in collaboration with EPFL.

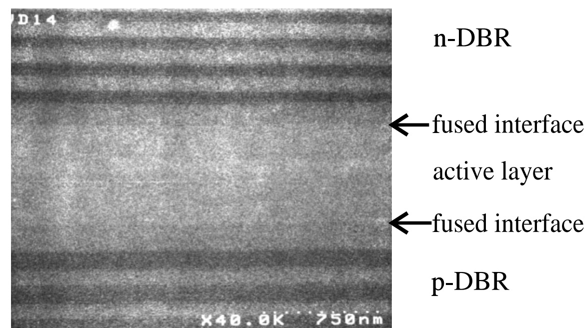

Fig. 3. SEM photograph of double fused sample.

4. VCSEL Fabrication

As Fig. 3 shows we processed a double-fused structure consisting of an n-doped AlAs/GaAs Bragg reflector, an InGaAsP active region, and a p-doped AlGaAs/GaAs Bragg reflector. Yet the fabrication of VCSELs requires more than the fusion process itself. After the first fusion step the InP substrate has to be removed by selective chemical etching. Furthermore there has to be an exact definition of the thickness of the active layer to fit the emitting wavelength to the optical resonator. This adjustment is obtained by wet chemical etching. Finally the lateral structure has to be defined and the metal contacts have to be deposited.

Another approach to the $1.55\,\mu$m VCSEL is the use of a single-fused structure which is completed by a dielectric Bragg reflector. This avoids additional thermal stress caused by the second fusion step. The main disadvantage of this method is the need of a ring metal contact around the dielectric layers and the resulting inhomogenous current distribution.

5. Summary

We have been able to develop a wafer fusion process that allows reproducible fabrication of InP and GaAs crystals. It has been shown that no native oxide layer is remaining at the fused interface. Although it is already possible to obtain double fused VCSEL structures there has to be put further effort on design and modelling of the laser cavity. It is also necessary to further investigate the electrical behaviour of the fused interface as well as the impact of the fusion process on the quality of the semiconductor material.

6. Acknowledgements

We like to thank Dr. Alok Rudra (Institute for Micro- and Optoelectronics, Swiss Federal Institute of Technology EPFL) for performing the TEM photographs and Reiner Bidenbach for doing the wafer fusion experiments.

References

[1] D. I. Babic, K. Streubel, R. P. Mirin, N. M. Margalit, M. G. Peters, J. E. Bowers, and E. L. Hu, "Fabrication and characteristics of double-fused vertical-cavity lasers", *Optical and Quantum Electron.*, vol. 28, pp. 475–485, 1996.

[2] R. J. Ram, J. J. Dudley, J. E. Bowers, L. Yang, K. Carey, S. J. Rosner, and K. Nauka, "GaAs to InP wafer fusion", *J. Appl. Phys.*, vol. 78, pp. 4227–4237, 1995.

Improvement of the Operation Characteristics of VCSELs by Carbon Doping

Gernot Reiner

This report deals with the improvements in operation characteristics of vertical-cavity surface-emitting lasers (VCSELs) emerging from substituting the conventional p-type dopant beryllium by carbon. For VCSELs with GaAs quantum wells, the peak wall plug efficiencies have been increased from 40 % to now 53 %. Driving voltages as well as output powers show significant improvements, even at reduced doping levels.

1. Introduction

Short wavelength vertical-cavity surface-emitting lasers are attractive light sources since they offer a number of advantages in comparison to edge-emitting laser diodes. Considering performance, low lasing threshold, high-speed dynamic single-mode operation and very high electrical to optical power conversion efficiencies at mW output powers are most attractive. Manufacturing issues like low-cost LED-like wafer-scale chip production without cleaving, on-wafer testing and simplified mounting and packaging makes them ideal for mass production. One major drawback of VCSELs however are the relatively high operation voltages required well above threshold and the high differential resistivities observed. Considerable effort has been put in reducing driving voltages and resistivities which are mainly caused by the p-doped Bragg reflector. Using the conventional p-type dopant beryllium one has to face several problems. Beryllium has a rather high activation energy in AlAs. Therefore the free carrier concentration in AlAs is rather low. For VCSEL devices with threshold voltages below 3 V, the low index AlAs layers of the p-DBR must be replaced by ternary AlGaAs layers. Due to the relatively high diffusion coefficient of beryllium, sharp doping profiles like those required in DBRs can only be achieved if the growth temperature of the p-DBR is significantly reduced compared to values normally used for growth. However, although taking care of the above mentioned points, relatively high doping levels are required throughout the p-DBR to achieve device performances with threshold voltages close to the bandgap of the active material. Fig. 1 shows the output characteristics of a 6 μm VCSEL device with optimized beryllium doped p-DBR. The upper p-type mirror consists of 24 $Al_{0.9}Ga_{0.1}As/Al_{0.2}Ga_{0.8}As$ pairs, while the lower n-type mirror consists of 30.5 $AlAs/Al_{0.2}Ga_{0.8}As$ pairs. The p-type mirror is homogeneously doped to 5×10^{18}. Additional δ-doping at the backward driven heterojunctions and step grading is applied as described in [1]. The device has a threshold current of 730 μA at a threshold voltage of 1.7 V. The wall plug efficiency reaches a maximum of 40 % and the maximum output power is around 8 mW. The high doping level of 5×10^{18} causes optical losses due to free carrier absorption which is detrimental to the overall device performance. Therefore improved device performance can be expected from p-type dopants with low activation energies and low diffusivity.

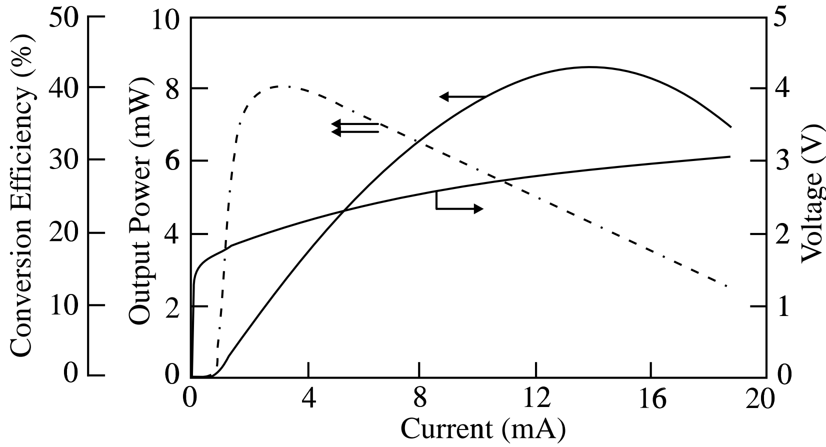

Fig. 1. Output characteristics of a 6 μm diameter VCSEL with beryllium doped top DBR.

2. Carbon doping with carbon tetrabromide (CBr_4).

Carbon, is known as a p-type dopant with the above mentioned properties [2, 3]. Several precursors have been investigated for supplying the active carbon species as well as carbon filament sources. Carbon tetrabromide (CBr_4) seems to be the most attactive one [4]. Fig. 2 shows the gas panel that was built to allow carbon doping with CBr_4 in our solid source MBE system. Vapor of carbon tetrabromide from a single-valved stainless steel cylinder is injected via

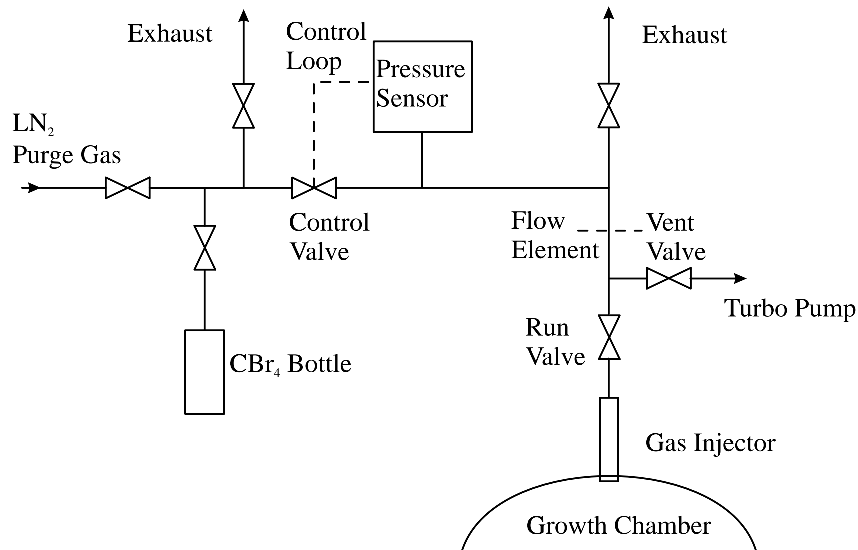

Fig. 2. Schematic of the CBr_4 gas handling system.

a pipe system and a gas injector into the growth chamber. No carrier gas is used to transport the CBr_4 to the system. The amount of vapor injected into the system is controlled by an automatic valve driven by a high precision Baratron pressure sensor and a flow element. A run/vent configuration is used for exact flux preadjustments and to improve the abruptness of the doping profiles. The whole pipe system is pumped with a 50 l/s turbo molecular pump and is kept at a temperature of around 40 °C to avoid recondensation of CBr_4 vapor. The gas injector is kept at a temperature of 120 °C preventing condensation of CBr_4 at the cryo shroud

and decomposition of the vapor in the injector. The elevated temperature of the gas injector is also necessary to avoid deposition of evaporated materials inside the injector, especially arsenic.

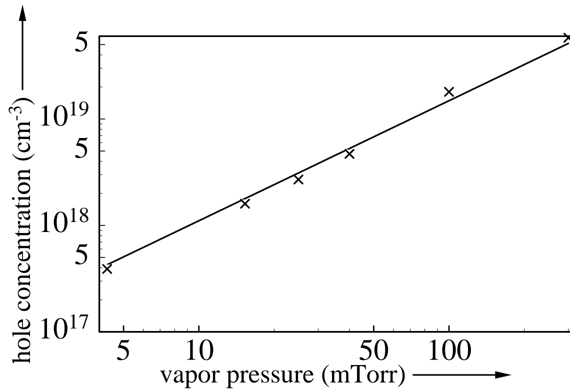

Fig. 3. Hole concentration as a function of inlet pressure in GaAs.

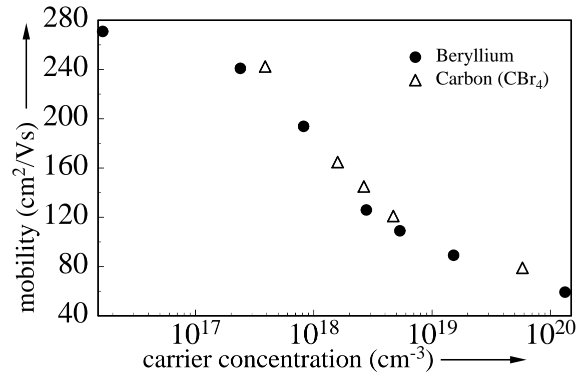

Fig. 4. Hole mobility as a function of carrier density.

Fig. 3 shows the hole concentration in GaAs as a function of inlet pressure. The GaAs growth rate is 1428 nm/h and the flow element was thosen to be 0.2 mm in diameter. There is approximately a linear dependency of carrier concentration on input pressure in the double logarithmic scale. Fig. 4 shows hole mobilities at 300 K in GaAs as a function of hole concentration for both beryllium and carbon. Mobilities were measured using the Van-der-Pauw Hall-effect technique. In general, the carbon doped layers show slightly higher mobilities than the beryllium doped ones. The whole gas handling system is integrated into the computer controlled MBE enviroment which allows switching of valves and providing pressure setpoints by the MBE software already in use. Fig. 5 shows the output characteristics of a 6 μm diameter VCSEL with three

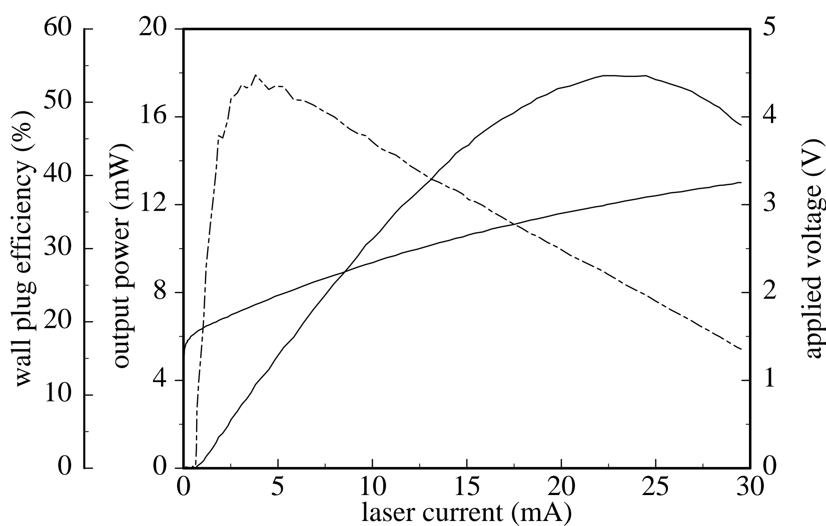

Fig. 5. Output characteristics of a 6 μm VCSEL with carbon doped top DBR.

8 nm thick GaAs/$Al_{0.2}Ga_{0.8}As$ quantum wells and carbon p-doped top Bragg reflector. The VCSEL has a bottom reflector with 30.5 AlAs/$Al_{0.2}Ga_{0.8}As$ pairs and a top reflector with 25 $Al_{0.9}Ga_{0.1}As/Al_{0.2}Ga_{0.8}As$ pairs. Doping levels in the p-mirror are around 2.5×10^{18} cm^{-3} and

therefore only half as high as in the case of the beryllium doped devices. Growth temperature and V/III ratio is the same as in case of beryllium. The device shows a threshold current of 700 μA which is nearly identical to the Be-doped device. The threshold voltage of 1.57 V is clearly lower compared to Be-doped devices. A differential resistance of 70 Ω also compares very favourable with 95 Ω for the Be-doped device. The devices achieve a maximum wall plug efficiency of 53 % and a maximum output power of 17 mW.

3. Conclusion

A dopant gas line for a solid source MBE system has been set up. *P*-type doping with vapor from carbon tetrabromide has been established. The carbon doped GaAs layers show improved electrical properties in comparison to beryllium *p*-doped layers. VCSELs with carbon doped *p*-DBRs show significant improvements in their output characteristics. The maximum wall-plug efficieny for a carbon doped VCSEL is now 53 % in comparison to formerly 40 % for the beryllium doped device. This improvement is attributed to the reduced optical absorption loss in the VCSEL device made possible by the reduction in overall doping concentration. A reduction in doping concentration is possible due to the smaller diffusivity of carbon in comparison to beryllium thus allowing sharper doping profiles.

References

[1] G. Reiner, E. Zeeb, B. Möller, M. Ries, and K. J. Ebeling, "Optimization of planar Be-doped InGaAs VCSELs with two-sided output", *IEEE Photon. Technol. Lett.*, vol. 7, pp. 730–732, 1995.

[2] K. Saito, E. Tokumitsu, T. Akatsuka, M. Miyauchi, T. Yamada, M. Konagai, K. Takahashi, "Characterization of p-type GaAs heavily doped with carbon grown by metalorganic molecular beam epitaxy", *J. Appl. Phys.*, vol. 55, pp. 3975–3979, 1988.

[3] C. R. Abernathy, S. J. Pearton, R. Caruso, F. Ren, J. Kovalchik, "Ultrahigh doping of GaAs by carbon during metalorganic molecular beam epitaxy", *Appl. Phys. Lett.*, vol. 55, pp. 1750–1752, 1989.

[4] W. E. Hoke, D. W. Weir, P. J. Lemonias, and H. T. Hendriks, "Carbon tetrabromide carbon doping of molecular beam epitaxial (GaAs) films", *Appl. Phys. Lett.*, vol. 64, pp. 202–204, 1994.

Carbon Doped 850 nm Wavelength GaAs VCSELs

Roland Jäger

Vertical-cavity surface-emitting lasers with Carbon p-type doped distributed Bragg reflectors show record room temperature wallplug efficiencies of 57 %. Threshold current and voltage are 0.8 mA and 1.58 V, respectively. Little influence of the substrate temperature during molecular beam epitaxial growth of the p-type layers on the current-voltage device characteristics is shown. Secondary ion mass spectra show sharp Carbon doping profiles.

1. Introduction

Over the past few years the performance of vertical-cavity surface-emitting lasers (VCSELs) has improved considerably through the advent of selective oxidation [1] and low-resistance distributed Bragg reflectors (DBRs) [2,3]. High wallplug efficiencies of about 50 % [4,5] and very low threshold currents of less than 100 μA [6,7] have been demonstrated with 980 nm InGaAs QW VCSELs. Presently, VCSELs with emission wavelengths of around 850 nm are of great interest as transmitters for optical interconnection.

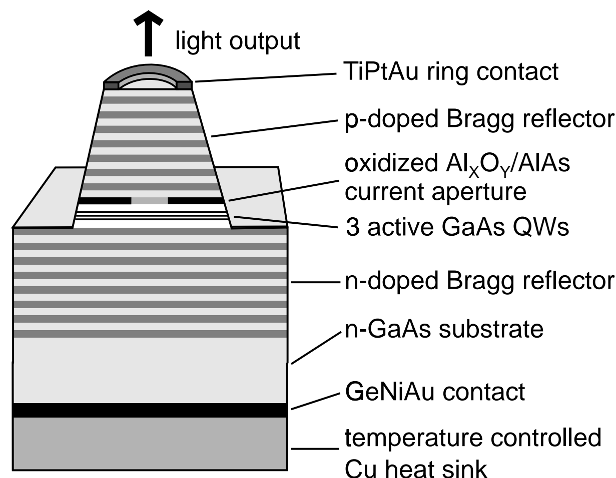

Fig. 1. Cut-away view of a selectively oxidized GaAs VCSEL.

2. Device structure

A schematic cut-away view of the fabricated oxide confined GaAs VCSELs is illustrated in Fig. 1. The epitaxial structures are grown using solid source molecular beam epitaxy (MBE). The bottom Bragg reflector consists of 30.5 n-type Silicon doped $AlAs/Al_{0.2}Ga_{0.8}As$ pairs. The

active region contains three 8 nm thick GaAs quantum wells separated by 10 nm $Al_{0.2}Ga_{0.8}As$ barriers. The p-type top DBR consists of 26 Carbon doped $Al_{0.2}Ga_{0.8}As$ / $Al_{0.9}Ga_{0.1}As$ pairs. A 30 nm AlAs layer is used for subsequent selective oxidation and is integrated in the lowest p-type top DBR pair. The oxidation layer is shifted towards a node of the longitudinal standing wave pattern to reduce the optical index guiding. Using wet chemical etching, mesas with diameters of 38 μm are formed. The etching process is stopped below the AlAs layer. Oxidation in an N_2/H_2O atmosphere at a temperature of 400°C defines the active area of the lasers, typically a few μm in diameter. On the top side TiPtAu ring contacts and on the bottom side broad area GeNiAu n-contacts are deposited.

3. Device characteristics

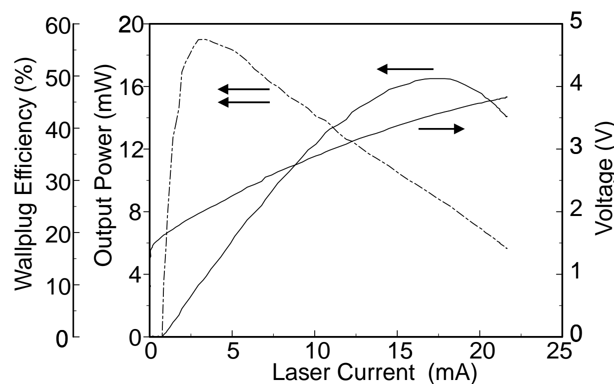

Fig. 2. Output characteristics of a 5 μm diameter GaAs VCSEL.

Output characteristics of a 5 μm active diameter device are given in Fig. 2. Threshold current and voltage are 0.8 mA and 1.58 V, respectively. The threshold voltage is only 120 mV larger than the photon energy limit of 1.46 V at 850 nm emission wavelength. Maximum conversion efficiency of 57 % is obtained at 3 mA current for an output power of 3.3 mW. Maximum output power of 16.6 mW achieved at 17.4 mA is limited by thermal roll over. The differential resistance of about 140 Ω is caused by the small current aperture. The light output is measured using a Newport 1830C optical power meter with a calibrated Silicon diode, which is directly illuminated. This equipment was cross-checked using a further detector system. The samples were mounted on Copper plates but were not cooled. At 20°C the emission spectrum shown in Fig. 3 is transverse multi mode, centered at 850 nm. The superposition of several higher order modes results in a good overlap of gain and intensity profiles. The spectra were measured using a microscope objective to couple the laser emission into a 50 μm core fiber which transmits the light to an Anritsu optical spectrum analyzer.

4. Carbon Doping

In comparison to Beryllium or Zinc doping the diffusion of Carbon atoms is rather low [8] and leads to sharper doping profiles with improved current-voltage (I-V) device characteristics [9]. Therefore Beryllium p-type doped DBRs are usually grown at low substrate temperatures, e.g., 480 °C. To show the advantage of the low Carbon diffusion two samples where grown, one at

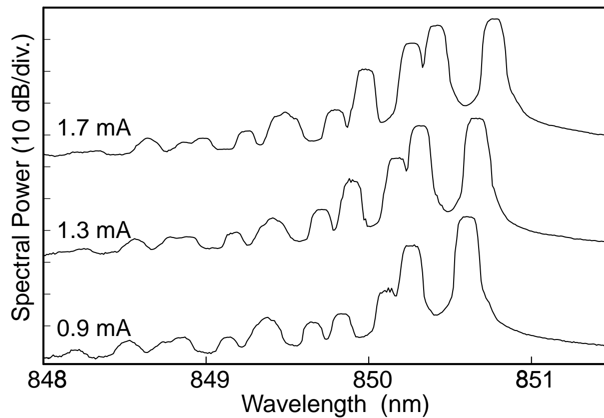

Fig. 3. Emission spectrum of the VCSEL in Fig. 2 for various laser currents. Spectra are offset by 30 dB for clarity.

480 °C and the other at 580 °C. All other parameter and process steps where nominally the same. The I-V characteristics of both samples are shown in Fig. 4 with no detectable increase of the

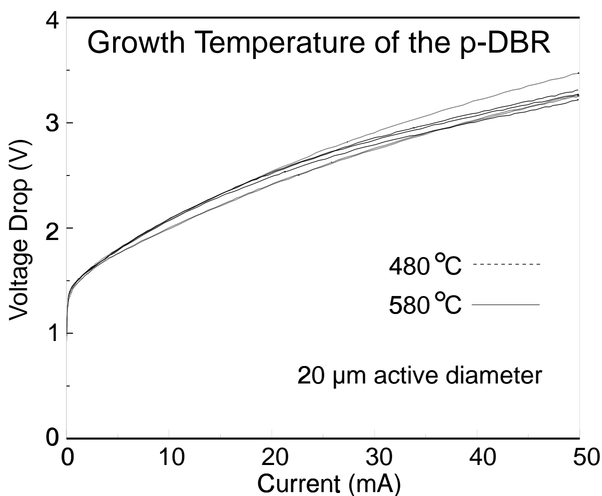

Fig. 4. I-V-characteristics of VCSELs with Carbon p-type doped DBRs grown at substrate temperatures of 480°C and 580°C.

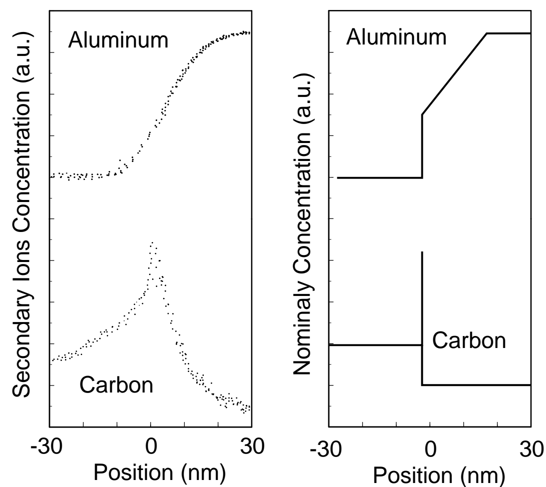

Fig. 5. Aluminum and Carbon SIMS profiles in comparison to nominal distributions.

resistance. A secondary ion mass spectrum (SIMS) analysis was performed on both samples. Due to the dependence of the secondary ions yield on the aluminum content of the AlGaAs layers a recalibration was performed. The resulting SIMS profile is shown in Fig. 5. The peak width ist mainly caused by the resolution of the SIMS measurement system. No correlation was found between Carbon and Oxygen concentrations, indicating a high purity of the Carbon source.

5. Conclusion

Oxide confined VCSELs of 5 μm diameter with record high 57 % conversion efficiency and maximum output power of 16.6 mW are demonstrated. The advantage of the low diffusion of Carbon atoms could be confirmed by comparing the I-V characteristics of two samples grown at different substrate temperatures. SIMS analysis shows a sharp Carbon doping profile.

References

[1] D. L. Huffaker, D. G. Deppe, and K. Kumar, "Native-oxide ring contact for low threshold vertical-cavity lasers", *Appl. Phys. Lett.*, vol. 65, pp. 97–99, 1994.

[2] M. G. Peters, D. B. Young, F. H. Peters, J. W. Scott, B. J. Thibeault, and L. A. Coldren, "17.3 % peak wall plug efficiency vertical-cavity surface-emitting lasers using lower barrier mirrors", *IEEE Photon. Technol. Lett.*, vol. 6, pp. 31–33, 1994.

[3] G. Reiner, E. Zeeb, B. Möller, M. Ries, and K. J. Ebeling, "Optimization of planar Be-doped InGaAs VCSEL's with two-sided output", *IEEE Photon. Technol. Lett.*, vol. 7, pp. 730–732, 1995.

[4] K. L. Lear, K. D. Choquette, R. P. Schneider, Jr., S. P. Kilcoyne, and K. M. Geib, "Selectively oxidised vertical cavity surface emitting lasers with 50 % power conversion efficiency", *Electron. Lett.*, vol. 31, pp. 208–209, 1995.

[5] B. Weigl, M. Grabherr, G. Reiner, and K. J. Ebeling, "High efficiency selectively oxidised MBE grown vertical-cavity surface-emitting lasers", *Electron. Lett.*, vol. 32, pp. 557–558, 1996.

[6] Y. Hayashi, T. Mukaihara, N. Hatori, N. Ohnoki, A. Matsutani, F. Koyama, and K. Iga, "Lasing characteristics of low-threshold oxide confinement InGaAs-GaAlAs vertical-cavity surface-emitting lasers", *IEEE Photon. Technol. Lett.*, vol. 7, pp. 1324–1326, 1995.

[7] G. M. Yang, M. H. MacDougal, and P. D. Dapkus, "Ultralow threshold current vertical-cavity surface-emitting lasers obtained with selective oxidation", *Electron. Lett.*, vol. 31, pp. 886–888, 1995.

[8] B. T. Cunningham, L. J. Guido, J. E. Baker, J. S. Major, N. Holonyak, and G. E. Stillman, "Carbon diffusion in undoped, n-type and p-type GaAs", *Appl. Phys. Lett.*, vol. 55, pp. 687–689, 1989.

[9] R. Hey, A. Paraskevopoulos, J. Sebastian, B. Jenichen, M. Höricke, and S. Westphal, "Low voltage vertical-cavity surface-emitting lasers (VCSELs) with low resistance C-doped GaAs/AlAs mirrors", *Inst. Phys. Conf.*, Ser. No. 136: Chapter 12, pp. 821–822, 1994.

High Efficiency Wide Temperature Range GaAs VCSELs

Bernhard Weigl

Using solid source MBE and Carbon as p-type dopant we have fabricated 840 nm wavelength GaAs vertical cavity lasers (VCSELs) with maximum conversion efficiencies of 57 % [P-55]. Investigations on the temperature behavior exhibit a maximum cw operation range from −80 °C up to +185 °C. Threshold current in a reduced temperature range from −40 °C to +80 °C stays below 500 μA while the laser current required for 1 mW of optical output power ranges between 1.5 mA and 1.85 mA.

1. Introduction

Due to intensive research the device characteristics of VCSELs have been strongly improved during the last few years. Using selective oxidation power conversion efficiencies exceeding 50 % were obtained for the first time in 980 nm wavelength InGaAs devices [1]. Agreements on the 820 nm to 860 nm wavelength regime for short distance optical data links have focused the interest on VCSELs with active GaAs [2] or InAlGaAs [3] quantum wells.

2. Device Structure

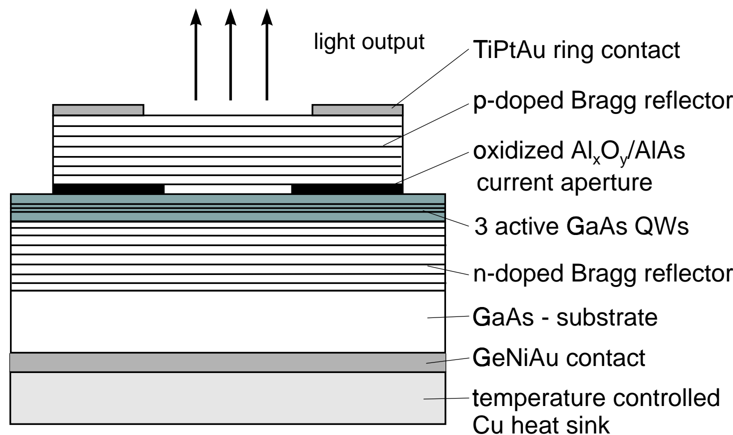

Fig. 1. Cross-sectional view of an oxidized GaAs VCSEL.

Fig. 1 shows a cross-sectional view of the optimized layer structure of the oxide confined GaAs VCSELs under investigation. The active region contains three 8 nm thick GaAs quantum wells in $Al_{0.2}Ga_{0.8}As$ barriers. The bottom Bragg reflector consists of 30.5 n-type Si doped AlAs/$Al_{0.2}Ga_{0.8}As$ pairs. The p-type output coupler has 26 modulation doped $Al_{0.2}Ga_{0.8}As$ /

$Al_{0.9}Ga_{0.1}As$ pairs. In comparison to our previous Beryllium doped devices, Carbon allows the realization of sharper doping profiles and with the high acceptor activation rate the total doping concentration and therefore absorption in the mirror can be reduced by a factor of two with even improved current-voltage characteristics. The 30 nm AlAs layer to be used for subsequent selective oxidation is shifted out of the antinode of the longitudinal standing wave pattern in order to weaken optical waveguiding.

3. Device Characteristics

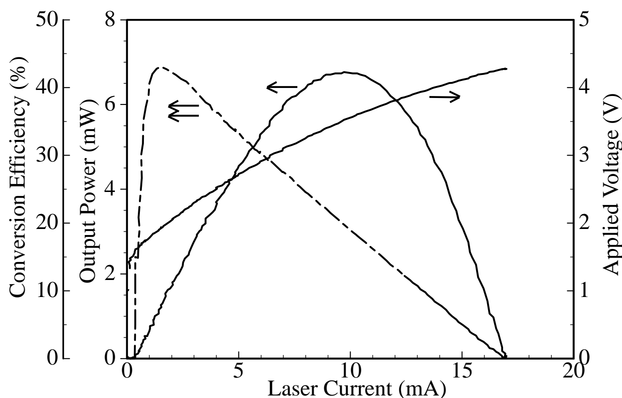

Fig. 2. Output characteristics of an extremely efficient $4\,\mu$m GaAs VCSEL.

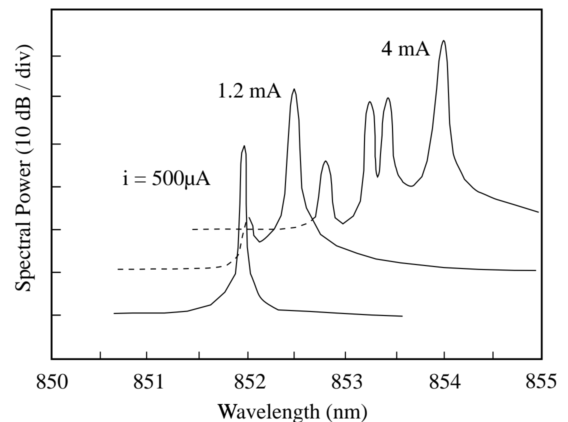

Fig. 3. Output spectra of the VCSEL in Fig. 2 for different driving currents.

In contrast to the record efficiency lasers of $5\,\mu$m diameter, investigations on the thermal behavior are performed using devices with a reduced active diameter of $4\,\mu$m. Output characteristics at room temperature are given in Fig. 2. Threshold current and voltage are $390\,\mu$A and 1.60 V, respectively. Maximum conversion efficiency of 43 % is obtained at 1.6 mA current for an output power of 1.3 mW. Maximum output power of 6.4 mW achieved at 9.5 mA is limited by thermal roll over. Threshold voltage is about 120 mV above the bandgap energy. The differential resistance of about $260\,\Omega$ is caused by the small current aperture. The emission spectra for different currents are given in Fig. 3, offset by 10 dB for clarity. Up to 1.2 mA laser emission is single-mode at about 852 nm wavelength. The mode spacing of the lateral higher order modes, appearing at slightly shorter wavelength, is related to a calculated diameter of $3.7\,\mu$m that is in good agreement with the nominal diameter of $4\,\mu$m. In the multimode regime the superposition of several higher order modes results in an improved overlap of gain and intensity profiles.

4. Temperature Range

Highly efficient lasers exhibit high optical gain as well as low internal heating and therefore are well suited for operation over a wide temperature range. In Fig. 4 optical output characteristics for cw operation from $-80\,°$C up to $+185\,°$C are depicted. The light output versus current curves are recorded from threshold up to thermally induced turn off of the lasers. For example, at a heat sink temperature of $-80\,°$C laser operation is observed from $400\,\mu$A up to 24 mA, the latter corresponding to a current density of $180\,\mathrm{kA/cm^2}$.

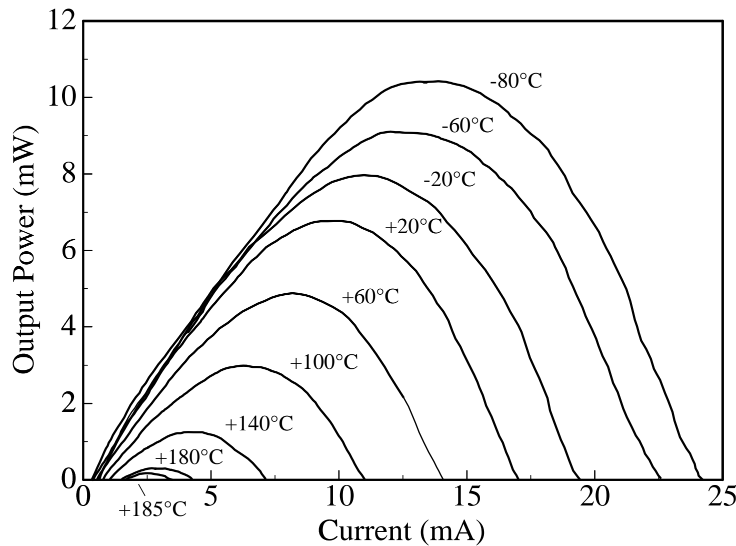

Fig. 4. Light output power versus current for various temperatures from −80 °C up to +185 °C.

Threshold currents and maximum output powers extracted from the light current characteristics are depicted in Fig. 5 over the whole temperature range. Threshold current is determined by the temperature dependent gain as well as the alignment of lasing mode and spectral gain maximum resulting in a minimum threshold of 300 μA at an ambient temperature of −20 °C for the particular devices under study. Maximum output power, limited by thermal roll over, steadily decreases with increasing heat sink temperature. Fig. 6 shows laser characteristics in a temperature range from −40 °C to +80 °C which is of primary technical interest. Within this temperature range threshold current varies between 300 μA and 500 μA, while laser current required for 1 mW of optical output power ranges between 1.5 mA and 1.85 mA. These homogeneous characteristics should allow applications without requiring any temperature stabilization. The spectral shift of the emission wavelength with temperature is evaluated to 0.065 nm/K.

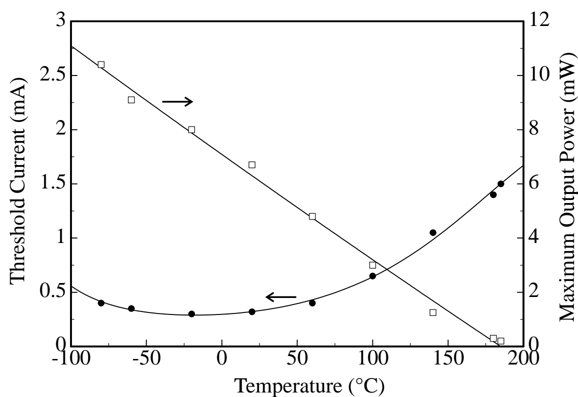

Fig. 5. Temperature dependent threshold current and maximum output power.

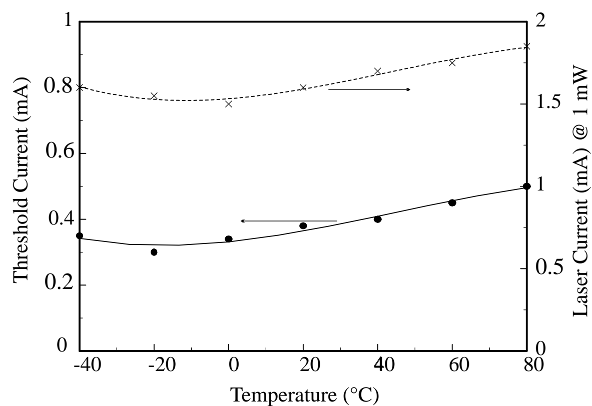

Fig. 6. Homogeneous temperature behavior of threshold current and laser current required for 1 mW output power in an industrially relevant temperature range from −40 °C to + 80 °C.

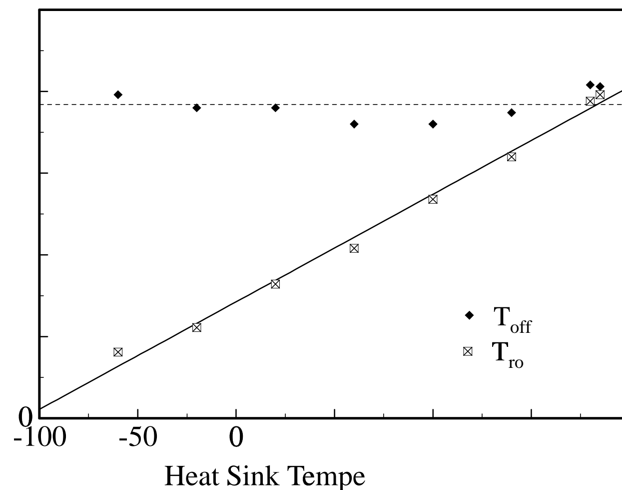

Fig. 7. Thermal roll over and laser turn off temperatures for various heat sink temperatures.

Dissipated power causes a red shift of 0.155 nm/mW, giving a thermal resistance of 2.38 K/mW for the 4 μm devices. With these spectral measurements and the evaluated thermal resistance, intrinsic temperatures for the roll over in the light current curves and the turn off of the laser are determined and plotted in Fig. 7. The intrinsic temperature for thermal roll over increases linearly with heat sink temperature while the turn off temperature of about 195 °C is found to be constant.

5. Conclusion

We have fabricated highly efficient oxide confined GaAs VCSELs emitting around 850 nm wavelength. Investigations of the operating temperature range show cw operation from −80 °C to +185 °C, where the minimum temperature is limited by the measurement setup. In an industrially relevant temperature range from −40 °C to 80 °C threshold current remains below 500 μA and the laser current required for 1 mW optical output power ranges between 1.5 mA and 1.85 mA. Other than the roll over temperature, the intrinsic turn off temperature of the VCSEL is shown to have a constant value of about 195 °C independent of the heat sink temperature.

References

[1] K. L. Lear, K. D. Choquette, R. P. Schneider, Jr., S. P. Kilcoyne, and K.M. Geib, "Selectively oxidised vertical cavity surface emitting lasers with 50 % power conversion efficiency", *Electron. Lett.*, vol. 31, pp. 208–209, 1995.

[2] R. P. Schneider, M. R. T. Tan, S. W. Corzine, and S. Y. Wang, "Oxide-confined 850 nm vertical-cavity lasers for multimode-fiber communications", *Electron. Lett.*, vol. 32, pp. 1300–1302, 1996.

[3] J. Ko, B. J. Thibeault, Y. Akulova, E. R. Hegblom, D. B. Young, and L. A. Coldren, "MBE-grown strained AlInGaAs/AlGaAs vertical cavity lasers with low threshold currents and high output power", in *Proc. LEOS 9th Annual Meeting*, Boston, MA, USA, p. 388, Nov. 1996.

Improvement of Oxide-Confined VCSELs for High Frequency Applications

Christian Jung

We report on top-emitting vertical-cavity surface-emitting laser (VCSEL) in the 850 nm wavelength regime with small mesa diameters produced by chemically assisted ion beam etching in combination with a wet-chemical etching step. Low threshold currents of 200 μA and modulation bandwidths up to 8.5 GHz are demonstrated. In addition, we also investigate three different methods of passivation and introduce a stable bondpad process.

1. Introduction

Dramatic improvements in the performance of selectively-oxidized VCSELs have been achieved in the last year. High conversion efficiencies of 57 % [P-60] and continous wave optical output powers of 180 mW [P-18] have been demonstrated. Investigations in the field of single-mode devices using a weak index guiding are also pressed ahead [P-18]. High intrinsic modulation bandwidths of VCSELs are promising for excellent high frequency behavior, therefore suggesting applications in optical data links and Gbit/s transmission systems. The highest 3 dB modulation frequency of 16.3 GHz for oxide based VCSELs has been demonstrated in [1]. The active region of this structure consists of three 8 nm InGaAs quantum wells designed for emission wavelengths around 850 nm. The device was formed with two aligned oxide apertures in square mesas by selective oxidation. To reduce the pad capacitance a 5 μm thick polyimide planarization was used and the VCSEL was bonded using 100 μm wide bonding ribbon to minimize the bondwire inductance. In this article we describe our first attempts and results in processing high-speed VCSELs with small mesa diameters. We also study the RF modulation characteristics of these devices.

2. Fabrication of High-Speed VCSELs

There are two methods available for etching a mesa device. Wet-chemical etches are usual, but tend to undercut the etch mask by a distance similar to the etch depth. This is not ideal for producing small devices, with 20 μm diameter or less at an etching depth of 3.5 μm. Therefore it is absolutely necessary to prepare the VCSELs using dry-etching techniques. The layer structure we use is very well described in [P-52]. We start the process by cleaning the sample with organic solvents to dissolve unwanted contaminant. Then we spin on a positive resist which is a convenient etch mask to pattern our devices, followed by soft-baking, exposure and development. Chemically assisted ion beam etching (CAIBE) using Cl_2 can easily produce etch depths of a few μm through AlAs/GaAs multilayers while maintaining smooth vertical sidewalls [2]. A Meißner-trap is applied in order to reduce water vapor pressure in the chamber, which is important for etching Al-containing layers. The etch depth can be determined by the

etching time knowing the exact etch rate and is controlled with a scanning electron microscope (SEM). Fig. 1 shows the scanning electron micrograph of a VCSEL with $20\,\mu$m diameter and etched to a depth of $3.5\,\mu$m.

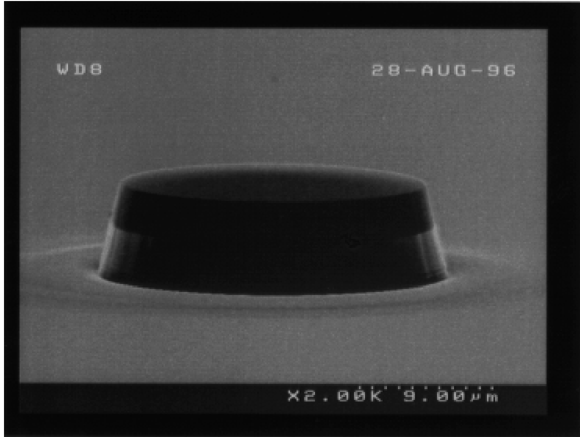

Fig. 1. Scanning electron micrograph of a dry-etched VCSEL showing smooth vertical sidewalls.

The final step in the lithographic process is resist stripping. After selective oxidation a Ti/Pt/Au ring contact for the top-emitting devices is deposited on top of the mesa and a Ge/Ni/Au broad area contact is evaporated on the backside of the substrate.

3. Mesa Passivation

Direct bonding or probing might be difficult for devices smaller than $20\,\mu$m in diameter. Thus it is often desirable to put larger contact pads over the device mesas to allow for easier contacting. This requires an insulating layer to prevent the pad from short cutting to the substrate. The next sections describe in more detail three different options for passivation.

A) Oxide Passivation with Al_2O_3

First attempts for passivation are done using a thin sputtered isolation layer. Contacting the devices requires windows on the top-sides of the mesas. This can be realized with a lithographcal step followed by wet-chemical etching. To form the contact pads we apply an image reversal process. The negative resist walls and the nearly $2.5\,\mu$m thick resist layer provides a reliable lift-off technique. The high relative permittivity $\epsilon_r = 10$ of Al_2O_3 and the thin oxide layer are limiting factors for high frequency applications due to the large parasitic capacitance caused by the bondpad. A bondpad size of $120\times120\,\mu m^2$ yields a pad capacitance of approximately 13 pF. According to the differential resistance of the VCSEL, we observed RC lowpass behavior limiting the 3 dB modulation response to nearly 700 MHz.

B) Ion Implantation for Passivation

Ion implantation is well-known as a very effective tool to create highly resistive regions in semiconductors. While in more conventional VCSELs a proton implantation step is necessary to define the active region, it is used hre only for passivation.

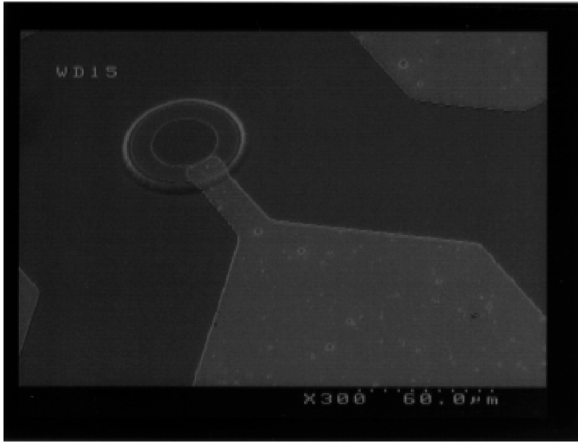

Fig. 2. SEM picture showing a bondpad on a proton implantation passivated area.

First a thick positive resist is put on top of the mesa. The implantation is carried out using protons with an energy of 80 keV and an ion dose of 10^{15} cm^{-2} leading to an implantation depth of approximately 1 μm. To ensure implantation of the mesa sides the sample is rotated during the process. After removing the resist with an oxygen plasma step and cleaning with organic solvents, the Ti/Au bondpads are deposited. Fig. 2 shows a scanning electron micrograph of a bondpad over an implantation passivated area. The bondpad metallization is about 400 nm thick. The advantage of proton implantation passivated oxide confined VCSELs is obviously the much easier bonding on a semiconductor surface.

C) Planarization and Passivation Using Polyimide

In this section we describe the attempt to passivate a VCSEL using a photosensitive polyimide. Polyimide is a polymer coating especially developed to provide a smooth planar coating of surface relief features. Fig. 3 illustrates the steps involved in passivating VCSELs in this way. First polyimide is spun (a) to planarize the surface. For contacting the devices a window has then to be opened into the polyimide (b). After exposing and developing a bake is performed

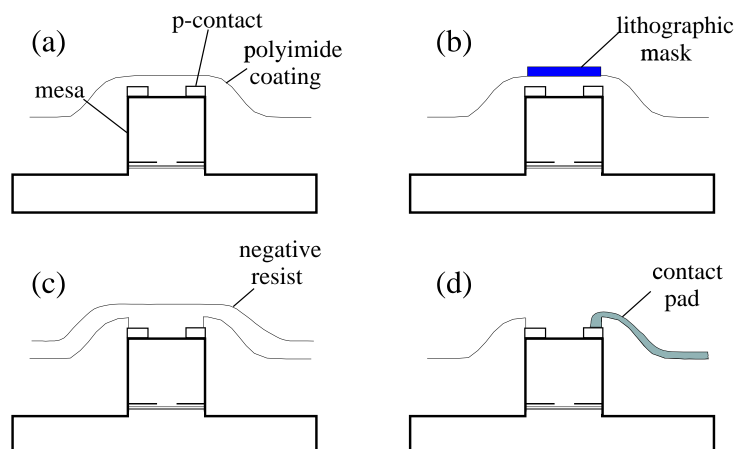

Fig. 3. Process steps to passivate VCSEL mesas using polyimide for applying bondpads.

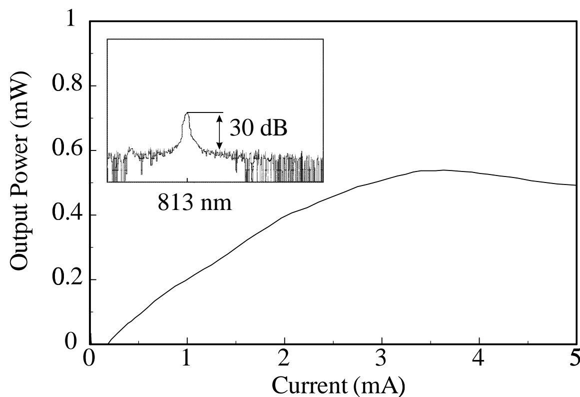

Fig. 4. Optical power against current characteristic of a 2 μm active diameter GaAs VCSEL. The inset depicts the corresponding emission spectrum at 2 mA current in a logarithmic scale with 10 dB/div. The laser oscillates at a wavelength of 813 nm and is single-mode up to 3 mA with a side mode suppression of about 30 dB.

to complete the imidization process. A pattern of contact pads is formed in the negative resist process (c) and finally p-type contact metals are evaporated (d).

Polyimide as passivating insulator around the mesa prevents AlAs layers from erosion in a moist atmosphere. Another advantage of thick polyimide layers is the very small relative permittivity of $\epsilon_r = 3.3$ predicting a better high frequency behavior compared to the oxide layer passivation using Al_2O_3. On the other hand bonding on the polyimide surface is much more difficult and requires a lot of experience.

4. Measurements

Fig. 4 depicts the continuous wave output characteristics of a selectively oxidized GaAs VCSEL with an active diameter of 2 μm. Threshold current and maximum output power are 200 μA and 0.5 mW, respectively. The inset illustrates the oscillation of the VCSEL on the fundamental mode ($\lambda = 813$ nm) up to 15 times threshold current with a side mode suppression of more than 30 dB.

For RF measurements VCSELs with larger current apertures are desirable due to the smaller differential resistance and higher optical output power. Output characteristics of a polyimide planarized dry-etched 8 μm VCSEL are shown in Fig. 5.

This laser diode exhibits a threshold current of 2.4 mA at a voltage of 1.8 V. The maximum optical output power is 5 mW, limited by thermal roll over. The emission wavelength of 810 nm reveals laser oscillation on the short wavelength side of the gain peak. Differential quantum efficiency and series resistance can be estimated to 51 % and 100 Ω, respectively. An approximately 2.2 μm thick polyimide layer is used to planarize the surface. Therefore, we expect a pad capacitance of 0.09 pF for the $80 \times 80\,\mu m^2$ large bondpad. For small signal modulation measurements the VCSELs are mounted on a SMA socket and short bonded to avoid large bondwire inductance. The laser emission is detected with a 25 GHz Si photodetector, fed to a 10 dB broadband amplifier and recorded with an HP scalar network analyzer. Typical modulation responses at various currents are shown in Fig. 6. The measurements indicate a maximum 3 dB modulation bandwidth of 8. 5 GHz at a bias of 9.0 mA. At higher currents, further increased bandwidths cannot be observed due to damping of the relaxation resonance and reduced differential gain due to heating. Size dependent investigations reveal that VCSELs of smaller active diameter but the same pad capacitance exhibit a smaller electrical 3 dB modulation bandwidth due to

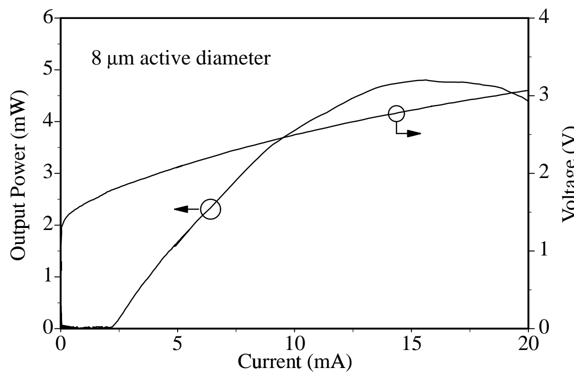

Fig. 5. Light output and voltage against current characteristic of a dry-etched VCSEL with 8 μm current aperture.

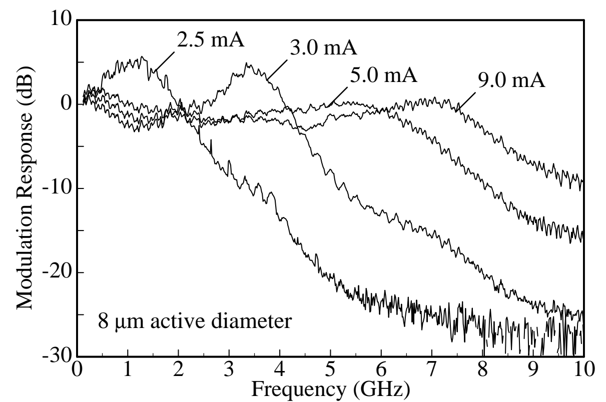

Fig. 6. Modulation response of a polyimide passivated VCSEL for different driving currents.

their higher differential resistance. Therefore the modulation response is obviously limited in bandwidth by the RC time constant of the pad capacitance and series resistance of the VCSEL.

On the other hand we also investigated the RF behavior of wet-chemically etched VCSELs with the intention to compare polyimide and proton implantation for mesa passivation. A bondpad size of $120\times120\,\mu\text{m}^2$ results in pad capacitance of 1.4 pF and 0.2 pF for proton implantation and polyimide passivated VCSELs, respectively. Small proton implantation passivated devices show a very strong lowpass behavior due to their large RC time constant resulting in bandwidths of only 1 GHz. Similar lasers with nearly the same series resistance using polyimide passivation exhibit 3 dB bandwidths of about 4.1 GHz.

5. Summary

In conclusion, VCSELs with a small mesa diameter of 20 μm using a special dry-etching method in combination with a wet-chemical etching step have been fabricated. Low threshold currents of less than 200 μA have been demonstrated. We have also discussed proton implantation and polyimide as two possible methods for passivation. The 3 dB modulation frequency of VCSELs with polyimide passivation exceeds 8.5 GHz. The modulation frequency is limited by the capacitance of the bondpad and the corresponding differential resistance of the VCSEL. For obtaining higher frequencies the capacitance of the selectively oxidized VCSEL should be minimized and the differential resistance should be lowered. Moreover, we have found inferior modulation characteristics of proton implanted as compared to polyimide planarized VCSELs.

References

[1] K. L. Lear, V. M. Hietala, A. Mar, K. D. Choquette, H. Q. Hou, and R. P. Schneider, Jr., "High frequency modulation of oxide-confined vertical-cavity surface emitting lasers", *IEEE J. Lightwave Technol.*, vol. 32, pp. 457–458, 1996.

[2] F. Eberhard and M. Schauler "Sputter etching of GaAs and GaN", *Annual Report 1995, Dept. of Optoelectronics, University of Ulm*, pp. 96–101, 1996.

Broad-Area High-Power Top Surface Emitting Laser Diodes

Martin Grabherr

Top surface emitting vertical-cavity lasers with active diameters from 4 to 150 µm have been investigated to estimate the limits of maximum cw output powers for single devices.

1. Introduction

In the past few years, performance of vertical-cavity surface-emitting laser diodes (VCSELs) has been improved dramatically. Threshold current densities and threshold voltages are as low as 200 A/cm^2 [1] and 50 mV [2] above corresponding bandgap voltages, respectively. Wallplug efficiencies exhibit 50 % [3, P-60] for small device diameters of around 6 µm. With maximum output powers of a few mW these devices are well suited for optical data transmission. Maximum output power is limited by thermal roll over and thus by dissipated power, which can be minimized by low series resistances of the Bragg reflectors and current apertures formed by selective oxidation of AlAs layers reducing nonradiative recombinations. High optical output powers should now be attainable with broad-area devices.

2. Device Structure

A schematic of the investigated devices is depicted in Fig. 1. P- and n-type Bragg reflectors surround the active region consisting of 3 InGaAs quantum wells, GaAs barriers, and AlGaAs cladding layers. On top of the mesa a TiPtAu ring forms the p-type contact, whereas GeNiAu is evaporated on the substrate as n-type contact. The devices are attached junction up to a copper block using silver paste. Substrate thickness is around 400 µm. The copper block can be heated or cooled in order to control heat sink temperature.

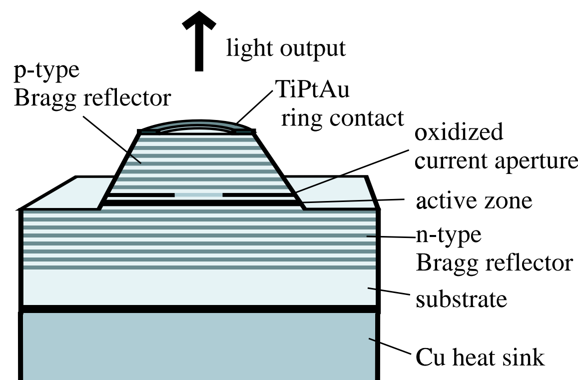

Fig. 1. Cross section of a top emitting VCSEL mounted junction up on copper heat sink.

3. Fundamental Characteristics and Modeling of Output Powers

To estimate attainable output powers for top surface emitting VCSELs, simple modeling of output power as a function of laser current i has been chosen according to

$$P = \hbar\omega/q \cdot \eta_d \cdot (i - i_{th}) \cdot f(\Delta T) \quad , \tag{1}$$

where $\hbar\omega$ denotes the photon energy, q is the electron charge, η_d the differential quantum efficiency, and i_{th} the threshold current. Laser heating is taken into account by the function $f(\Delta T)$ and the intrinsic temperature rise ΔT can be determined from the thermal resistance and the dissipated power as

$$\Delta T = R_{th} \cdot P_{diss} \quad . \tag{2}$$

Assuming a linearized current-voltage characteristics with a constant differential resistance R_d and a kink voltage V_k, the dissipated power is written as

$$P_{diss} = (V_k + R_d \cdot i) \cdot i - P \quad . \tag{3}$$

From the experiments, the parameters i_{th}, R_{th}, and R_d can all be expressed as functions of the device diameter D_{act} and therefore output power is now only a function of driving current and laser size. The intrinsic temperature rise ΔT cannot be directly measured, therefore the thermal resistance in (2) has to be calculated from the quotients of wavelength shifts $\Delta\lambda$ with both dissipated power ΔP_{diss} and heat sink temperature T_{hs} as

$$R_{th} = \frac{\Delta\lambda}{\Delta P}\left(\frac{\Delta\lambda}{\Delta T_{hs}}\right)^{-1} \quad . \tag{4}$$

Fig. 2 depicts the wavelength shift with dissipated power for a 150 μm active diameter device, showing a high degree of linearity. The device emits in multiple transverse modes among which a single mode has to be recorded with an optical spectrum analyzer to obtain the wavelength shift. This procedure is also applied for observing the red shift with increasing heat sink temperature for constant dissipated power in Fig. 3, which directly gives the slope of wavelength deviation with intrinsic temperature. Due to the dependence of refractive indices on temperature, this

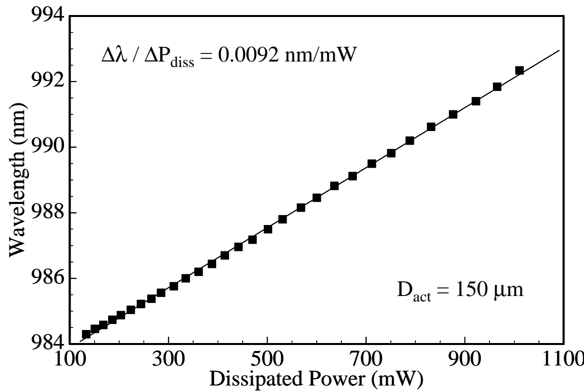

Fig. 2. Wavelength shift with dissipated power for a 150 μm diameter device.

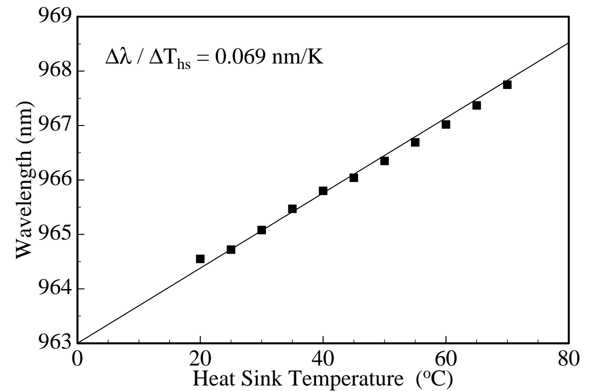

Fig. 3. Tuning of the emission wavelength with varying heat sink temperature.

slope is constant for all devices with identical layer structure independent of the active diameter. For the given example a thermal resistance of 133 K/W is calculated. Measurements for device diameters from 4 to 150 μm result in an inversely proportional behavior of thermal resistance with device diameter in accordance with a simple theoretical model [4] in which the thermal resistance is related to the thermal conductivity λ_c by

$$R_{th} = \frac{1}{2\lambda_c D_{act}} \quad . \tag{5}$$

A fit to the experimental data, shown in Fig. 4, determines λ_c to 40.4 W/(m·K) which is close to the value 44 W/(m·K) usually taken for the GaAs substrate material. Using a resistance network

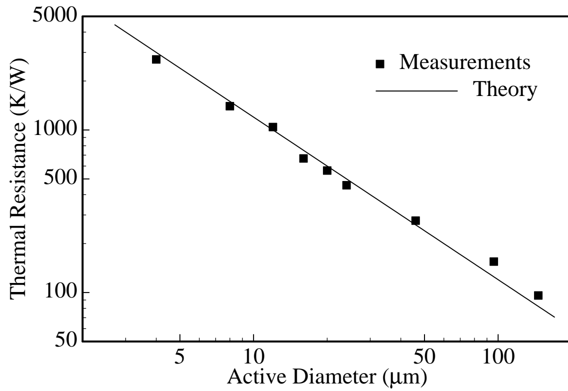

Fig. 4. Thermal resistance of top surface emitting VCSELs versus device diameter.

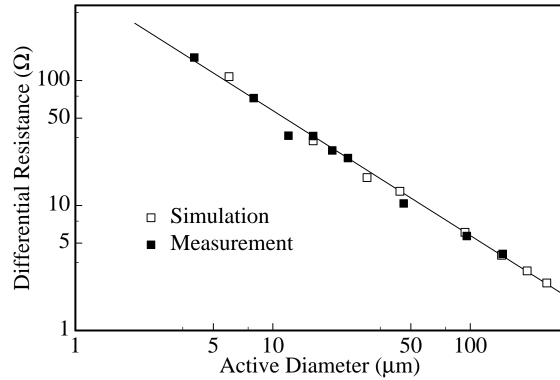

Fig. 5. Differential resistance of the investigated devices as a function of avtive diameters.

model [5], series resistances for investigated device structures, contact geometries, and doping concentrations have been simulated. The results for a broad range of device diameters are in good agreement with the measurements as seen in Fig. 5. Again we see an inversely proportional dependence with active diameter, which is not directly expected because of the increase of the active area with D_{act}^2. This effect can be explained by current crowding at the oxide aperture with a circumference being proportional to D_{act}. The dependence in Fig. 5 ca be fitted with a single parameter as

$$R_d = \frac{575\ \Omega\mu\text{m}}{D_{act}} \quad . \tag{6}$$

Another input parameter for the simulation is the threshold current versus active diameter, depicted in Fig. 6. Again it is expected that the threshold current increases with the squared diameter, but this is only confirmed for device sizes below 40 μm. For larger diameters an almost linear increase is seen from the measurements, again being due to the inhomogeneous current density distribution in the active area. To describe the thermal behavior of the output characteristics, the temperature T_{off} at the thermal turn off point is calculated from the light-current curves presented in Fig. 7. We obtain an almost constant value $T_{off} = 200\,°\text{C}$ for all device sizes and for different heat sink temperatures T_{hs}. The function describing thermal behavior in the simulation is simply assumed to be

$$f(\Delta T) = 1 - \frac{\Delta T + T_{hs}}{T_{off}} \quad , \tag{7}$$

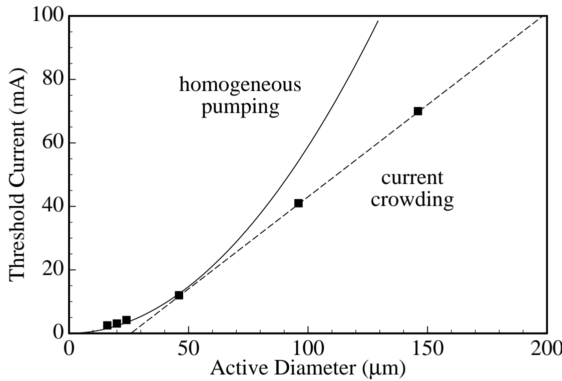

Fig. 6. Threshold current versus device diameters.

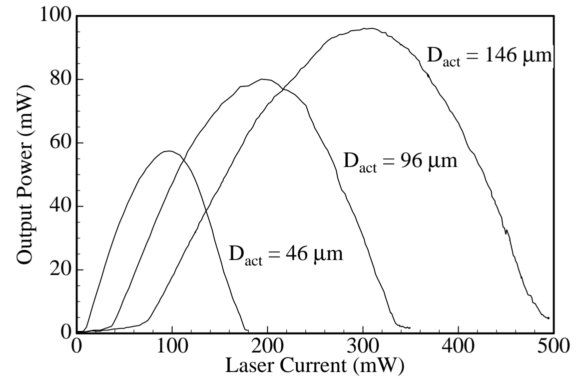

Fig. 7. Output characteristics and thermal turn off for different device diameters.

taking a constant heat sink temperature into account and enforcing $P = 0$ at $T = T_{off}$ while neglecting temperature dependencies of all other parameters.

4. Comparison of Modeling and Measurements

Taking the emission wavelength of 990 nm and a differential efficiency of 90 % into account, the output characteristics can be simulated using equations (1)–(3) and the experimental data according to (5)–(7) and Fig. 6. The good agreement between measurement and simulation in Fig. 8 for a 50 μm device confirms the assumptions used in the model. For this device maximum wallplug efficiency is 40 % at 40 mW output power. Maximum output power at thermal roll over is 78 mW. Performing these simulations for various device diameters, a linear increase of maximum output power with device diameter is expected, as plotted in Fig. 9. The experimental data only show a sublinear increase due to the injection of carriers near the center of the active region where mo stimulated emission occurs. Maximum wallplug efficiencies are as high as 40 % for device sizes up to 50 μm and decrease down to 20 % for devices with 150 μm active diameter.

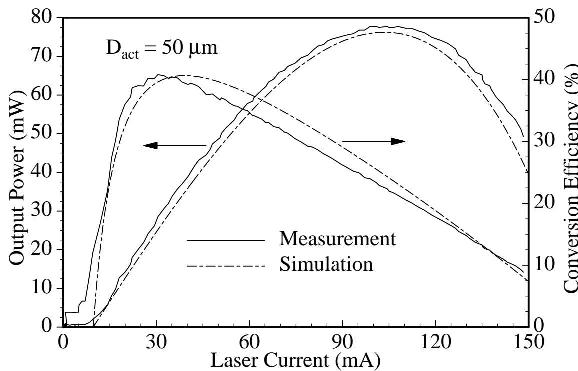

Fig. 8. Comparison of measured and simulated output characteristics of a 50 μm active diameter device.

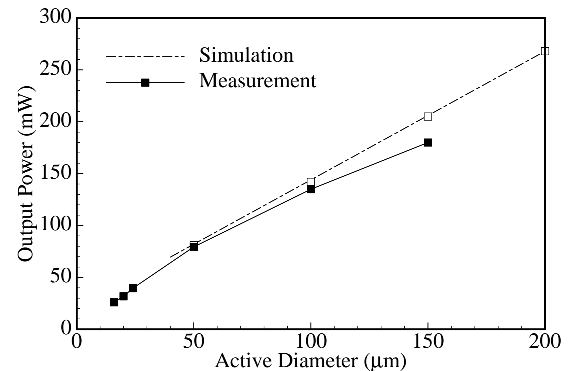

Fig. 9. Maximum output power for different device sizes.

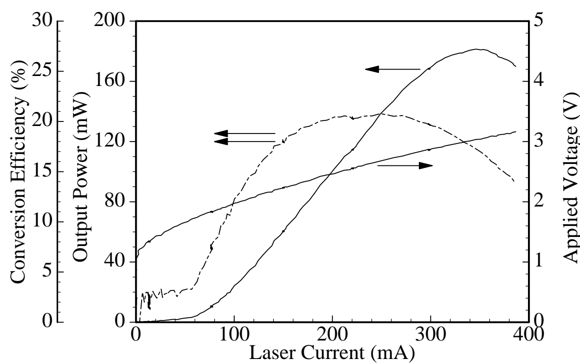

Fig. 10. CW output characteristics of a device with 150 μm active diameter.

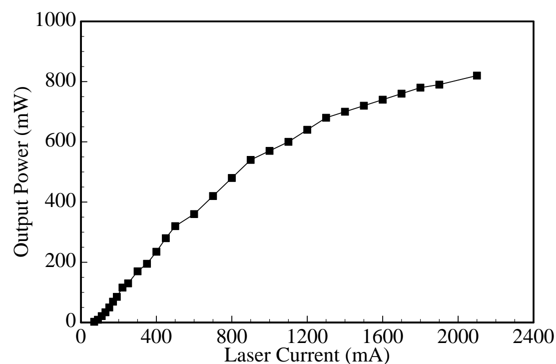

Fig. 11. Pulsed operation with maximum pulse power of 820 mW of the device from Fig. 10.

5. Maximum Output Powers for CW and Pulsed Operation

The characteristics of the devices with the highest cw output power experimentally observed are presented in Fig. 10. At a laser current of 350 mA, 180 mW output power is reached at room temperature with a wallplug efficiency of 15 %. The broad current range where high conversion efficiency is obtained is due to the low series resistance of 3.8 Ω and an optimized tuning of resonance wavelength and gain peak. Therefore 160 mW output power is achieved at maximum wallplug efficiency of 20 %. Fig. 11 shows the importance of further improvements of mounting technologies and thus reductions of thermal resistance. Pulsed operation results in 820 mW output power at 2.1 A current for a pulse width of 1 μs and a duty cycle of 1:100. The relatively large pulse width and accompanied heating still gives rise to the power saturation seen in Fig. 11.

6. Outlook

Further reductions of dissipated power by decreasing the differential resistance and more homogeneous current density distributions are expected for bottom emitting devices. Together with junction down soldering of those devices and thus lower thermal resistances, higher output powers for VCSELs are foreseeable.

References

[1] P. D. Dapkus, M. H. MacDougal, G. M. Yang, A. E. Bond, C. Lin, D. Tishinin, V. Pudikov, Y. Cheng, and K. Uppal, "Ultralow threshold current lasers", in Proc*Conf. on Lasers and Electro-Optics CLEO'96*, Anaheim, CA, USA, pp. 357–358, 1996.

[2] K. D. Choquette, R. P. Schneider, Jr., K. L. Lear, and K. M. Geib, "Low threshold voltage vertical-cavity lasers fabricated by selective oxidation", *Electron. Lett.*, vol. 30, pp. 2043–2044, 1994.

[3] K. L. Lear, K. D. Choquette, R. P. Schneider, Jr., S. P. Kilcoyne, and K. M. Geib, "Selectively oxidised vertical-cavity surface-emitting lasers with 50 % power conversion efficiency", *Electron. Lett.*, vol. 31, pp. 208–209, 1995.

[4] W. Nakwaski and M. Osinski, "Thermal resistance of top-surface emitting vertical-cavity semiconductor lasers and monolithic two-dimensional arrays", *Electron. Lett.*, vol. 28, pp. 572–574, 1992.

[5] R. Michalzik and K. J. Ebeling, "Modeling and design of proton-implanted ultralow-threshold vertical-cavity laser diodes", *IEEE J. Quantum Electron.*, vol. 29, pp. 1963–1974, 1993.

Measurement of Ultrafast Oscillations in Vertical-Cavity Lasers after Pulse Perturbation

Dieter Wiedenmann

The temporally resolved emission of a running vertical-cavity surface-emitting laser (VCSEL) after perturbation with a short optical pulse has been measured with a high resolution up-conversion setup. Transverse multimode devices show very fast oscillations of the laser emission. It seems that modelocking between the titanium sapphire (Ti:Sp) pulse and the VCSEL emission is achieved, and the fast oscillations are attributed to interference between the transverse VCSEL modes. Measurements of mode spacing and oscillation frequency show good agreement.

1. Introduction

Vertical-cavity lasers are predestined devices for high speed optical communications. The small cavity volume of VCSELs promotes high photon densities and therefore high resonance frequencies of the devices. There are some reports on ultrafast oscillations in VCSELs with frequencies exceeding 50 GHz [1, 2]. Normally they are attributed to ultrafast relaxation oscillations based on the oscillatory energy transfer between the electronic and the photonic system. But they are far beyond measurements of relative intensity noise (RIN) and small signal modulation [3]. Therefore we made some investigations of the transient response of a running VCSEL to a perturbation of the intrinsic photon density. In this paper our investigations are restricted to perturbations with pulses having the same photon energy as the VCSEL, in order to get no transient carrier heating caused by carrier-carrier scattering.

2. Experimental Setup

Fig. 1 shows the measurement setup. The sample is mounted such that a 100 fs pulse from the Ti:Sp laser is coupled from the substrate side into the VCSEL cavity, and the device luminescence is monitored at the epitaxial side. In this setup we have the advantage that the intense backscattered light from the mirror of the VCSEL does not cause problems in the detection system. The laser luminescence can be measured either by an optical sampling scope with a time resolution of 30 ps or by up-conversion [4, 5]. For that purpose the VCSEL output and a fraction of the Ti:Sp pulse are collimated on a $LiIO_3$ crystal and mixed using Type I phase-matching. The polarization plane of the linearly polarized Ti:Sp pulse can be rotated with a half wave plate (HWP) in order to match the polarization of the VCSEL emission, which is itself not defined due to the circular aperture of the cavity. The measurement setup is polarization selective, therefore we are able to measure the VCSEL emission splitted in two polarizations. Time resolution of the up-conversion setup is 200 fs and the maximum possible measurement time of 100 ps is limited by the optical delay line.

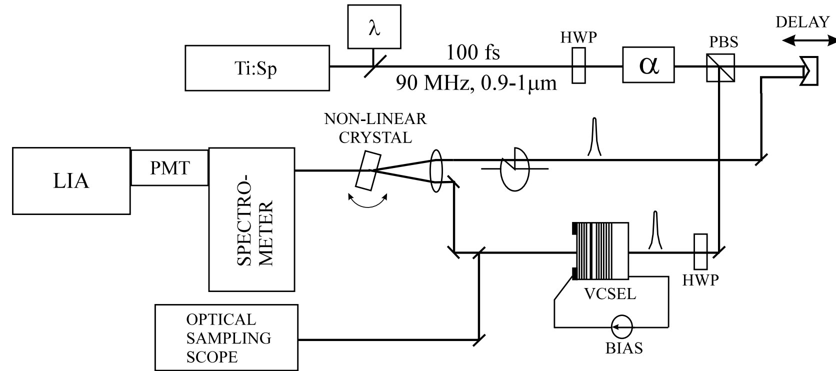

Fig. 1. Experimental setup for measurement of transient resolved VCSEL emission after pulse perturbation. (LIA: lock-in amplifier, PMT: photomultiplier tube, PBS: polarizing beam splitter.)

3. Device Structure

We have investigated VCSELs with 3 $In_{0.2}Ga_{0.8}As$ quantum wells emitting in the 980 nm wavelength regime [P-54]. The devices are grown on n-doped GaAs substrate, which is transparent for the emission wavelength of the device. Therefore we are able to couple an optical pulse through the substrate into the active region of the VCSEL with the same wavelength as the emission wavelength of the device. Current is injected through a ring contact on top of the device and through the substrate. Current confinement is achieved either through proton implantation in the top mirror or through selective oxidation of a thin AlAs layer after mesa etching. The optical fields of proton-implanted devices are gain and thermally induced index guided, whereas oxidized devices are mainly index guided by the oxide aperture.

4. Measurement of Transverse Single-mode VCSEL

First we couple a short optical pulse from the Ti:Sp Laser into a transverse single-mode oxidized VCSEL. The VCSEL is electrically biased above threshold, emitting a linearly p-polarized beam. When a s-polarized Ti:Sp pulse with the same wavelength as the VCSEL is coupled into the VCSEL cavity, we can observe the behavior shown in Fig. 2. The VCSEL luminescence, split into the p- and s-polarizations, is measured with the optical sampling scope because of the limited measurement time intervall of the up-conversion setup. There is a fast decay in output power for the p-polarization. For high pulse energies the VCSEL is even switched off. After some time for recovery, the VCSEL switches on again, and we can observe relaxation oscillations. This behavior was predicted by Koch [6] for pulses with excess photon energy, due to pulse induced carrier heating. In our case the emission wavelength of the VCSEL and the Ti:Sp pulse are the same and accordingly we have no carrier heating. A simple explanation for the interruption of laser action is a strong reduction in gain induced by stimulated electron hole recombination after pulse perturbation. Surprisingly, we can observe the same behavior if we have a Ti:Sp pulse wavelength below the emission wavelength of the VCSEL. Here, stimulated electron hole recombination/generation is not resonant and due to lower gain/higher absorption, we should get the above mentioned transient carrier heating. In the s-polarization we can see the transmitted pulse from the Ti:Sp laser, which is filtered by the VCSEL cavity. If the perturbation pulse

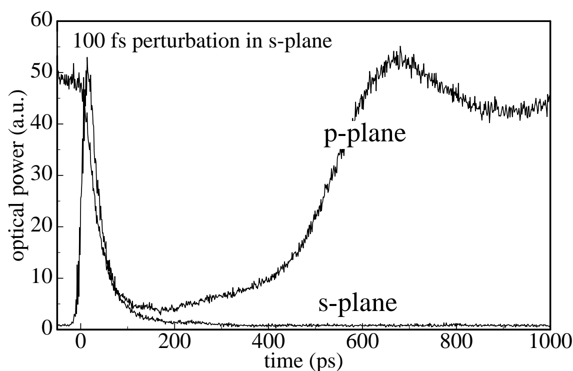

Fig. 2. VCSEL emission in p- and s-polarization plane measured with optical sampling scope.

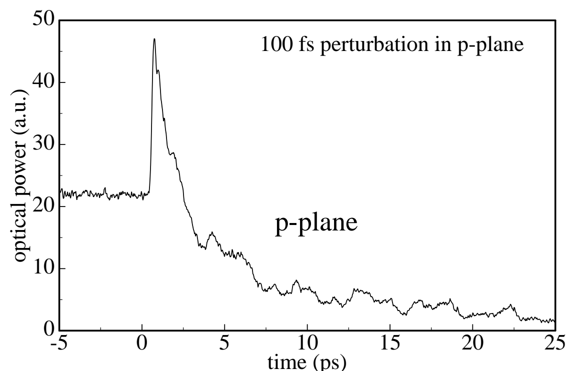

Fig. 3. VCSEL emission in p-polarization after perturbation with p-polarized light. The high resolution up-conversion setup is used for meaurement.

has the same polarization as the VCSEL output, we can observe a strong overshoot in VCSEL emission after the pulse is coupled into the VCSEL cavity. Then a decay in output power followed by relaxation oscillations similar to that in Fig. 2 can be observed. This behaviour is shown in Fig. 3 where the different time scale compared to Fig. 2 should be noted. As expected, in the s-polarized direction no emission at all can be seen.

5. Measurement of Transverse Multimode VCSEL

We now couple the pulse from the Ti:Sp laser into a transverse multimode protonimplanted VCSEL, being polarized in p-direction for all lasing modes. First the perturbation pulse is polarized orthogonal to the VCSEL emission, and we observe a behavior similar to the single-mode VCSEL shown in Fig. 2. If the pulse has the same polarization as the VCSEL we get the results shown in Fig. 4. Very fast oscillations of the emission after perturbation can be seen. The measurement is done for different bias currents. Oscillation frequency is determined to range between 190 GHz and 245 GHz after fast Fourier transformation (FFT) of the signal. If we compare these data with the mode spacing of the VCSEL, varying between 0.58 nm and 0.8 nm at these currents as shown in Fig. 5, a very good agreement with the oscillation frequencies can be seen. In this case, measurements are done with proton-implanted device, where the mode spacing is a function of bias current due to thermal lensing. The slight difference between mode spacing and calculated FFT spectra might be explained by the time averaging of the optical spectrum analyzer. The oscillations are caused by interference of different modes of the VCSEL. A requirement for observing the interference of the modes with this sampling measurement setup is a stable phase relation between the modes and the pulse from the modelocked Ti:Sp laser. Otherwise the sampled data at a fixed time would vary with the phase of the modes relative to the phase of the Ti:Sp laser pulse, and therefore the response of the VCSEL emission to the pulse perturbation would exhibit a decay without oscillations.

All measurements show that it seems impossible to force the VCSEL emission into a different polarization plane although there are no obvious polarization selective elements in the VCSEL cavity.

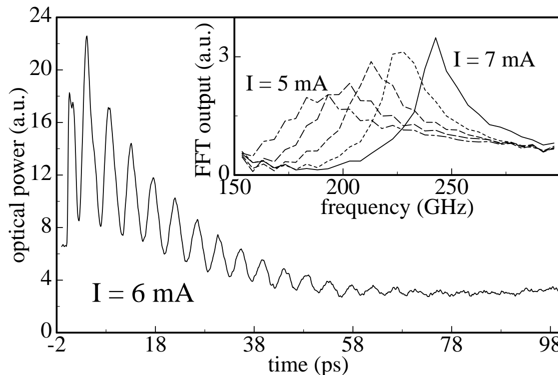

Fig. 4. Emission of multimode VCSEL in p-polarization after perturbation with p-polarized 100 fs pulse and corresponding FFT spectra for different bias currents of the laser.

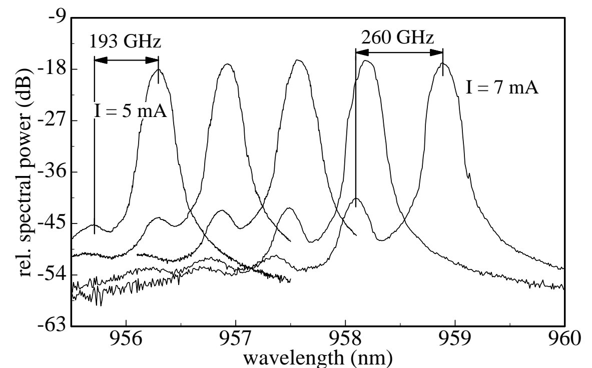

Fig. 5. Emission spectra of the multimode VCSEL in cw-operation for different bias currents showing increasing transverse mode spacings.

6. Conclusion

We have shown ultrafast oscillations in VCSEL emission after perturbation with a short optical pulse having the same wavelength and polarization as the VCSEL. Comparison between oscillation frequency and VCSEL mode spacing reveals that these oscillations are due to interference between different transverse modes of the VCSEL. The optical phase of the different transverse modes are phase locked to the perturbing pulse.

References

[1] D. Tauber, G. Wang, R. S. Geels, J. E. Bowers, and L. A. Coldren, "Large and small signal dynamics of vertical cavity surface emitting lasers", *Appl. Phys. Lett.*, vol. 62, pp. 325–327, 1993.

[2] M. Koch, J. Shah, M. Tsuchiya, H. Wang, T. C. Damen, J.E. Cunningham, and W. Y. Jan, "Ultrafast oscillations in the optical emission from a semiconductor microcavity", *Ultrafast Phenomena X*, Springer Series in Chemical Physics, vol. 62, pp. 425–426, 1996.

[3] K. L. Lear, A. Mar, K. D. Choquette, S. P. Kilcoyne, R.¶. Schneider, Jr., and K. M. Geib, "High-frequency modulation of oxide-confined vertical cavity surface emitting lasers", *Electron. Lett.*, vol. 32, pp. 457–458, 1996.

[4] H. Mahr and M. D. Hirsch, "An optical upconversion lightgate with picosecond resolution", *Opt. Commun.*, vol. 13, pp. 96–98, 1975.

[5] J. Shah, "Ultrafast luminescence spectroscopy using sum frequency generation", *IEEE J. Quantum Electron.*, vol. 24, pp. 276–288, 1988.

[6] F. Jahnke and S. Koch, "Ultrafast intensity switching and nonthermal carrier effects in semiconductor microcavity lasers", *Appl. Phys. Lett.*, vol. 67, pp. 2278–2280, 1995.

Bias-Free Data Transmission Using Single-Mode GaAs VCSELs at $\lambda = 835$ nm

Peter Schnitzer

Bias-free 1 Gb/s pseudo-random data transmission using laterally oxidized single-mode GaAs vertical-cavity surface-emitting laser diodes is demonstrated and compared to biased modulation. Bit error rates of 10^{-11} *obtained for* -28 *dBm received optical power make these devices very attractive for optical interconnection.*

1. Introduction

Over the past few years, short wavelength ($\lambda = 850, 980$ nm) vertical-cavity surface emitting lasers (VCSELs) have improved considerably in performance. For selectively oxidized VCSELs, high wall-plug efficiencies of 57 % [P-60] combined with extremely low threshold currents of smaller than $100\,\mu$A [1] have been demonstrated. Transmission at data rates as high as 10 Gb/s with proton-implanted InGaAs VCSELs [P-14] as well as 16.3 GHz modulation bandwidth of oxidized InGaAs VCSELs [2] have been reported. Presently, VCSELs are being investigated as transmitters for optical interconnections such as in high-speed board-to-board communication and parallel short range multi-gigabit data links. Bias-free data transmission is highly desirable for reducing power consumption and to simplify laser driving circuits. In this report, we investigate bias-free 1 Gb/s non-return-to zero (NRZ) pseudo-random bit sequence (PRBS) transmission with $2^{31} - 1$ word length using a laterally oxidized single-mode GaAs VCSEL source. The results of non-biased data transmission are compared to those obtained for biased operation.

2. Device Structure

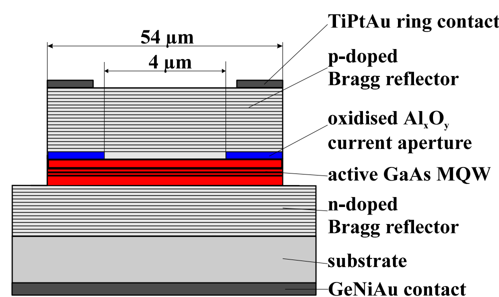

Fig. 1. Cross-sectional view of selectively oxidized GaAs VCSEL.

The layer structure of the molecular beam epitaxially grown GaAs VCSEL used for the experiments is schematically illustrated in Fig. 1. The one-wavelength thick cavity contains a $\lambda/2$

central region with three 8 nm thick active GaAs quantum wells embedded in $Al_{0.2}Ga_{0.8}As$ barriers and surrounded by $\lambda/4$ $Al_{0.5}Ga_{0.5}As$ layers for efficient carrier confinement. The bottom Bragg reflector consists of 28.5 n-type Si-doped $AlAs/Al_{0.2}Ga_{0.8}As$ quarter wavelength layer pairs. To reduce the electrical resistance, the 24 pairs $Al_{0.9}Ga_{0.1}As/Al_{0.2}Ga_{0.8}As$ p-type C-doped step-graded top reflector has an optimized modulation and δ-doping profile. As the lowest layer of the p-doped top Bragg reflector, a single 30 nm thick AlAs layer was grown for selective oxidation. The VCSEL studied has an active diameter of about 4 μm and emits at 836 nm wavelength.

3. Experiment

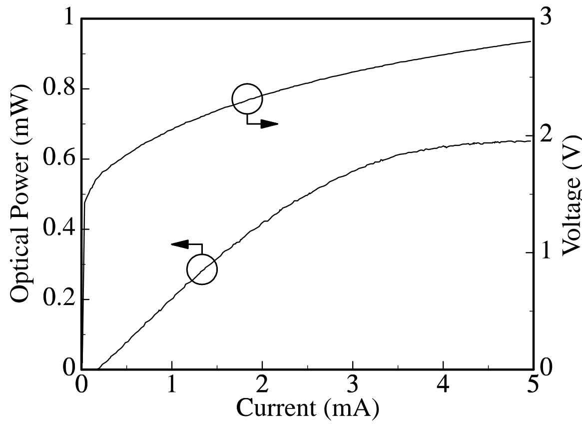

Fig. 2. Output charactristics of a 4 μm diameter selectively oxidized GaAs VCSEL.

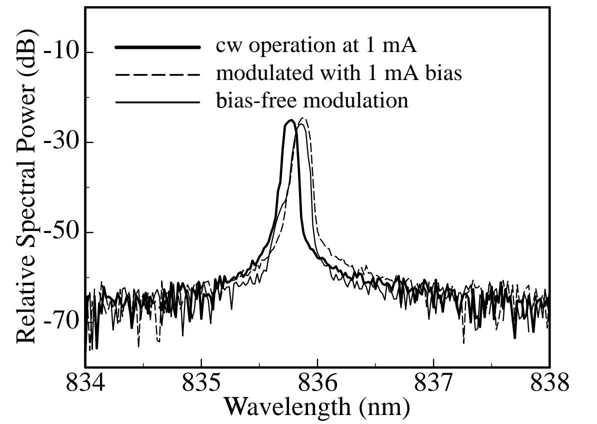

Fig. 3. Optical spetrca for biased and bias-free modulation.

The VCSEL is wire bonded to an SMA socket and either driven with a cw current or modulated with a PRBS signal at 1 Gb/s NRZ data rate. Fig. 2 shows the output characteristics of the laser diode. The threshold current is 250 μA at a threshold voltage as low as 1.7 V, while an output power of 0.55 mW is obtained at 3 mA.

Fig. 3 depicts the spectra recorded for bias-free 1 Gb/s modulation with $V_{pp} = 2$ V and 1 Gb/s modulation at 1 mA bias current and $V_{pp} = 0.5$ V. All spectra indicate single-mode emission at 836 nm with a side mode suppression exceeding 30 dB. Fig. 4 illustrates the experimental setup. For data transmission experiments, the laser is either directly driven by a pattern generator at 1 Gb/s with $V_{pp} = 2$ V without any additional bias, or a bias current of 1 mA and 1 Gb/s modulation with $V_{pp} = 0.5$ V are combined in a bias-tee and fed to the VCSEL. The emitted light is butt-coupled to a 50 μm core diameter graded index multimode fiber. After 100 m transmission, the signal is passed through a variable attenuator and detected with a Germanium avalanche photodiode and preamplified in two stages.

Fig. 5 shows the eye diagrams for biased and bias-free 1 Gb/s PRBS modulation. In the diagram of the biased VCSEL the eye is wide open and symmetric. For non-biased modulation we observe a turn-on delay of $\tau_d \approx 150$ ps and an asymmetric eye shape due to a significant relaxation oscillation peak. For an average driving current of 1 mA inferred from the spectra in Fig. 3 one can estimate a logic on-state current of about $I_p = 1.55$ mA from the nonlinear

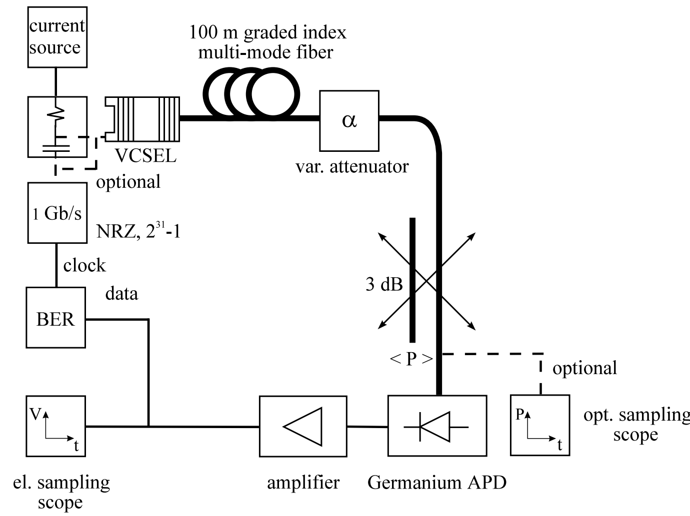

Fig. 4. Experimental setup.

I-*V* characteristics displayed in Fig. 2, taking an on-off ratio of 50 % into account. The turn-on delay is then calculated as

$$\tau_d = \tau_e \ln \frac{I_p}{I_p - I_{th}} = 150 \text{ ps}$$

using a threshold current of 250 μA and assuming a carrier lifetime of $\tau_e = 1$ ns. This result is in reasonable accordance with the experimental observation in Fig. 5. The results of the transmission experiments are summarized in the bit error rate (BER) characteristics in Fig. 6, where circles denote biased 1 Gb/s PRBS modulation while squares denote bias-free transmission over 100 m of multimode fiber. The bit error rate for 1 Gb/s remains better than 10^{-11} for biased as well as for bias-free operation. The received optical power necessary for a bit-error

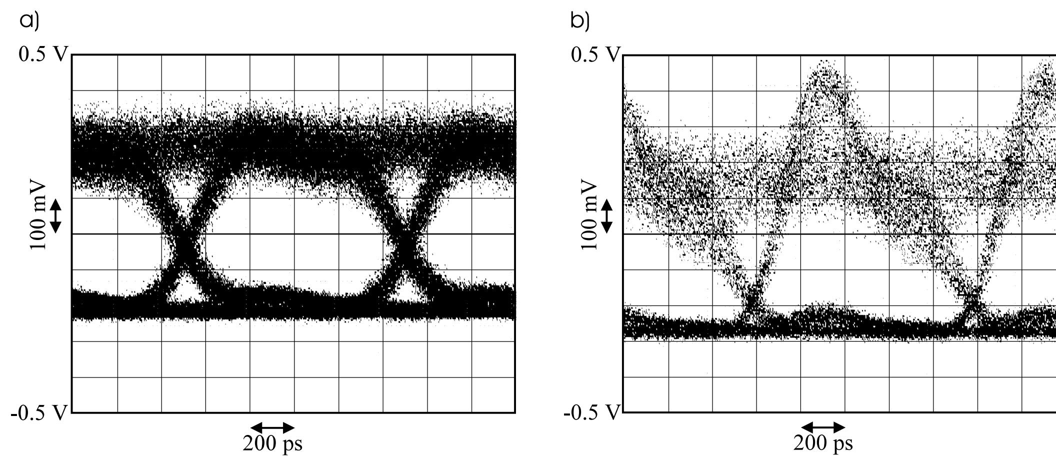

Fig. 5. Eye diagrams for a) biased modulation at 1 Gb/s $2^{31} - 1$ PRBS and b) bias-free modulation at 1 Gb/s $2^{31} - 1$ PRBS.

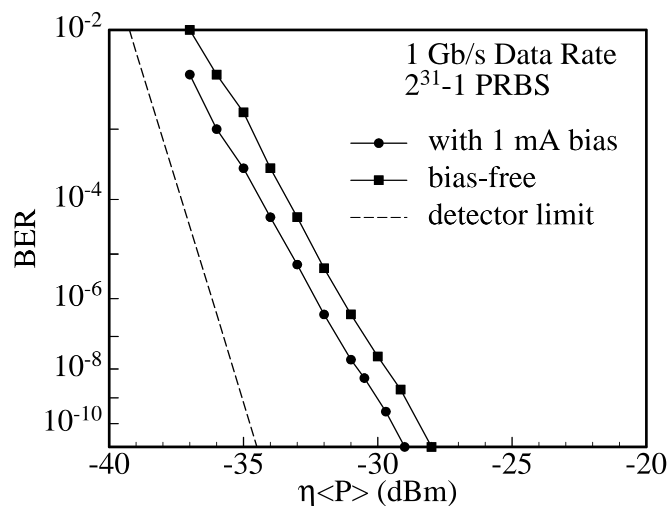

Fig. 6. Bit error rate measurement at 1 Gb/s and $2^{31} - 1$ word length.

rate of $< 10^{-11}$ is as low as -29 dBm for biased operation, while bias-free operation shows a penalty of 1 dB nearly independent of the BER. Also indicated in Fig. 6 is the APD detector noise limit.

4. Conclusion

For the first time we have successfully demonstrated bias-free data transmission with $2^{31} - 1$ PRBS signals at 1 Gb/s data rate using a high performance GaAs VCSEL source emitting in the 800 to 850 nm wavelength regime [P-63]. A BER of 10^{-11} is obtained at a received power of -29 dBm for biased and -28 dBm for bias-free transmission over 100 m graded index multimode fiber. Bias-free operation greatly facilitates optical interconnection systems.

References

[1] Y. Hayashi, T. Mukaihara, N. Hatori, N. Ohnoki, A. Matsutani, F. Koyama, and K. Iga, "Lasing characteristics of low-threshold oxide confinement InGaAs-GaAlAs vertical-cavity surface-emitting lasers", *IEEE Photon. Technol. Lett.*, vol. 7, pp. 1324–1326, 1995.

[2] K. L. Lear, A. Mar, K. D. Choquette, S. P. Kilcoyne, R. P. Schneider, Jr., and K. M. Geib, "High-frequency modulation of oxide confined vertical cavity surface emitting lasers", *Electron. Lett.*, vol. 32, pp. 457–458, 1996.

A Model of an Optical Communication System

Roger King

The basic principles that underlie the analysis and design of well established digital communication systems [1] are adapted to optical communication systems.

1. Introduction

In the design of communication systems for transmitting information through physical channels, it is convenient to construct mathematical models that reflect the most important characteristics of the transmission medium. Then, the mathematical model for the channel is used in the design of the channel modulator at the transmitter and the demodulator at the receiver. In the case of optical communication systems a model may also help to analyze the laser performance as the characteristics of the output light cannot be measured directly; only the detected electrical signal is a measurable quantity.

2. Elements of an Optical Communication System

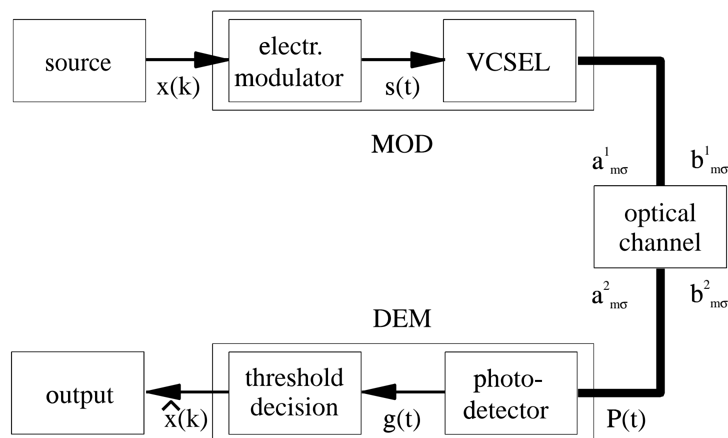

Fig. 1. Basic elements of a digital optical communication system.

Fig. 1 illustrates the functional diagram and the basic elements of a digital optical communication system employing a vertical-cavity surface emitting laser (VCSEL). The information source output $x(k)$ is a digital signal that is discrete in time and often has two output characters. This binary sequence is passed to the digital modulator MOD, which serves as the interface to the optical channel. Since the communication channel is capable of transmitting electromagnetic signals, the primary purpose of the modulator is to map the binary information sequence first into the electrical signal $s(t)$ and afterwards into the optical signal.

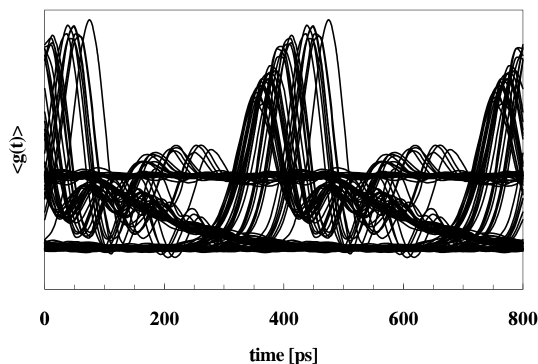

Fig. 2. Eye diagram of a 2.5 Gb/s PRBS 7. The output signal of the VCSEL suffers from the strong relaxation oscillation and the pattern dependence of the turn-on delay.

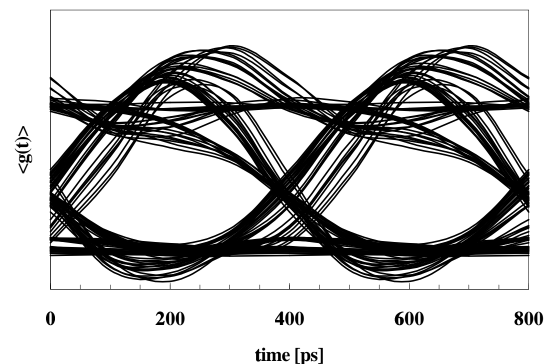

Fig. 3. A narrowband demodulator suppresses the relaxation oscillations shown in the left picture. Still there is the dependence of the turn-on delay on the transmitted pattern.

Mapping the electrical signal into an optical signal can be favorably done by modulating the intensity of a VCSEL with the laser drive current. Turn-on delay and relaxation oscillations are responsible for the intrinsic distortions of the VCSEL, especially for bias-free modulation (see pp. 46–49). Fig. 2 shows an example of an measured eye diagram of the detected electrical signal for 2.5 Gb/s PRBS 7 (pseudo random bit sequence with $2^7 - 1$ different patterns) modulation and a broadband (10 GHz) demodulator. Fortunately the strong relaxation oscillations can be suppressed by using a narrowband (2 GHz) detector as indicated in Fig. 3, but there is still the dependence of the turn-on delay on the transmitted pattern.

The communication channel is the physical medium used to send the signal from the transmitter to the receiver. The essential feature is that the transmitted signal is corrupted in a random manner by a variety of possible mechanisms.

The light signal is treated in a classical manner with normalized modal baseband amplitudes $a^j_{m\sigma}(t)$, which have a magnitude equal to the square root of the optical power and a phase equal to a selected observable such as the electric field [2]. If at some reference plane the reflected waves are characterized by a normalized amplitude $b^j_{m\sigma}(t)$, the net power flowing into port j is

$$P^j(t) = \sum_{m\sigma} \left(|a^j_{m\sigma}(t)|^2 - |b^j_{m\sigma}(t)|^2 \right) \quad , \tag{1}$$

where m is the mode index and σ is the polarization index.

Noise and distortions of the semiconductor laser signal are altered considerably due to the interaction of the laser with the optical channel. The influence of partition noise [3] is important if the channel exhibits material dispersion or if the transmission loss is wavelength-dependent. An interaction with the active medium of the laser occurs if some light is reflected from the channel back to the laser yielding noise and distortions [4]. Forward transmission interferences may occur between different fiber modes (modal noise effects) yielding, also, noise and distortions with respect to the transmitted optical power.

At the receiving end of the digital communication system, the demodulator DEM processes the transmitted waveforms corrupted by the channel and reduces the waveforms to a sequence of numbers $\hat{x}(k)$ that represent estimates of the transmitted data symbols $x(k)$.

A measure of how well the demodulator performs is the frequency with which errors occur in the detected sequence. More precisely, the average probability of a bit error at the output of the demodulator is a measure of the overall system performance. In general, the probability of error is a function of the code characteristics, the types of waveforms used to transmit the information over the channel, the transmitter power, the characteristics of the channel, i.e. the amount of noise, the nature of interference, etc., and the method of demodulation. Some items will be discussed in more detail in the following section.

3. Detection Errors due to Noise

In the previous section light is treated in a completely classical manner; describing the detection of light there is no necessity to deal with quantization of the electromagnetic fields, only the interaction of the classical field and matter has to be quantized [5].

When light, having a deterministic variation of intensity over space and time, is incident on a photodetector, the fluctuations of the photocounts obey a Poisson statistics. In most problems of real interest, however, the light wave incident on the photosurface has stochastic attributes. Any stochastic fluctuations of the classical intensity $P(t)$ do influence the statistical properties of the photon generation process. According to this, the relationship between the variance of the detected electrical signal $\sigma_g^2(t)$ and the averaged received optical power $\alpha\langle P^{ref}(t)\rangle$ has a physical interpretation. The variance consists of three distinct terms:

$$\sigma_g^2(t) = \langle \delta g(t)^2 \rangle = \sigma_{receiver}^2 + \alpha\sigma_{shot}^2(t) + \alpha^2\sigma_{excess}^2(t) \quad . \tag{2}$$

The first term represents the receiver noise, the second can be interpreted as representing the effects of pure Poisson noise introduced by the random interaction of light and matter, also called shot noise. The third term, because it is proportional to the variance of the fluctuations of the incident intensity, is the classically expected result in the absence of any noise associated with the interaction of light and matter (excess fluctuations).

Fig. 4 shows the dependence of the bit error rate (BER) on the averaged received optical power $\alpha\langle P^{ref}(t)\rangle$ with different weighting of receiver, shot and excess noise. Strong classical light fluctuations result in a bit error floor, the performance of the demodulator cannot be improved by increasing the transmitted optical power. In accordance with the simulated BERs, Fig. 4 d) presents a measured BER curve. Excess noise, as a result of strong modal noise created in the optical channel, dominates the BER for power levels above −24 dBm.

4. Conclusions

The simplest mathematical model for a communication channel is the additive noise channel, illustrated in the equation

$$g(t) = \alpha s(t) + n_{receiver}(t) \quad . \tag{3}$$

If the noise is introduced primarily by electronic components and amplifiers at the receiver, it may be characterized as thermal noise. This type of noise is characterized statistically as a Gaussian noise process. Channel attenuation is easily incorporated in the attenuation factor α.

The additive gaussian noise channel does not adequately characterize many of the optical channels encountered in practice. A more accurate model has been presented in this text. The

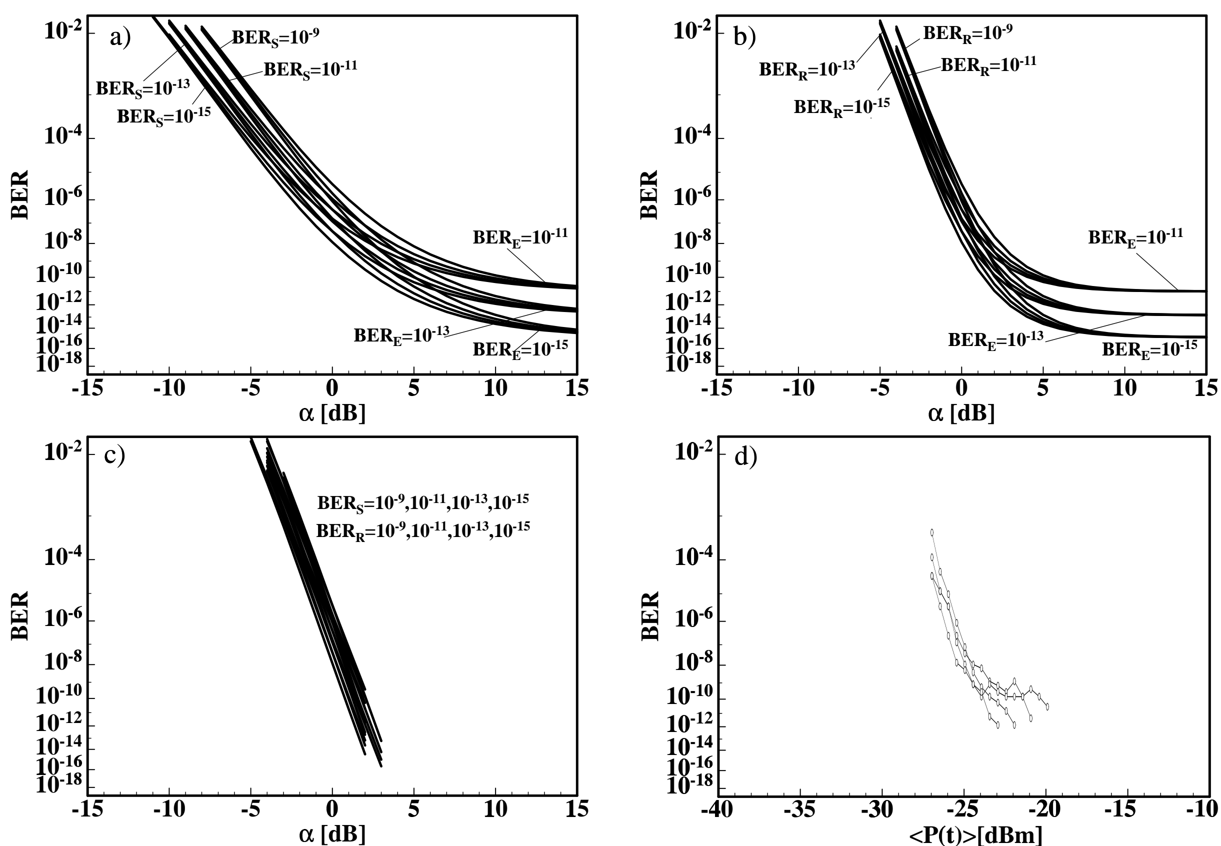

Fig. 4. Dependence of the BER on the received light intensity: a) to c) simulation of different weighting (reference $\alpha = 0$ dB) of receiver noise (R), shot noise (S) and excess noise (E); d) measurement.

statistics of shot noise and excess noise depend on the averaged received optical power, i.e. on the optical attenuation factor α. Linear filters may describe bandwidth limits, relaxation oscillations and the turn-on delay of the laser.

References

[1] J. G. Proakis, *Digital Communications*, 3rd Edition. McGraw-Hill International Editions, 1995.

[2] H. A. Haus, *Waves and Fields in Optoelectronics*. Prentice-Hall, 1984.

[3] K. Petermann, *Laser Diode Modulation and Noise*. Kluwer Academics Publishers, 1988.

[4] G. K. Grau, *Optische Nachrichtentechnik*, 3rd Edition, Ch. 6.3.8. Springer Verlag, 1991.

[5] G. K. Grau, *Quantenelektronik*. Vieweg Verlag, 1978.

Microcavity Light Emitting Diodes

Wolfgang Schmid

In this article the concept of microcavity LEDs (MCLEDs) is presented. The structure is varied and important properties are calculated. The limitations of such LEDs are shown.

1. Introduction

The efficiency of conventional LEDs is strongly limited because of total internal reflection. Placing the active material inside a microcavity, some properties of the spontaneous emission can be changed like spontaneous emission lifetime [1], spectral purity, and far field pattern [2]. To enlarge the external quantum efficiency one has to support emission perpendicular to the surface of the semiconductor at the cost of in-plane emission. This can be achieved by embedding the active material between two distributed Bragg reflectors (DBRs) leading to a structure similar to VCSELs. Nevertheless, there is a difference in the number of mirrorpairs. Laser emission relies on a self-consistent reproduction of a wave after one round-trip in the cavity requiring very high reflectivities, whereas in MCLEDs one has to limit the re-absorption, thus allowing only a moderate reflectivity of the output mirror [2]. To find a suitable structure we have evaluated the properties of such LEDs.

2. Theory

Spontaneous emission cannot be taken as a fixed parameter of a material but is depending on the surrounding structure. A cavity has a considerable influence on the spatial intensity of a standing wave, where nodes and antinodes develop. When placing an active material in such a node no emission is possible leading to inhibition of the spontaneous emission process in contrast to an antinode where enhancement occurs. In a specific structure there exists a great set of modes of which some will be supported while others are suppressed.

To predict the behavior of the emission, the spontaneous emission can be described by Hertzian dipoles located in the active layer and one has to calculate the coupling of these dipoles to all directions. Applying the reciprocity theorem, this is proportional to the coupling of incident plane waves to the dipoles which is much easier to compute using the transfer matrix method [3]. Considering all modes, this has to be done for TE- and TM-waves at a certain wavelength and for each direction both on the top and on the substrate side. In the next step the integration of the far field over a given emission spectrum is performed. The far field pattern of the upper hemisphere leads to the top emitted power and the overall far field yields the total power, finally giving the external efficiency as the ratio of both values. In these calculations the change of the spontaneous emission lifetime is neglected, being justified both by computed and reported variations in the range of 10 % [4].

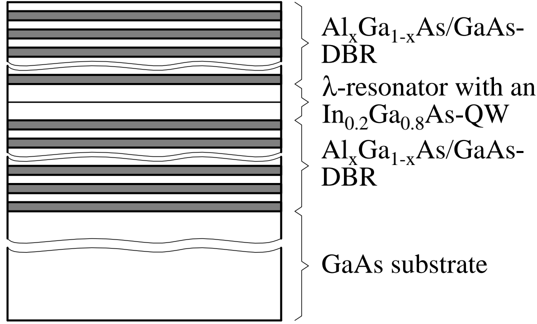

Fig. 1. The structure of the MCLED. An active layer is embedded in a λ-resonator between two DBRs with the number of top and bottom mirror pairs m_t and m_b, respectively.

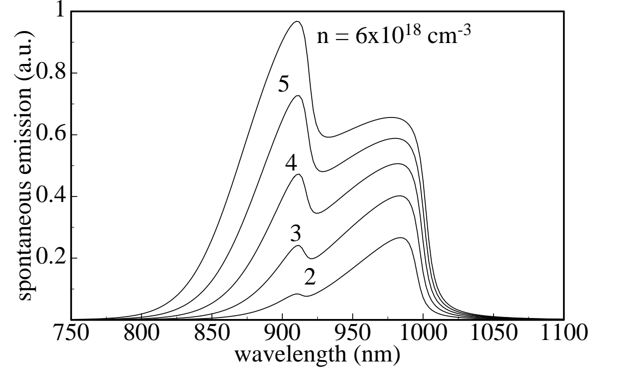

Fig. 2. The spontaneous emission spectra of an $In_{0.2}Ga_{0.8}As/GaAs$-quantum well for different carrier densities.

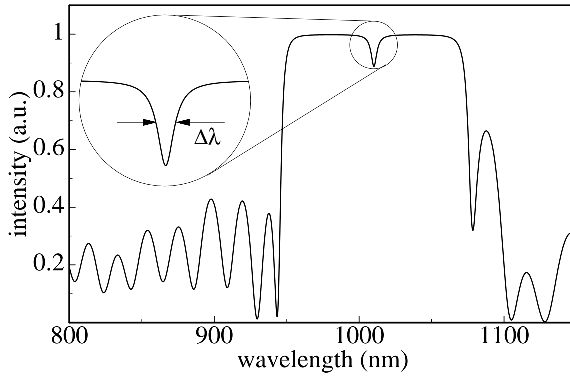

Fig. 3. The reflectivity spectrum of a typical MCLED.

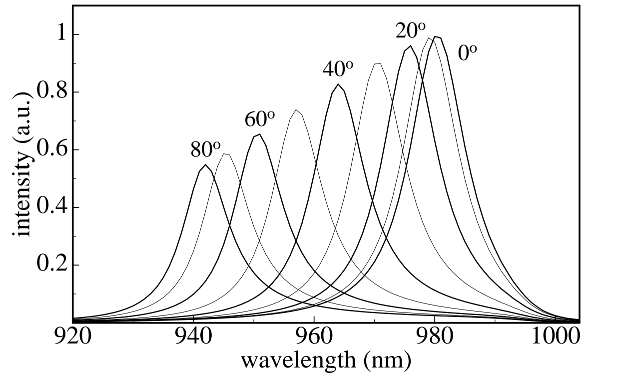

Fig. 4. The emission spectra versus the direction of observation.

3. Structure of the MCLED and Spontaneous Emission Spectra

Fig. 1 shows the assumed multi-layer structure for the calculations. An active layer is embedded between two DBRs with the number of periods m_b and m_t. The DBRs consist of GaAs and AlGaAs for the higher and lower refractive index layers, respectively. We take no lateral variations into account which largely facilitates the calculations. For the active material we assume an 8 nm $In_{0.2}Ga_{0.8}As$-QW with spontaneous emission spectra depicted in Fig. 2 [Ph.D.-3]. Obvious is the broadening of the spontaneous emission spectra with increasing carrier density. For high densities a peak at shorter wavelength occurs related to transitions between the second subbands.

4. Emission Spectra of a MCLED

In a conventional LED at 980 nm emission wavelength the spectral width with a typical value of 40 nm is strongly dependent on the temperature, whereas in MCLEDs the spectrum in Fig. 3 is mainly defined by the DBRs. Calculating the reflectivity spectrum, a cavity resonance is

obtained similar as in VCSELs. While in the latter case the resonance only fixes the emission wavelength, in MCLEDs both wavelength and spectral width are determined as indicated in Fig. 3. Also should be noted the dependence of the reflectivity and therefore the emission spectrum on the direction of observation. This is shown in fig. 4 where for increasing far field angle both the wavelength and the linewidth decrease.

5. External Efficiencies

The improvement of the external efficiency is one of the most essential reasons for research into the MCLEDs. Therefore we calculate this quantity, varying different parameters. First we assume only one DBR between the active layer and the substrate. The microcavity is then built by the DBR and the interface of GaAs to air. Fig. 5 shows the rising of η_{ex} before saturating at about 19% with increasing periods of AlAs/GaAs-layers for a fictitious monochromatic emission. The maximum external efficiency decreases with increasing carrier density due to off-resonance emission. High efficiency operation of an MCLED can therefore be expected only for low current densities. This is also seen when plotting the dependence of efficiency on wavelength in Fig. 6. For maximum efficiency, the DBR layers have to exceed $\lambda/(4\bar{n})$ by a few percent leading to resonance no more perpendicular to the surface but with a small in-plane k vector. The great disadvantage of enlarging resonant waves is the broadening of the far field.

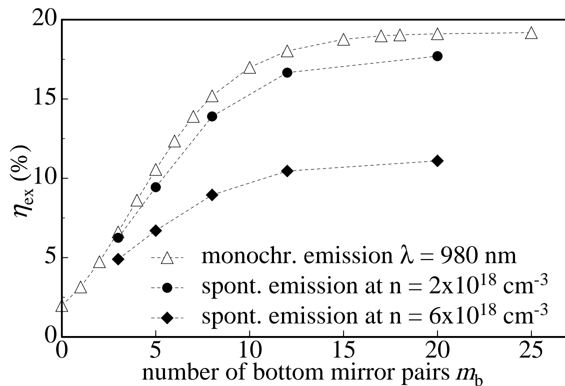

Fig. 5. External efficiency η_{ex} versus the number of periods of the bottom mirror m_b. Broad emission spectra lower the efficiency.

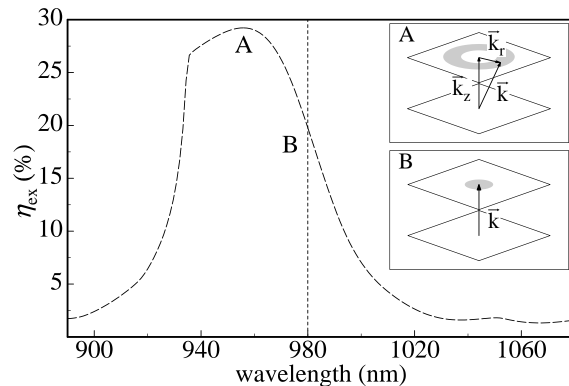

Fig. 6. External efficiency η_{ex} versus wavelength for monochromatic emission. The design wavelength is 980 nm and $m_b = 25$. The insets illustrate the broader range of useful wavevectors for small detuning of DBR and emission.

Another parameter of investigation is the high and low refractive index difference $\Delta\bar{n}$ of the two quarter wavelength stacks. A higher $\Delta\bar{n}$ diminishes the penetration depth and therefore reduces the angle dependence of the complex reflection coefficients. As illustrated in Fig. 7, lowering the refractive index leads to higher external efficiencies for monochromatic emission up to nearly 26 %. Disregarding the problem of current injection, a suitable material is Al_xO_y emerging from selectively oxidized AlAs layers. Nevertheless, for further diminution η_{ex} decreases again because of the improved lateral waveguiding property of the λ-resonator.

Fig. 8 displays the efficiency of the MCLED when adding a top DBR with varying numbers of mirror pairs. With a DBR matching the emission wavelength no higher output power can be

achieved. Nevertheless, as seen above for a small detuning a slight improvement can be obtained when the number of top mirrors m_t is in the range of 4.

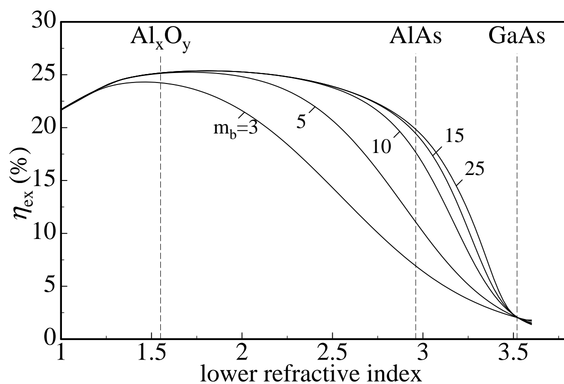

Fig. 7. External efficiency η_{ex} versus the lower refractive index. The refractive indexes of some interesting materials are also depicted.

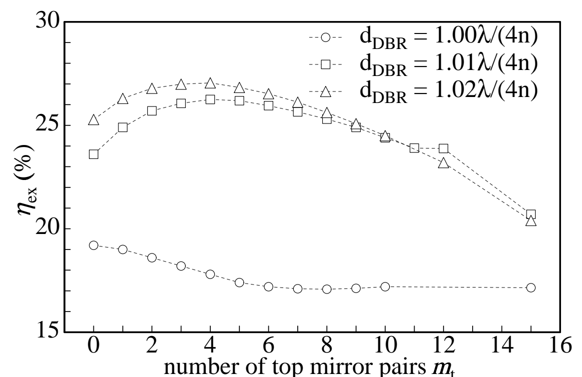

Fig. 8. External efficiency η_{ex} versus the number of periods of the top mirror m_t while $m_b = 20$. For improving of the efficiency a small cavity detuning is necessary.

6. Summary

We have theoretically shown the efficiency improvement to be obtained by embedding an LED in a microcavity. Nevertheless there are some restrictions. Because of the negligible reduction of spontaneous lifetime, the maximum modulation frequency is not higher than in a usual LED. A high efficiency demands low carrier density leading to small output power. In addition, requirements on accuracy of layer thicknesses are more stringent than in VCSELs where the wavelength of stimulated emission is pinned by the DBRs. Enlarging the efficiency by detuning the DBRs leads to far field broadening which is not desired with regard to efficient fiber coupling.

These theoretical results are in accordance with reports on fabricated MCLEDs in which the backside DBR is replaced by a metal reflector [5, 6]. In spite of the nearly wavelength independent reflection properties, the structures suffer from broad far-field patterns and require small current densities.

References

[1] H. Yokoyama, K. Nishi, T. Anan, and H. Yamada, “Enhanced spontaneous emission from GaAs quantum wells in monolithic microcavities”, *Appl. Phys. Lett.*, vol. 57, pp. 2814–2816, 1990.

[2] E. F. Schubert, N. E. J. Hunt, R. J. Malik, M. Micovic, and D. L. Miller, “Temperature and modulation characteristics of resonant-cavity light-emitting diodes”, *IEEE J. Lightwave Technol.*, vol. 14, pp. 1721–1729, 1996.

[3] P. Yeh, *Optical waves in layered media*. New York: J. Wiley & Sons, 1988.

[4] N. E. J. Hunt, E. F. Schubert, R. F. Kopf, D. L. Sivco, A. Y. Cho, and G. J. Zydzik, "Increased fiber communications bandwidth from a resonant cavity light emitting diode emitting at $\lambda = 940\,\text{nm}$", *Appl. Phys. Lett.*, vol. 63, pp. 2600–2602, 1993.

[5] J. Blondelle, H. De Neve, P. Van Daele, G. Borghs, and R. Baets, "16% external quantum efficiency from planar microcavity LEDs at 940 nm by precise matching of cavity wavelength", *Electron. Lett.*, vol. 31, pp. 1286–1288, 1995.

[6] H. De Neve, J. Blondelle, R. Baets, P. Demeester, P. Van Daele, and G. Borghs, "High efficiency planar microcavity LEDs: Comparison of design and experiment", *IEEE Photon. Technol. Lett.*, vol. 7, pp. 287–289, 1995.

Thermal Analysis in High-Power Semiconductor Laser Amplifiers

Zheng Dai

The thermal lensing effect within the large-area amplifier is investigated intensively. The device-dependent thermal response function is solved with the finite elemente analysis. Heat sources within the amplifier are analyzed and calculated with an improved electric and BPM model. The thermally induced index changes of broad-area amplifiers and tapered amplifiers under cw operation are simulated numerically.

1. Introduction

Thermal behavior plays a decisive role in cw high-power semiconductor lasers and laser amplifiers. Leakage current, non radiation recombination, gain coefficient, α-factor, carrier transportation, field confinement factor, and many other material properties are temperature dependent. Thermal rollover limits the maximum optical output power as well as the output beam quality. Even if far below the rollover temperature, the beam quality of an amplifier is also strongly depended on the temperature inhomogeneity within the waveguide. To investigate the thermally induced index change in detail, we integrate the finite element model into our BPM model [P-3] to simulate the cw operation of broad-area and tapered amplifiers. This article focusses on the beam quality and the thermally induced index disturbations. The devices are supposed to operate far below the rollover temperature.

2. Modeling

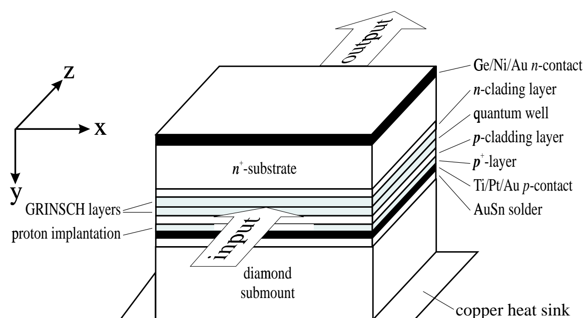

Fig. 1. Schematic structure of a semiconductor laser amplifier. Injected current is laterally confined by proton implantation. The amplifier is junction-down mounted on a diamond heat spreader for thermal dissipation.

As shown in Fig. 1 the amplified beam is collimated after the injected light transmits through the active area. The amplifier is junction-side-down mounted on a diamond heat spreader and the spreader is bonded on an 1-mm-wide, 5-mm-thick, and 2.2-mm-long copper heat sink, whose bottom temperature is kept at 300 K by water cooling. The thermal lensing effect is due to the thermally induced index changes, which is linearly proportional to the temperature rise in the

waveguide [1]. The temperature distribution across the waveguide $T(x,z)$ can be expressed as the convolution of a thermal response function $R_{th}(x)$ and the heat generation rate $H_{th}(x,z)$ [2]

$$T(x,z) = R_{th}(x) \otimes H(x,z) \quad , \tag{1}$$

where the thermal response function $R_{th}(x)$ is a device-dependent function. Its peak value and shape depend on the thermal structure of the amplifier and is pre-calculated for individual design with finite element method [P-3]. The thermal response function of the amplifier used in our laboratory is plotted in Fig. 2 for an 1-μm "point" heat source.

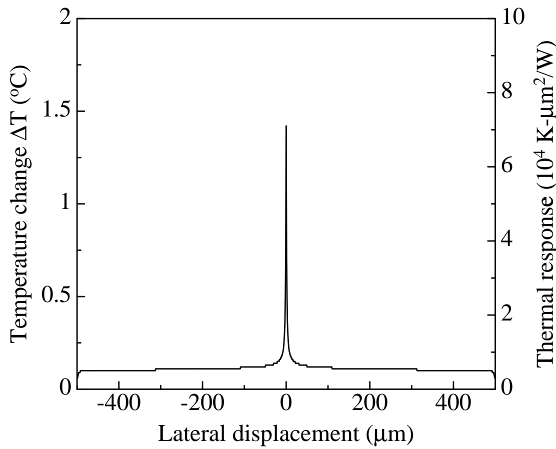

Fig. 2. The temperature response of 1-μm point source with a heat generation rate of $2.0 \cdot 10^7\,\mathrm{W/m^2}$. The thermal response function is plotted on the right axis in $\mathrm{K \cdot \mu m^2/W}$.

Heat generated outside the GRINSCH layer is negligible for high quality InGaAs/AlGaAs/GaAs laser devices. The heat sources concentrated in the GRINSCH region are further classified as electric injection $Q_{el}(x,z)$ in the carrier confinement layer d_c, optical absorption $Q_{abs}(x,z)$ in the optical confinement layer w_c, and photon cooling Q_{sti} due to the stimulated emission in the active layer d_a. It is inconvenient to mesh the calculation area according to the sort of the heat sources, especially for the thin quantum-well active layer. Considering the thermal diffusion length is in the order of $10\,\mu$m, much larger than perpendicular dimension of the heat sources, we convert the above heat sources into an equivalent face heat source $H(x,z)$ in the middle of the GRINSCH region. The heat generated per unit active area is expressed as

$$\begin{aligned} H(x,z) &= Q_{el} \cdot d_c + Q_{abs} \cdot w_c + Q_{sti} \cdot d_a \\ &= J(x,z)V_{jct}(x,z) + \alpha_{abs} S(x,z) w_c + g S(x,z) d_a \quad , \end{aligned} \tag{2}$$

where $J(x,z)$ is the injected current density, $V_{jct}(x,z)$ is the junction voltage, α_{abs} is the absorption coefficient, g is the modal gain for laser amplification, and $S(x,z)$ is the optical power density in $\mathrm{W/m^2}$.

3. Numerical Results

The above thermal model is integrated into each step of BPM. The electric model describing the current confinement and the BPM model describing the beam amplification and propagation have been introduced in [P-3]. Parameters extracted from experiments and literature are the same as those used in [P-3, P-59].

A) Broad-Area Amplifier

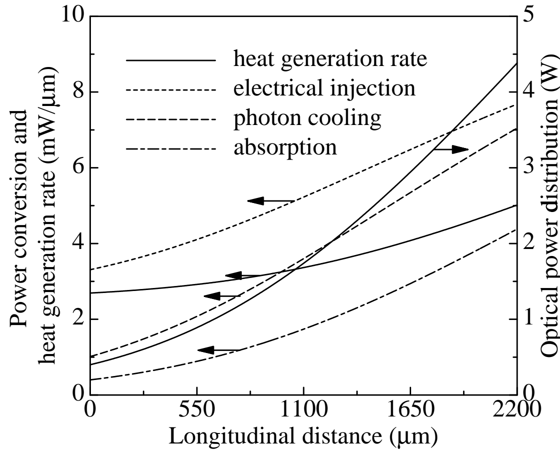

Fig. 3. The longitudinal power conversion between electric injection, laser amplification, optical absorption and photon cooling. Operation condition: injected current $I = 8.8\,\mathrm{A}$, optical input $P_{in} = 400\,\mathrm{mW}$, output power $P_{out} = 4.4\,\mathrm{W}$.

The heat source inside the amplifier is neither uniform in lateral nor in longitudinal direction. The longitudinal power conversion calculated according to expression (2) of a 400-μm-wide, 2200-μm-long amplifier is shown in Fig. 3. The amplifier is driven at 8.8 A and has an output power of 4.4 W. The optical power increases nearly exponentially in longitudinal direction and the curve of the optical absorption is proportional to the amplified optical power. High optical power intensifies the hole burning effect in gain coefficient and in carrier concentration, which cause a decrease in the junction voltage. The decline in junction voltage raises the injected current density significantly, as a consequence, the total injected electrical power density increases along the transmission path. Photon cooling depends on the transmitted optical power and saturated gain coefficient. The low optical injection will minimize the photon cooling at the input side and the extremely high optical power saturates the gain coefficient and reduces the photon cooling

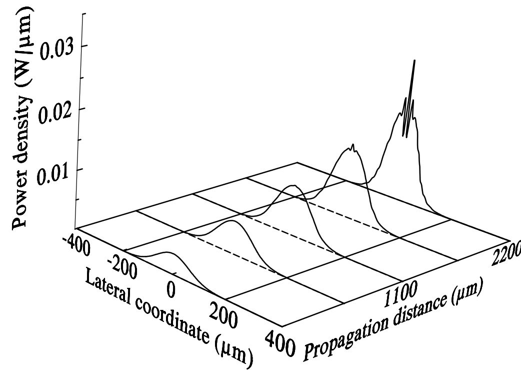

Fig. 4. Beam profile within a $400\,\mu\mathrm{m} \times 2200\,\mu\mathrm{m}$ broad-area amplifier under cw operation. Driving current $I = 5.0\,\mathrm{A}$, optical input $P_{in} = 400\,\mathrm{mW}$, optical output $P_{out} = 1.58\,\mathrm{W}$, thermal index coefficient $\alpha_{th} = 3.4{\cdot}10^{-4}\,\mathrm{K}^{-1}$.

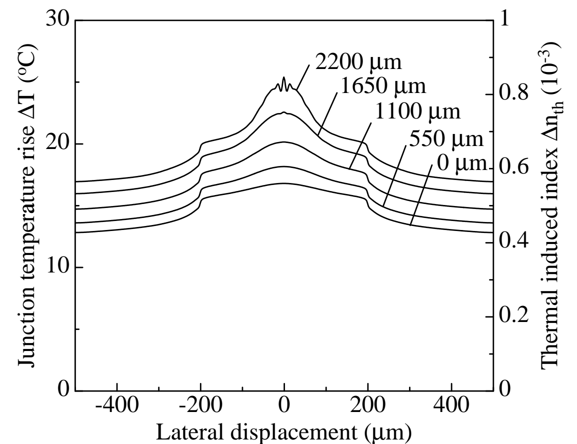

Fig. 5. Temperature rise and the thermally induced index change at different propagation position of the broad-area amplifier. Operation conditions are the same as in Fig. 4.

effect at the output side. A gaussian beam of 400 mW is used as the injected beam in Fig. 3. Comparing the injected electric power density and the heat generation rate, we find a significant contribution of the photon recycling.

The thermal lensing effect is due to the lateral inhomogeneity of the temperature distribution. With the same device parameters used above, the thermal lensing effect occurs when the driving current increases to 5.0 A. Fig. 4 shows the beam profile within the amplifier as the thermal lensing effect occurs. The deeper hole burning in the center of the waveguide increases the heat generation rate there. Furthermore, the photon recycling makes some additional contribution to the heat generation rate at the center of the waveguide. The lateral intensity fluctuations cause corresponding variations in the heat sources and lead to modulations in the temperature distribution and the thermally induced index. The temperature and corresponding index profiles at different propagation positions are plotted in Fig. 5.

B) Tapered Amplifier

The tapered amplifier represents the state-of-the-art power amplifier and has the unique advantage of monolithical integration. With the model described above, we also simulated the thermal lensing effects in tapered amplifiers. The amplifier is 5-μm wide at the input side, 250-μm wide at the output side, and 2000-μm in length.

The beam profiles within the tapered amplifier are shown in Fig. 6. A gaussian beam of 10 mW is injected into the narrow waveguide of the amplifier. The amplifier is driven under 3.4 A and has an optical output power of 1.2 W. The temperature changes and the thermally induced index changes at different propagation positions are plotted in Fig. 7. Due to the effect of the photon recycling, an "inverted" temperature distribution is generated near the input facet of the amplifier, which builds up a negative thermal lens at the input side of the waveguide compensating the self focussing effect. The beam quality strongly depends on the heat dissipation

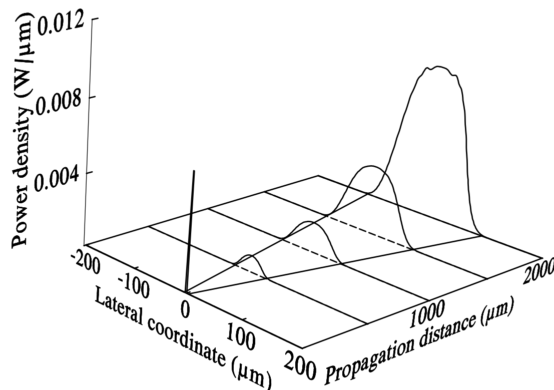

Fig. 6. Beam profile within the tapered amplifier under cw operation. Driving current $I = 3.4\,\mathrm{A}$, injected optical power $P_{in} = 10\,\mathrm{mW}$, optical output $P_{out} = 1.2\,\mathrm{W}$, thermal index coefficient $\alpha_{th} = 3.4{\cdot}10^{-4}\,\mathrm{K}^{-1}$.

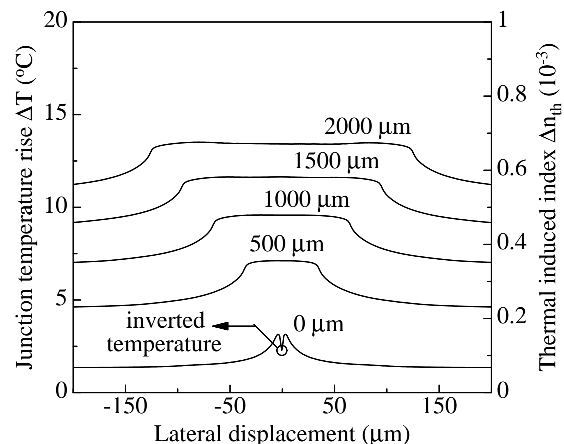

Fig. 7. Temperature rise and the thermally induced index change at different propagation position of the tapered amplifier. Operation condition is the same as in Fig. 6.

and the heat generation rate in the amplifier. The thermal lensing effect limites the maximum diffractive-limited output power.

4. Conclusions

A thermal model for broad-area and tapered amplifiers has been developed using the finite element and the BPM model. Non uniform heat sources have been analyzed for amplifiers under cw operation. The experimentally observed inverted temperature distribution has been investigated numerically.

References

[1] H. C. Casey, Jr. and M. B. Panish, "Optical field and wave propagation", Chapter 2 in *Heterostructure Lasers, Part A: Fundamental Principles*. New York: Academic Press, Inc., 1978.

[2] R. J. Long, A. Hardy, R. Park, D. Mehuys, S. O'Brien, J. Major, and D. Welch, "Numerical analysis of flared semiconductor laser amplifiers", *IEEE J. Quantum Electron.*, vol. 29, pp. 2044–2051, 1993.

High-Power InGaAs/AlGaAs Traveling-Wave Amplifiers

Günter Jost

Broad-area traveling-wave semiconductor amplifiers (TWA) are capable of producing high-power near-diffraction-limited emission. Small sizes and large electrical to optical conversion efficiencies are required in a wide range of applications, including pump sources for Er-doped fiber amplifiers and solid-state lasers as well as satellite optical communication and biomedical uses. TWAs use the optical gain of a forward biased semiconductor diode that is based on the principle of stimulated emission in the population inverted laser medium. The graded-index separate-confinement heterostructure (GRIN-SCH) quantum-well structures are grown by molecular beam epitaxy (MBE) on n-doped GaAs substrates. The input and output facets have an antireflection (AR) coating made by evaporation or ion beam sputter deposition. To reduce thermal effects, the device can be mounted juntion-side-down on a heat spreader and copper heatsink. With such devices we achieve an output power of more then 2 W under CW condition and a spectral gain of 14 dB with a FWHM of 40 nm.

1. Introduction

We report about broad-area traveling-wave high-power amplifiers with an active region consisting of an 8 nm $In_{0.2}Ga_{0.8}As$ quantum well surrounded by 50 nm-thick GaAs spacing layers. The waveguiding region consists of $Al_xGa_{1-x}As$ cladding layers with a continuously varied Al concentration. The n- and p-type $Al_{0.47}Ga_{0.53}As$ cladding layers have a thickness of 1 μm. To get broad-area traveling-wave amplifiers it is necessary to have an antireflection coating on the cleaved input and output facet of the amplifiers. We use an SiO_x single-layer coating, where the refractive index can be controlled by the deposition rate and oxygen or nitrogen partial pressure in the deposition system. The output power of a reference laser is measured during the evaporation to control the thickness of the AR coating. The lowest facet reflectivity at gain-peak wavelength can be reached by stopping the deposition at the minimum of the output power. Especially for the evaporation system, it is difficult to control the refractive index in a tolerance of 0.01 and achieve reproduceable results [1]. We get the best results with an ion-beam sputter deposition. The obtained residual reflectivity of the AR coating is in the range of $5 \cdot 10^{-4}$. This is necessary for small undulation in the optical spectrum and high gain over a large spectral range. 100-μm- and 150-μm-wide broad-area laser amplifiers with cavity lengths between 1 mm and 1.5 mm have been fabricated [2]. Some of the devices have been mounted junction-side down on copper heatsinks with a heat spreader to get a low thermal resistance as described on pages 69–74. This is necessary for high-power traveling-wave amplifiers to prevent thermal roll-over of the output power and therefore a decrease of wall-plug efficiency. The devices have been characterized with regard to the optical output power, spectral gain, emission spectra, and beam quality.

2. Characterization of broad-area amplifier

As master oscillator we use a Ti:sapphire laser with a gaussian beam profil. The wavelength of this laser ranges continuously from 920 nm to 1060 nm. To achieve an appropriate input beam profil, the gaussian beam is expanded with a beam expander to approximately 4 mm FWHM. A combination of a cylindrical lens and a focusing lens is used in horizontal direction as an afocal telescope. To inject a broad, gaussian shaped beam with nearly planar phase front into the active zone of the amplifier, typical cylindrical lenses with focal lengths between 6 cm and 30 cm are used, depending on the amplifier aperture. As focusing lens serves in vertical direction a lens with a numerical aperture of 0.615 and a focal length of 6.5 mm. By operating the amplifier in a reverse-biased photoconductive mode and measuring the responsivity, the coupling efficiency between Ti:sapphire laser and traveling-wave amplifier is found to be in the range of $\eta = 65\,\%$ [3]. Fig. 1 shows the light-current characteristic of a 150- μm-broad traveling-wave amplifier with

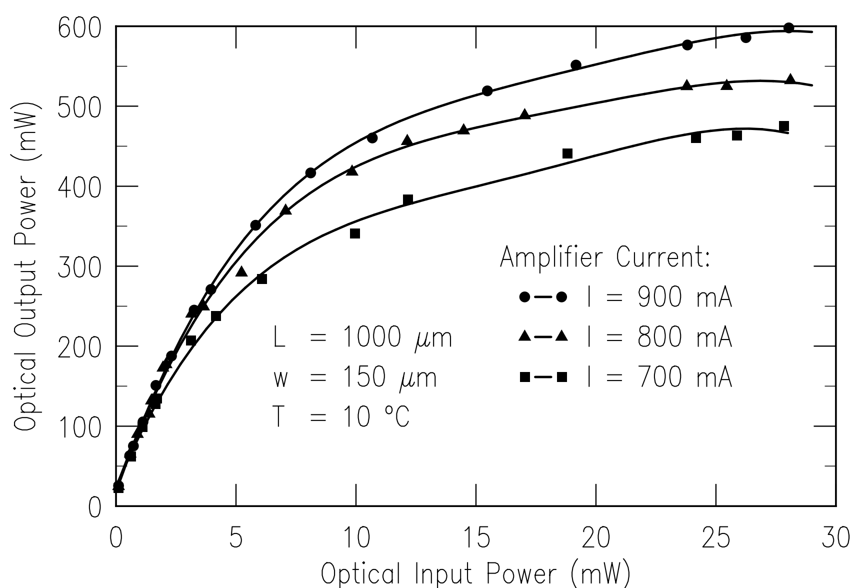

Fig. 1. Optical output power versus input power for different current under CW conditions at a temperature of 10 °C. The 150-μm-broad traveling-wave amplifier with a cavity length of 1 mm is mounted junction-side up

a cavity length of 1 mm under CW condition at a temperature of 10 °C. This device is mounted junction-side up. The maximum output power is 600 mW for an input power of 27 mW at a current of 900 mA. The output power of this device is limited by the thermal effects caused by the large thermal resistance of this junction-side up mounted device. Fig. 2 demonstrates the behavior of a 150-μm-broad amplifier with a cavity length of 1.5 mm. With such a junction-side down mounted amplifier we achieve an maximum output power of 2 W for an input power of 350 mW at a CW current of 3.4 A and a heatsink temperature of 0 °C. The maximum wall-plug efficiency of this device is 32 % depending on the input power and current of the broad-area amplifier. If we increase the current of the device, we also have to increase the input power to saturate the amplifier and to get a maximum of wall-plug efficiency. In that way we reduce the spontaneous and amplified spontaneous emission and improve the amplifier noise characteristic.

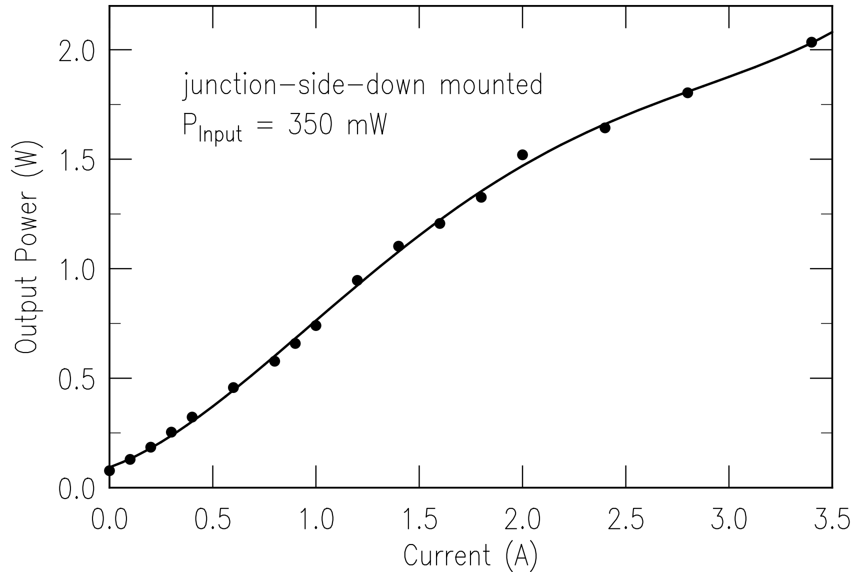

Fig. 2. Optical output power versus current under CW conditions at a temperature of 0 °C. The 150-μm-broad traveling-wave amplifier with a cavity length of 1 mm is mounted junction-side down on a boron nitride heatspreader.

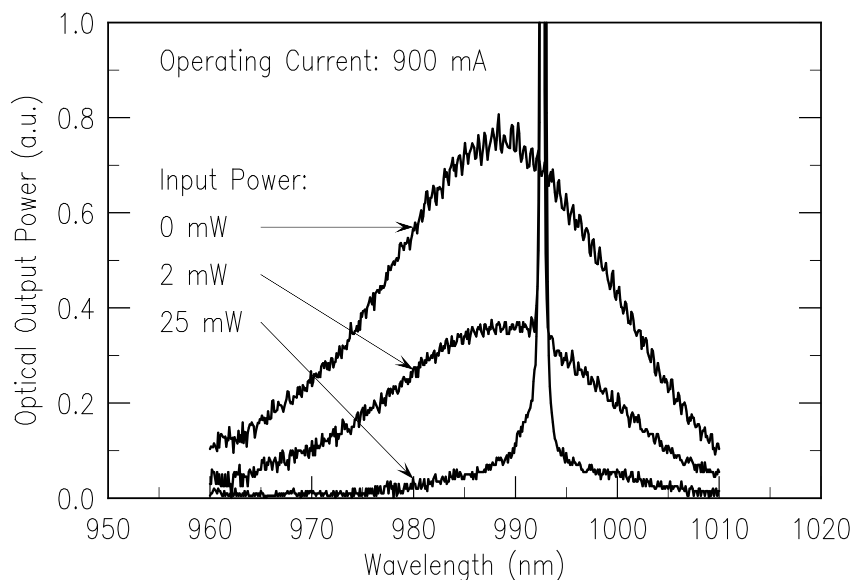

Fig. 3. Optical spectrum of a broad-area amplifier at constant current for three different input power levels. The input wavelength of the Ti:sapphire master oscillator is 992 nm.

This behaviour is shown in the emission spectra (Fig. 3) at an operating current of 900 mA for three different values of input power. The input wavelength is at 992 nm represented by the cutted peak in the optical spectrum. The spectral gain of a broad-area amplifier versus different input wavelength is plotted in Fig. 4 for 21 mW input power at 900 mA. The full width at half maximum is about 42 nm, the maximum spectral gain is 14 dB at 992 nm.

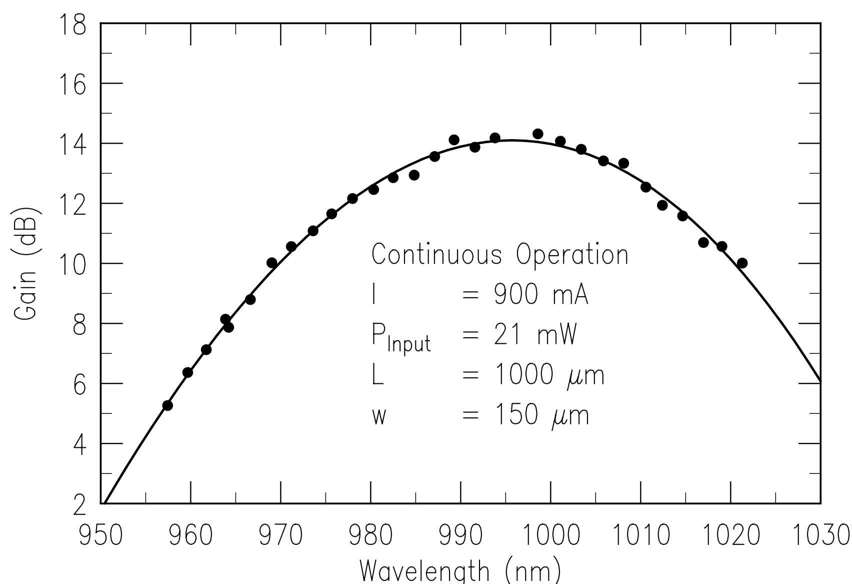

Fig. 4. Spectral gain of broad-area amplifier. The maximum gain of 14dB is achieved at a wavelength of λ= 992 nm. The FWHM is 42 nm.

3. Beam quality

With an oscillator/amplifier system it is possible to get high output power and near diffraction limited beam quality. In order to achieve high coupling efficiencies for single mode fiber applications, a beam quality M^2 of nearly 1 is necessary. Tab. 1 shows the beam quality factor M^2 [4] for different semiconductor laser devices.

device	input power	beam quality
broad-area laser	—	$M^2 > 35$
amplifier without input power (900 mA)	—	$M^2 > 150$
amplifier with input power (900 mA)	22 mW	$M^2 = 6.5$

Tab. 1. Beam quality of broad-area laser and amplifier.

For broad-area laser of the same size as our amplifier structures we measured a beam quality factor M^2 of more then 35 corresponding to a spatially coherent but filamented mode. Without input power the beam quality factor M^2 of the amplifier is about 150. The lateral amplified emission can be viewed as consisting of many transverse modes with very limited spatial coherence. If we increase the input power up to 22 mW at an amplifier current of 900 mA, we achieve a beam quality M^2 of about 6.5 for an output power of 570 mW. Further improvements of the

antireflection coating and amplifier with tapered geometry would optimize the beam quality factor, close to the near-diffraction-limited output profile of $M^2 = 1.7$ of the Ti:sapphire master oscillator.

References

[1] Y. Yamamoto, *Coherence, Amplification and Quantum Effects in Semiconductorlasers*, pp. 260–267. New York: Wiley Interscience Publication, 1996.

[2] G. Jost, J. Heerlein, and S. Morgott, “Characterization of high-power lasers and traveling-wave amplifiers”, *Annual Report 1995, Department of Optoelectronics, University of Ulm*, pp. 46–50, 1996.

[3] L. Goldberg, D. Mehuys, M.R. Surette, and D. C. Hall, “High power, near-diffraction-limited large-area traveling-wave semiconductor amplifiers”, *IEEE J. Quantum Electron.*, vol. 29, pp. 2028–2043, June 1993.

[4] A. E. Siegman, *Solid State Lasers: New Developments and Applications*. New York: Plenum Press, 1993.

Fabrication and Mounting of Broad-Area Laser Diodes for High-Power Operation

Jörg Heerlein

We report on the fabrication technology, mounting and characteristics of high-power InGaAs/AlGaAs broad-area GRINSCH lasers. For efficient cooling we mounted the semiconductor lasers on diamond, boron nitride and copper compound heat spreaders with an eutectic AuSn solder. We achieved an output power of 1.5 W with a maximum wall-plug efficiency of 56 % for uncoated devices.

1. Introduction

High power semiconductor lasers emitting at a wavelength of around $\lambda = 980$ nm are used in a wide range of applications: for pumping of erbium-doped fiber amplifiers, for pumping of solid state lasers and for direct material treatment. Furthermore, by evaporating an anti-reflection coating on the facets, the devices can be used as travelling-wave amplifiers [1]. The maximum output power of InGaAs/AlGaAs lasers is limited by two events. The first is an irreversible catastrophic optical mirror damage (COMD). Filamentations in broad area lasers and a degradation of the facets by oxidation are the leading reasons for the destruction of the laser facet. Special geometrical and epitaxial structures with little or without aluminum in the cladding layer and dielectric mirror coatings are used for increasing the COMD limit [2]. The second power limitation is a reversible thermal roll over due to the thermal power dissipation which decreases the optical gain. To increase this power limitation, the differential series resistance of the laser has to be lowered, leading to a reduced thermal power dissipation. But of course there are non-radiative transitions and absorptions which can not be omitted completely. Therefore, an efficient cooling is necessary [3]. Since the thermal conductivity of the GaAs substrate is low (44 W/mK) it is recommendable to mount the laser diode junction-side down. A lot of soldering materials are commonly used for bonding semiconductors on submounts, which are discussed later. Since the local heat is generated in a very small area, it is helpful to spread the heat onto a larger area for easier transportation. For that reason we bonded broad area lasers on heat spreaders with an excellent thermal conductivity.

2. Device Fabrication

We have fabricated MBE-grown strained InGaAs/AlGaAs/GaAs graded-index separate-confinement heterostructure (GRINSCH) lasers with different numbers of quantum wells (1–2). The 8-nm-thick $In_{0.2}Ga_{0.8}As$ quantum wells are surrounded by 40-nm-thick GaAs barrier layers and $Al_xGa_{1-x}As$ graded index layers where the Al mole fraction x is linearly graded from 14 % to 50 %. We have varied the thickness of the GRINSCH region in the range of 250 nm to 600 nm. The p- and n-type dopands are Be and Si, respectively. The top contact consists of a highly doped

($2 \cdot 10^{20}\,\mathrm{cm}^{-3}$) cap layer and an evaporated TiPtAu contact metallization. The lateral active area with a width of 20–150 μm has been defined by wet chemical etching. The structures have been passivated by a 200-nm-thick Si_3N_4 layer deposited by plasma-enhanced chemical vapor deposition (PECVD). For easier cleaving the wafer has been thinned from the substrate side to about 100 μm and a n-contact has been evaporated. Fig. 1 shows the MBE-grown epitaxial structure. Laser devices were completed by scribing with a mechanical precise diamond scriber and cleaving of the Fabry-Perot resonators with definite length. So lasers with lengths of 300 μm up to 2 mm have been fabricated.

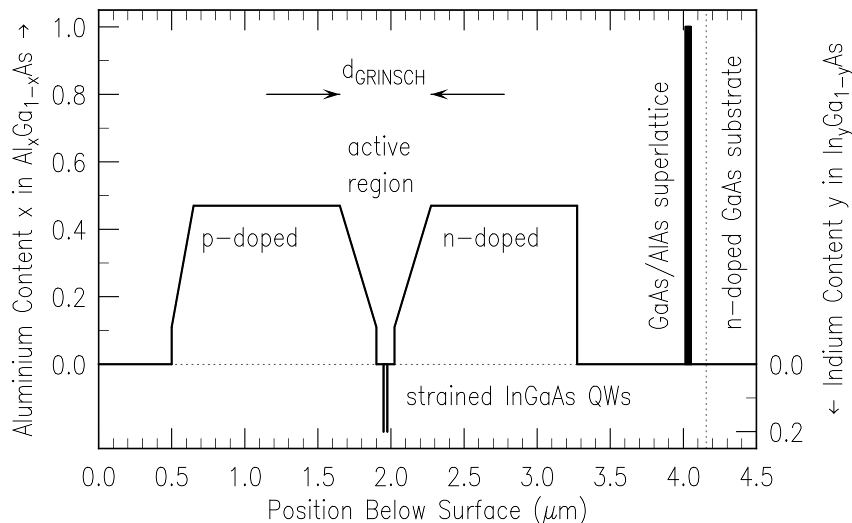

Fig. 1. MBE-grown laser structure.

3. Laser Bonding

Besides a low series resistance, an effective cooling mechanism is necessary. Without a reliable bonding the lasing performance is limited by a thermal roll over or would fail due to inadequate heat dissipation and mechanical strength. For lowering the thermal resistance, the laser diodes have been soldered junction-side down on heat spreaders like diamond, T-cBN (translucent cubic boron nitride) and $W_{0.89}Cu_{0.11}$ because of their good thermal conductivity. For reliable bonding, an adequate bonding medium is required. Commonly used materials are hard solders, soft solders and metal filled epoxies [4]. Metal filled epoxies have poor thermal conductivities of 1–2 W/mK and thus lead to high power dissipation. Furthermore, the epoxy has a bad homogeneity and a layer thickness which is difficult to reproduce. Most commonly used are soft solders like In, Pb or compounds. These media offer a good thermal conductivity like most of the metals but are mechanically weak. Lasers bonded with soft solders do not suffer under high stress since the bonding layer deforms plastically to compensate the developed stress. The stress occurs during the cooling process caused by the mismatch of the thermal expansion between semiconductor crystal and subcarrier material. But soft solders are suspected to cause migration and whiskers, to thermal fatigue and creep rapture due to the plastical deformation and oxidation which limits the long term reliability. In this work we used as a hard solder AuSn. The AuSn eutectic alloy has a melting point of 278 °C. AuSn has a good thermal conductivity and a high mechanical

material	thermal conductivity λ_{th} [$Wm^{-1}K^{-1}$]	thermal expansion coefficient α [$10^{-6}\,K^{-1}$]
CVD diamond	1000	2.3
T-cBN	600	3.7
copper	398	16.8
gold	312	14.3
tin	65	27
$W_{0.8}Cu_{0.2}$	200	8.3
$W_{0.89}Cu_{0.11}$	180	6.5
GaAs	44	6.4
single component epoxy	1.72	–
two component epoxy	1.64	–

Tab. 2. Thermal conductivities and thermal expansion coefficients for different heat spreader materials.

strength that results in a long term stable connection. Since there is no plastical deformation, the laser diode suffers under a large amount of stress depending on the bonding temperature and the mismatch of thermal expansion. As heat spreaders we use 300-μm-thick diamond, T-cBN or $W_{0.89}Cu_{0.11}$ metalized with TiPtAu layers. The 3-μm-thick AuSn solder on top consists of a few thin Au and Sn layers. Tab. 1 shows the thermal conductivities and the thermal expansion coefficients of GaAs and some heat spreader materials. As one can see, the CVD (chemical vapor deposition) diamond offers the highest thermal conductivity but the thermal expansion is quite different compared to the coefficient of the GaAs substrate. The $W_{0.89}Cu_{0.11}$ compound is fitted in thermal expansion, such that bonding becomes uncritical. But its thermal conductivity is much lower compared to the CVD diamond. T-cBN is an alternative with a lower mismatch in expansion compared to CVD diamond and offers a quite good thermal conductivity. While cooling down the laser during bonding an excessive thermo mechanical stress is produced in the case of large expansion mismatch. Fig. 2 shows the result on the laser facet of a laser bonded onto a CVD diamond heat spreader. Cracks in the facet occur and therefore the laser mirror is

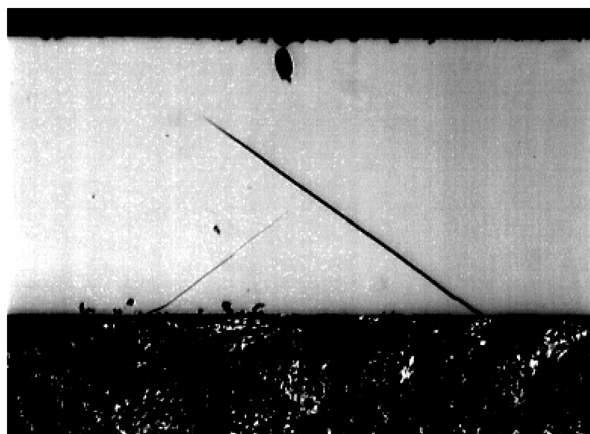

Fig. 2. Cracks on the laser facet due to different thermal expansion of CVD diamond and GaAs substrate.

destroyed.

The bonding process has been optimized and as a result we are able to bond the laser reproducible on a diamond heat sink up to a length of 2 mm. The lasers are bonded on the heat spreader with a die bonder. We use a pulse-heated graphite heater stripe. The device is heated up to a base temperature of 200 °C and then heated up to an end temperature of 290 °C in about 3 s. During bonding, N_2 is blown over the specimen. The diode is holded down onto the heat spreader with only little force. A further improvement is achieved by modifying the AuSn solder. For that, a 2-μm-thick electroplated Au layer has been deposited on the p contact of the laser. This modification was suggested by Weiß [3] and explained by producing a AuSn ζ-phase where the mechanical stress is reduced. Furthermore, the thick Au layer offers a nearly plastical connection. The time for cooling down the laser is also a critical parameter. We used a cooling ramp of about 10 K/min. These process parameters lead to the excellent laser characteristics presented in section 4. After gluing the heat spreader onto a commercial $W_{0.8}Cu_{0.2}$ submount, the laser is connected by some gold wires by using a wedge bonder. Fig. 3 shows a SEM photograph of an 1.5-mm-long laser diode bonded onto a CVD diamond heat spreader. The diamond itself is glued by a single component epoxy on a $W_{0.8}Cu_{0.2}$ submount. The electrical connection is provided by five gold wires.

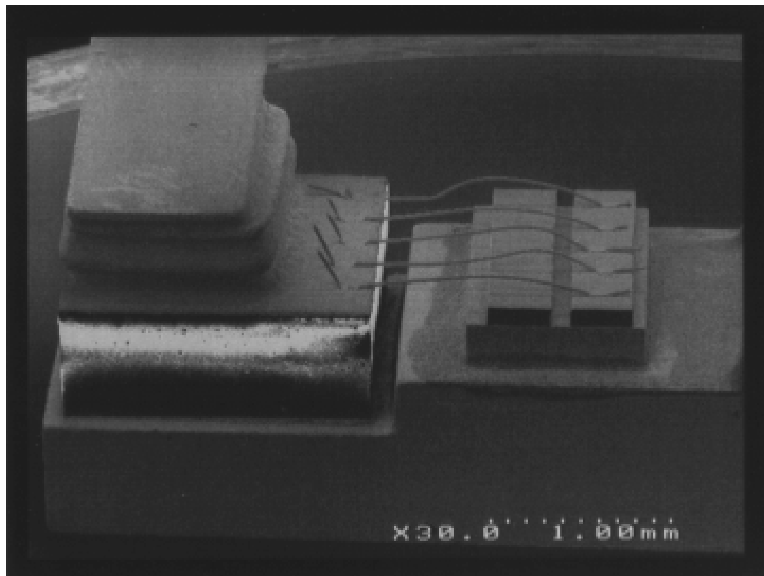

Fig. 3. SEM picture of a mounted laser diode with a cavity length of 1.5 mm.

4. Characterization

All measurements have been carried out in continuous wave (CW) operation. The lasing spectra show emission peak wavelengths in the range of 980–1000 nm. All lasers are measured as cleaved without facet coating. The broad area laser stripes exhibit threshold current densities of 80 to 220 A/cm^2. Internal efficiencies and intrinsic losses are 70–86 % and 5–12 cm^{-1}, respectively, depending on the epitaxial structure.

For measuring the thermal resistances of mounted laser diodes we use the correlation of wavelength shift and temperature rise. In theory, the wavelength shift of the band gap for an 8 nm $In_{0.2}Ga_{0.8}As$ quantum well is $\Delta\lambda/\Delta T = 0.32\,nm/K$ [Ph.D.-3]. We measured values between 0.3 nm/K and 0.35 nm/K since the wavelength does not increase linearly in broad area structures due to the fact that a lot of higher longitudinal and transversal modes propagate through the resonator (compare Fig. 4). Using

$$R_{th} = \frac{\Delta\lambda}{0.32\,\mathrm{nm/K}} \cdot \frac{1}{\Delta P_d} = \frac{\Delta T}{\Delta P_d} \tag{1}$$

with the power dissipation $P_d = VI - P_{opt}$ we have measured the thermal resistances R_{th} for broad area lasers with resonator lengths of 500 μm and widths of 100 μm. Lasers bonded on CVD diamond and T-cBN heat spreaders which are glued by a single component epoxy on the subcarriers show thermal resistances R_{th} of 39 K/W and 45 K/W, respectively. The fact, that the value of $R_{th} = 39\,K/W$ for a $500 \cdot 100\,\mu m^2$ large device is still high, can be explained by the low thermal conductivity of the epoxy below the diamond. An alternative is provided by the thermal compression bonding of the heat spreader onto the submount. This can be seen from the measurement of the thermal resistance of a laser diode soldered junction-side down on a $W_{0.89}\,Cu_{0.11}$ heat spreader, where the heat spreader is mounted onto the submount by thermal compression bonding. In this case, a thermal resistance of 31 K/W is observed. For comparison we glued a laser directly on a submount junction-side up, the thermal resistance increases to a value of 82 K/W as depicted in Fig. 5.

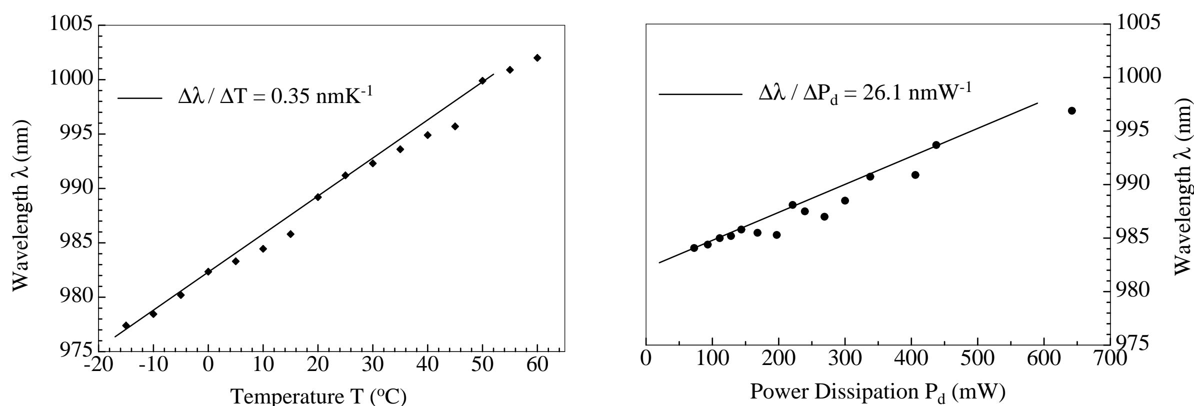

Fig. 4. Correlation between temperature and wavelength shift of the gain maximum.

Fig. 5. The diagram shows the wavelength shift due to increasing power dissipation of a laser glued junction-side up on a submount. From the slope of this characteristic the thermal resistance can be calculated to a value of 82 K/W.

The laser characteristic of a $500 \cdot 100\,\mu m^2$ large single-quantum-well laser bonded on CVD diamond heat spreader is presented in Fig. 6. This device has a threshold current density of 171 Acm^{-2} and a differential quantum efficiency of $\eta_d = 69.4\,\%$. The measured continuous optical power of 1.5 W with a wall-plug efficiency of $\eta_c = 56\,\%$ exhibits the high performance of the device.

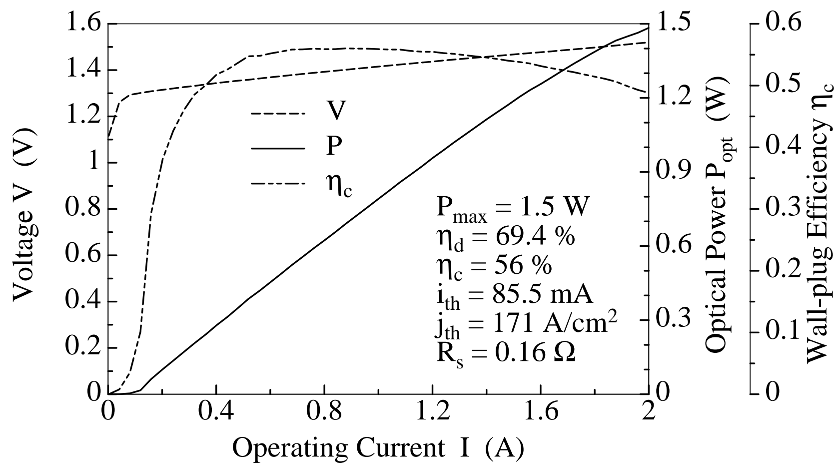

Fig. 6. Laser characteristic of a $500 \cdot 100\,\mu\text{m}^2$ SQW laser bonded on a diamond heat spreader.

References

[1] L. Goldberg, D. Mehuys, M. Surette, and D. Hall, "High power, near-diffraction-limited large-area traveling-wave semiconductor amplifier", *IEEE J. Quantum Electron.*, vol. 29, pp. 2028–2043, 1993.

[2] A. Moser, A. Oosenbrug, E. E. Latta, Th. Forster, and M. Gasser, "High-power operation of strained InGaAs/AlGaAs single quantum well lasers", *Appl. Phys. Lett.*, vol. 59, pp. 2642–2644, 1991.

[3] St. Weiß, E. Zakel, and H. Reichl, "Mounting of high power laser diodes on diamond heatsinks", *IEEE Trans. Components, Packaging, and Manufacturing Technol.*, vol. 19, pp. 46–53, 1996.

[4] C. C. Lee, C. Y. Wang, and G. S. Matijasevic, "A new bonding technology using gold and tin multilayer composite structures", *IEEE Trans. Components, Hybrids, and Manufacturing Technol.*, vol. 14, pp. 407–412, 1991.

GaN-Based Light Emitting Diodes Grown by Low Pressure MOVPE

Christoph Kirchner, Markus Kamp

Using low pressure Metal Organic Vapor Phase Epitaxy (MOVPE) for GaN growth and magnesium as p-type dopant, we have fabricated GaN based pn-junctions grown heteroepitaxially on c-plane sapphire. Visible light emission is obtained from GaN pn-homojunctions and InGaN heterojunctions. Results will be discussed.

1. Introduction

Recently, there has been great interest in short wavelength light-emitting devices fabricated from III-V Nitride compound semiconductors (InAlGaN) with emission wavelengths from the UV to red spectral region. Intensive research on III-V Nitrides has paved the way to high quality crystals of AlGaN, InGaN and p-type conduction [1, 2, 3, 4]. High-power blue and green LEDs using quantum well structures are now commercially available [5]. A blue emitting laser diode with a InGaN multi-quantum-well structure as active layer was demonstrated by S. Nakamura in late 1995 [6].

2. Experimental

A horizontal MOVPE reactor (AIXTRON AIX 200 RF) operated at low pressure (100–300 mbar) is used for growth. Substrate material is sapphire with (0001) orientation (c-plane). Triethylgallium (TEGa), Trimethylaluminium (TMAl), Trimethylindium(TMIn) and Ammonia (NH_3) are used as source materials. The dopant sources are Silane (SiH_4) for n-type and the organometallic source Bis-cyclopentadienylmagnesium (Cp_2Mg) for p-type doping with Magnesium. Nitrogen is used as carrier gas. Prior to growth, the substrates are degreased in organic solvents and deionized water. After loading the substrate into the reactor, it is heated up to 1000 °C under Nitrogen and Ammonia to remove surface impurities and to nitridate the sapphire surface. Subsequently the substrate temperature is lowered to 600 °C to deposit a GaN nucleation layer. Due to the large lattice mismatch between GaN and sapphire of approximately 14 %, partially polycrystalline nucleation layers are mandatory to form a lattice transition between substrate and GaN layer. Quality of the GaN films strongly depends on these initial growth steps. The optimized thickness of the nucleation layer is approximately 30 nm. After deposition of the nucleation layer, the reactor temperature is raised to temperatures between 1020 and 1060 °C to grow GaN films. The investigated pn structures consist of the following layers: on top of the nucleation layer, a 1–1.5 μm thick undoped GaN layer is grown. During growth of this layer, the flow rates of NH_3 and TEGa are maintained at 2.0 l/min and 18 μmol/min, respectively. Growth temperature is kept at 1020 °C. Due to the fact, that the undoped GaN

layers are highly n - type, additional doping with SiH_4 is not necessary. Then growth temperature is raised to 1060 °C to grow a 0.5 μm thick p - type GaN layer using Cp_2Mg at a flow rate of 20 nmol/min. After growth, thermal annealing in Nitrogen ambient at 750 °C for 15 min is performed to obtain p - type GaN films. Fabrication of devices is accomplished as follows: p- and n-contact regions are defined by contact lithography and the p - type GaN layer is partially removed using chemically assisted ion beam etching (CAIBE). Details of processing and etching are described in the articles by M. Schauler and F. Eberhard. A Ni/Au contact is evaporated onto the p - type layer and a Ti/Al contact onto the n-type layer. Fig. 1 shows a schematic of a processed device.

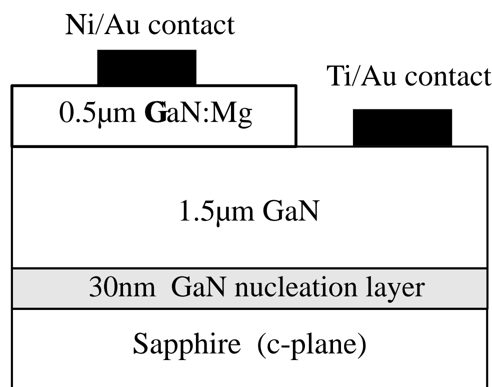

Fig. 1. Cross section of a complete homotype GaN pn diode.

Characteristics of the devices are measured under direct current conditions at room temperature. In Fig. 2, an IV characteristic of such a homotype pn junction is shown. Turn on voltages are between 3.4 and 4 V, corresponding to the bandgap energy of GaN of 3.4 eV at room temperature. Reverse breakdown voltages are about 10 V. Fig. 3 shows electroluminescence spectra of a GaN homojunction LED at forward currents of 0.5, 1.5 and 2 mA, respectively. The peak wavelength is around 385 nm and the full width at half-maximum (FWHM) is 450 meV. The visible emission wavelength regime results from a magnesium related transition 350 meV below the bandgap of GaN [7].

To improve luminescence intensity of the devices, an approximately 100 nm thick InGaN recombination layer grown at 850 °C is inserted between the n-type GaN and the Mg - doped GaN layer to form a double heterostructure (DH) LED. Growth of InGaN with reasonable Indium contents needs comparatively low growth temperatures due to the high vapor pressure of Indium. The reduced growth temperature decreases optical and crystal quality of nitride films. The device structure of an GaN/InGaN - DH LED is displayed in Fig. 4.

Fig. 5 presents the IV characteristic of a DH LED. Turn on voltages are higher than those of the GaN homojunction LED due to the higher series resistance. The peak wavelength of room temperature electroluminesence shifts to shorter wavelengths with increasing forward current from about 415 nm at 1.4 mA to 406 nm at 1.6 mA and 388 nm at 2.2 mA as shown in Fig. 6. This behavior is not observed for GaN homojunction LEDs. We assume that recombination takes place in the InGaN layer at low current densities, whereas at higher current densities recombination occurs in the Mg - doped GaN.

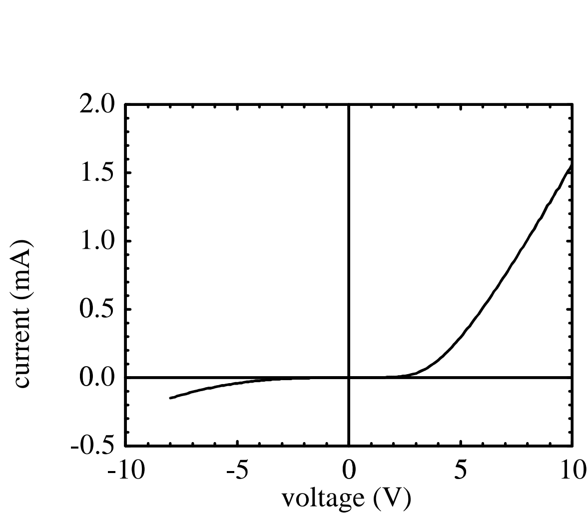

Fig. 2. IV characteristic of a homotype GaN pn-junction.

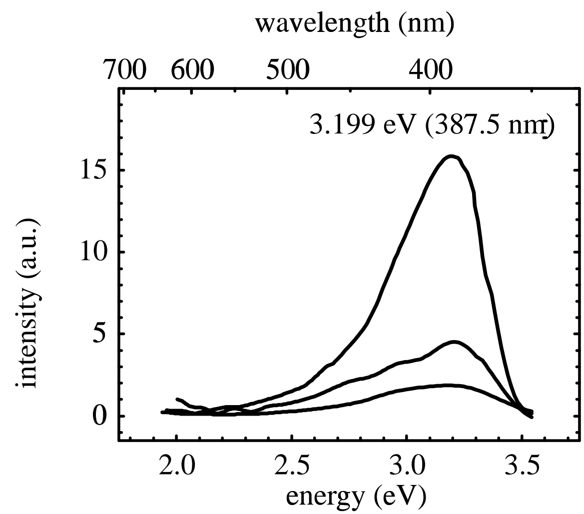

Fig. 3. Electroluminescence spectra of a GaN pn-junction for various forward currents.

The In-content of the InGaN-layer is estimated from the emission wavelength at low currents to be about 15 % in accordance with X-ray diffraction (XRD) measurements.

3. Conclusions

GaN pn-junctions have been grown with low pressure MOVPE, using Mg-doped GaN layers and low temperature GaN nucleation layers. The devices show visible light emission at room temperature under DC bias conditions. Luminescence intensity was improved by inserting an InGaN recombination layer. But electroluminescence is still faint in comparison to NICHIA blue LEDs and further process optimization is required to obtain better p-type conduction and brighter blue luminescence.

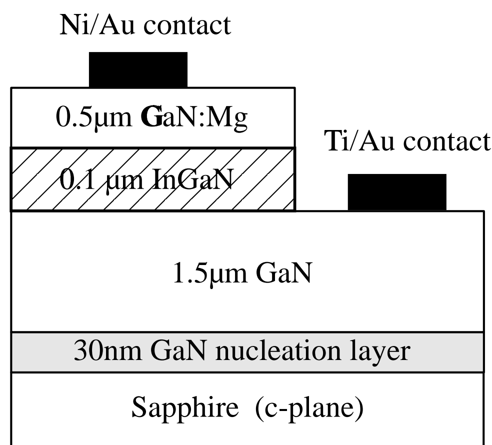

Fig. 4. Device structure of a GaN/InGaN DH LED.

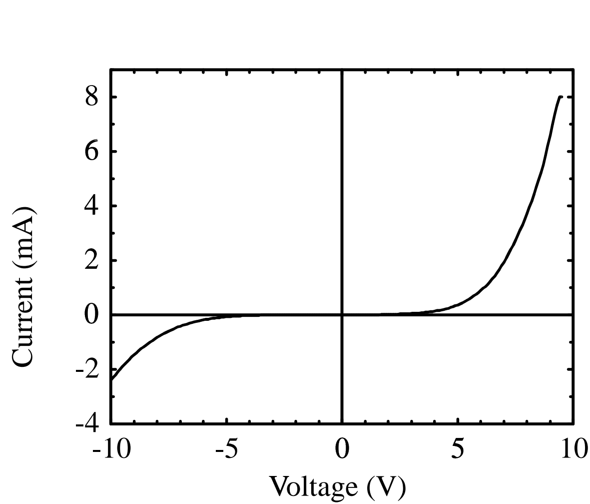

Fig. 5. Current-voltage characteristic of a GaN/InGaN DH LED.

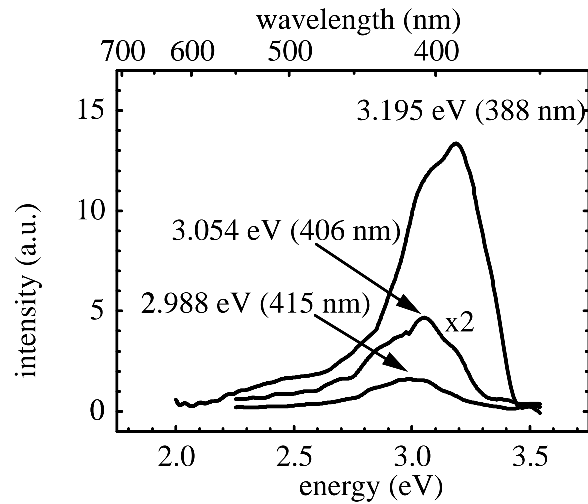

Fig. 6. Electroluminescence spectra of a GaN/InGaN DH LED for various forward currents.

References

[1] S. Strite and H. Morkoç, "GaN, AlN, and InN: A review" *J. Vac. Sci. Technol.* B 10, p. 1237, 1992.

[2] H. Morkoç, S. Strite, G. B. Gao, M. E. Lin, B. Sverdlov, and M. Burns, "Large-band-gap SiC, III-VI nitride, and II-VI ZnSe-based semiconductor device technologies", *J. Appl. Phys.*, vol. 76, p. 1363, 1994.

[3] H. Amano, M. Kito, K. Hiramatsu, and I. Akasaki, "P-type conduction in Mg-doped GaN treated with low-energy electron beam irradiation", *Jpn. J. Appl. Phys.*, vol. 28, p. L2112, 1989.

[4] S. Nakamura, T. Mukai, M. Senoh, and N. Iwasa, "Thermal annealing effects on p-type-doped GaN films", *Jpn. J. Appl. Phys.*, vol. 31, p. L139, 1992.

[5] S. Nakamura, M. Senoh, N. Iwasa, and S. Nagahama, "High-Brightness InGaN Blue, Green and Yellow Light Emitting Diodes with Quantum Well Structures", *Jpn. J. Appl. Phys.*, vol. 34, pp. L 797–L 799, 1995.

[6] S. Nakamura, M. Senoh, S. Nagahama, N. Iwasa, T. Yamada, T. Matsushita, H. Kiyoku, and Y. Sugimoto, "InGaN-based Multi-Quantum-Well-Structure Laser Diodes" *Jpn. J. Appl. Phys.*, vol. 35, pp. L 74–L 76, 1996.

[7] S. Nakamura, T. Mukai, and M. Senoh, "High-Power GaN P-N Junction Blue-Light-Emitting Diodes" *Jpn. J. Appl. Phys.*, vol. 30, pp. L 1998–L 2001, 1991.

Molecular Beam Epitaxy of GaN — Homoepitaxial Films and LEDs

Markus Mayer, Markus Kamp

The use of on surface cracked (OSC) ammonia as nitrogen precursor for molecular beam epitaxy of nitrides has been established. Homoepitaxial GaN films are grown on GaN single crystal substrates. The deposited films are examined by low-temperature photoluminescence. A rich excitonic spectrum with record PL linewidths as small as 0.5 meV is observed. These transitions can be explained with excitons bound to neutral donors ($(D^\circ, X)_1$ at 3.4709 eV, $(D^\circ, X)_2$ at 3.4718 eV) and to a neutral acceptor ((A°, X) at 3.4663 eV). In addition, free exciton lines are observed at 3.4785 eV, 3.4832 eV, and 3.499 eV for excitons A, B, and C, respectively. In heteroepitaxial GaN, photoluminescence linewidths of 5 meV and free electron concentrations of 10^{17} cm^{-3} with mobilities of 220 cm^2/Vs are obtained. Additionally, p- and n-doping, current-voltage characteristics as well as photoluminescence and eletroluminescence properties of homotype GaN light emittiong diodes are reported.

1. Introduction

GaN attracts attention of numerous research groups because of its wide direct bandgap (room temperature: $E_g = 3.4$ eV) and the extraordinary photoluminescence (PL) efficiencies at near bandgap energies. These properties make the group III nitrides a highly promising candidate for applications in optoelectronic devices operating in a spectral region which is not covered by other III-V semiconductors. The steady flow of reports on GaN-based light-emitting diodes (LEDs) published over the last years has recently been highlighted by the first GaN-based injection diode laser [1].

For most semiconductor systems high quality devices are achieved with homoepitaxial growth. Homoepitaxial growth of group III nitride based devices should also be favorable compared to the heteroepitaxy of nitrides on sapphire or silicon carbide, where misfit dislocations are generated. Employing bulk GaN as substrate crystal it is expected to reduce the dislocation density leading to a significant improvement of the GaN layer quality. Quite generally, homoepitaxy may open new perspectives for commercial applications of group III nitrides.

We report on PL properties of homoepitaxially grown GaN. For the first time molecular beam epitaxy (MBE) film qualities are achieved, that are comparable or even superior to nitride layers grown by metal organic vapor phase epitaxy (MOVPE). Using heteroepitaxial growth on sapphire substrate, we demonstrate homotype LEDs. Typical current-voltage characteristics of these LEDs and electroluminescence (EL) are discussed.

2. Growth and Characterization

For epitaxy an almost standard molecular beam epitaxy (MBE) system (Riber 32) is used, which has been adapted to group V gas sources. NH_3 is introduced into the growth chamber through a standard high temperature gas injector (Riber HTI 432). The decomposition of NH_3 is carried out with an on surface cracking technique, where the ammonia molecules are thermally cracked on the growing surface. Elemental Ga, Al, In and Mg is supplied by effusion cells. As an additional Mg source methalorganic bismethylcyclopentadienyl-magnesium is used. Growth of homoepitaxial GaN films is performed without deposition of a nucleation layer at a growth termperature of 720 °C. Neither mechanical nor chemical pretreatment is done before the growth.

Heteroepitaxial growth is commonly performed on c-plane sapphire. The advantages of sapphire as substrate crystal are high temperature resistence, excellent crystal qulities and hexagonal structure (corund) as well as low price. Due to the high lattice mismatch of 15 % to GaN, the nitridation and deposition of a thin nucleation layer are essentiell.

Unless otherwise mentioned, the standard nitridation is performed at a NH_3 pressure of 1.5×10^{-5} mbar at a temperature of 900 °C for 5 min. After nitridation the substrate temperature is reduced to 500 °C for deposition of an about 20 nm GaN nucleation layer. This film is grown at Ga and NH_3 pressures of 5.2×10^{-7} mbar and of 1×10^{-5} mbar, respectively. For subsequent growth of the GaN layer, the temperature is increased again to 800 °C.

For characterization of the grown layers, x-ray diffraction, photoluminescence and electroluminescence are used. The optical excitation is performed with a 1 mW HeCd laser (325 nm). The PL data are taken using a Spex 500 M spectrometer connected to a GaAs photomultiplier (Hamamatsu R943 02). Particularly for homoepitaxial GaN the spectra is calibrated using two ultraviolet lines of an argon ion laser at 351.1 nm and 363.8 nm wavelength. Spectral resolution is better than 0.3 meV.

3. Homoepitaxy

Fig. 1 shows a typical PL spectrum of a 0.4 μm thick GaN film. For interpretation of the spectrum we consider high energy free and lower energy bound exciton regimes. The free excitonic part is explained as follows: as a result of axial crystal field and spin orbit interaction the valence band of α-GaN (wurtzite structure) at the Γ point is splitted into three subbands. Because of the valence band splitting, three free excitons, FE_A, FE_B and FE_C are expected. At low temperatures (4.2 K), only two lines can be identified in the high energy part of Fig. 1. These lines at 3.4785 eV and 3.4832 eV are attributed to free exciton transitions FE_A and FE_B, respectively.

A third line, which is crucial to the interpretation of the entire spectrum, emerges from the background at elevated temperatures (80 K) at an energy of 3.494 eV, as shown in Fig. 2. This third excitonic transition is interpreted as FE_C. With decreasing temperature, the energy positions of the three excitons shift towards higher energies. In the temperature range from 80 K to 4.2 K, the shift for FE_A and FE_B transitions is 5 meV. This energy shift is in agreement with data determined from absorption measurements of the energy gap [2]. Based on these results, the extrapolated energy of the FE_C at 4.2 K is 3.499 eV.

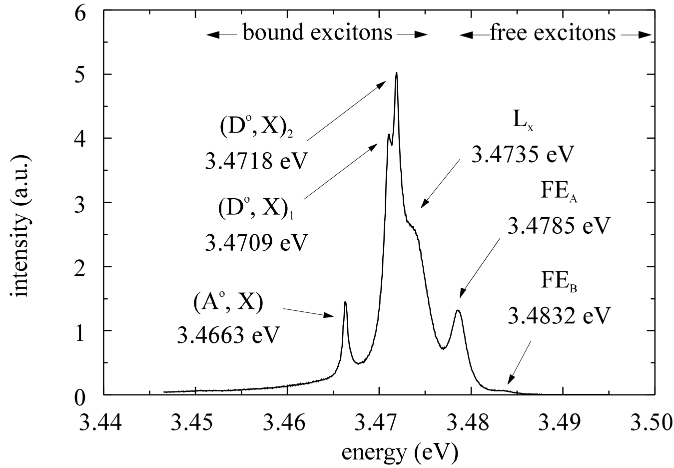

Fig. 1. Photoluminescence spectrum (4.2 K) of homoepitaxial undoped GaN.

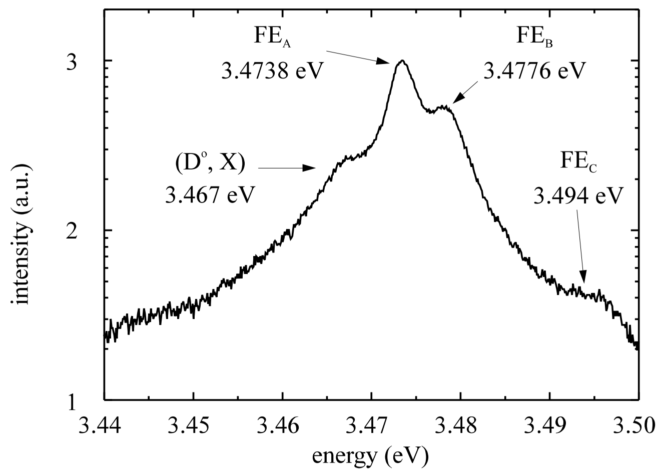

Fig. 2. Luminescence spectra in the exciton region (at 80 K). In contrast to the low-temperature PL the free excitons are dominating the spectra and the FE_C line is visible.

The positions of the free excitonic lines are in a good agreement with the values reported for thick (unstrained) GaN films on sapphire [3, 4] and for homoepitaxial GaN [5] as indicated in Tab. 3. By adding the exciton thermal activation energy of 27 meV[6] to the energy of the FE_A, a value of $E_g = 3.505$ eV for the bandgap energy is obtained. A comparable bandgap energy of $E_g = 3.503$ eV was reported by Monemar et al. [4].

The origin of the line centered at 3.4735 eV is subject to further investigation. It can correspond to an exciton, bound to a very shallow donor, or to a donor bound exciton formed by an electron and a hole from a deeper Γ_7 valance band. Two lines at 3.4718 eV and 3.4709 eV have much smaller linewidths of 0.5 meV and 0.7 meV, respectively. We attribute these lines to excitons bound to different neutral donors ($(D°, X)_{1,2}$). In all our spectra, the lines are distinctly separated by an energy of 1 meV. In MOVPE grown GaN, Pakula et al. [5] observed one (D°, X) transition at 3.4719 eV, which shows a double-peak fine structure. Although this double-peak was not clearly resolved, they mentioned that it can be fitted with two Lorentzian lines. To the best of our knowledge, we are able for the first time to resolve these two donor bound transitions in low-temperature luminescence experiments. In addition to shallow donors, PL measurements

Tab. 3. Low-temperature ($T < 10\,\text{K}$) free and bound exciton energies in thick heteroepitaxial GaN (grown on sapphire) and in homoepitaxial GaN

FE_A (eV)	FE_B (eV)	FE_C (eV)	D^oX (eV)	layer thickness (μm)	substrate crystal	author
3.4745	3.4805	3.501	3.467	150	sapphire	Dingle et al. [3]
3.4751	3.4815	3.503	3.469	110	sapphire	Monemar et al. [4]
3.4780	3.4835	3.502	3.4719	2	GaN	Pakula et al. [5]
3.4785	3.4832	3.499	3.4709/3.4718	0.4	GaN	our work

reveal also the presence of a considerable number of acceptors. Their presence is manifestated by the neutral acceptor bound exciton line clearly visible at 3.4663 eV in Fig. 1. The linewidth of this transition is also very narrow (0.7 meV).

The energetic positions of donor bound excitons and free excitons can be used to calculate the exciton localization energy to the shallow donors by: $E_{localized_{1,2}} = E_{FE_A} - E_{(D^o,X)_{1,2}}$

Localization energies of $(D^o, X)_1$ and $(D^o, X)_2$ are 7.6 meV and 6.7 meV, respectively. These values are to be compared with localization energies between 6.1 meV and 13.5 meV reported by other groups [3, 4, 5]. The localization energies of donor and acceptor bound excitons can be used to calculate the activation energies assuming Hayne's rule. This phenomenological rule states proportionality of localization energy and activation energy of an impurity ($E_{localized} = const \times E_D$). For Silicon, the proportionality constant is 0.1 for acceptors and 0.2 for donors. A rough estimation of the activation energies E_{D_1} and E_{D_2} yields 38 meV and 34 meV, respectively. These energies for homoepitaxially grown GaN are in excellent agreement with results of heteroepitaxial GaN grown on sapphire [7], where nitrogen vacancies are assumed to be the origin of the donor level.

At low excitation densities and low temperatures, the (D^o, X) transitions are dominating the spectra. However, the shape of the spectra changes completely with higher excitation intensity. The donor bound transitions saturate and the FE_A becomes dominating.

Tab. 3 compares energies for (D^o, X) transitions obtained by various authors and shows a good agreement within ± 2 meV.

4. Heteroepitaxy

We have grown various binary and ternary layers on c-plane sapphire. The achieved results are summarized as follows:

GaN:

- PL: luminescence dominated by donor bound excitons, linewidths of 5 meV at 4 K
- Hall measurement: free carrier concentrations of $n = 2\times10^{17}\,\text{cm}^{-3}$ with mobilities of $\mu_n = 220\,\text{cm}^2/\text{Vs}$ (300 K)
- Diffraction (XRD): rocking curves with linewidths of 400 arcsec of the (0002) reflex (ω-scan)

AlGaN:

- AlGaN up to 35 % AlN realized (XRD)
- Hall of $Al_{0.17}Ga_{0.83}N$: free carrier concentrations of $n=1\times10^{18}\,cm^{-3}$ with mobilities of $\mu_n=10\,cm^2/Vs$ (300 K)

InGaN:

- InGaN up to 4 % InN realized (XRD)
- PL: luminescence dominated by broad emission at 3.06 eV (300 K)
- Low growth temperatures are essentiell to increase In incorporation

P-doping is one of the major challenges on the way to fabricate light emitting devices in nitrides. Early reports claimed that p doping of GaN in MBE growth can only be achieved if a plasma source is used in addition to the ammonia [8]. Whereas Wang et al. could achieve free hole concentrations with simultaneous use of the plasma cell and ammonia, they were not able to obtain p-doping when only ammonia was used. In our MBE system Mg is supplied as elemental Mg by a standard effusion cell and by the metalorganic precursor bismethylcyclopentadienyl-magnesium (MCp_2Mg) through a low-temperature gas injector. The p-conductivity is still subject of further investigations, but it seems that the metalorganic source improves the electrical properties compared to the elemental Mg. Photoluminescence of Mg doped GaN is presented in Fig. 3. The spectrum is dominated by a narrow transition at 3.26 eV and the corresponding LO phonon replica at lower energies. A typical current-voltage characteristic of a pn-junction is shown in Fig. 4. Indium is used as n-contact to the nominally undoped GaN layer and the p-contact is realized by a gold probe tip. Turn-on voltage is 3–4 V. Using Ti/Au n-contact metallization as well as Ni/Au p-contact formation is expected to lead to lower contact resistances. Electroluminescence of the homojunction LED is indicated in Fig. 5. The luminescence is dominated by a rather steep increase at 380 nm, whereas the linewidth of approx. 85 nm is determined by the long tail towards lower energies. Future work on electroluminescenc has to be concentrated on heterostructures and on improvements of the GaN: Mg films.

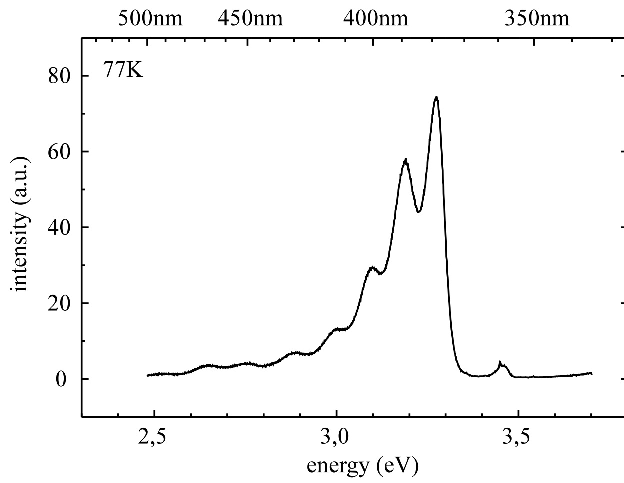

Fig. 3. Photoluminescence of Mg doped GaN (77 K)

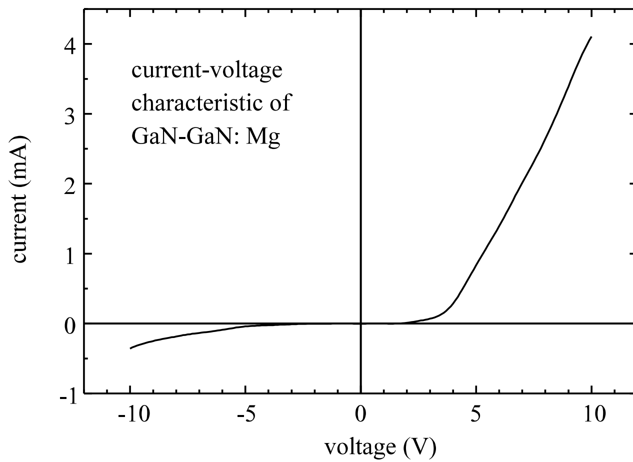

Fig. 4. Typical current-voltage characteristic of homojunction *pn*-diodes

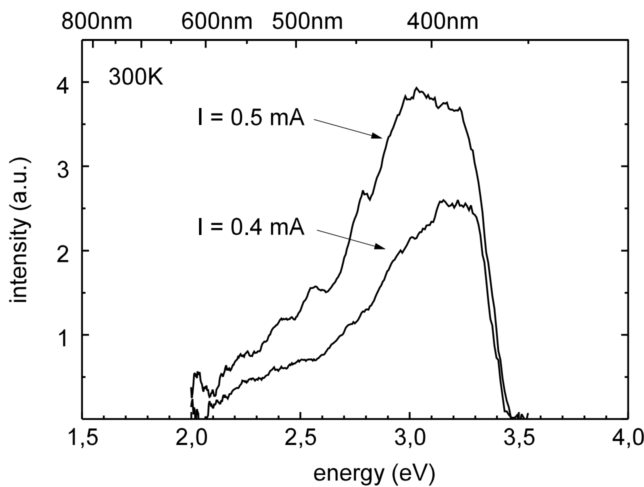

Fig. 5. Electroluminescence spectra of a homotype *pn*-junction (300 K), driven at different current levels.

5. Summary

In conclusion, we have used MBE with NH_3 supply and on surface cracking for growth of high performance GaN based layers. Low-temperature PL of homoepitaxially grown GaN layers reveals extremely narrow linewidths and indicates excellent optical properties. We observed free excitonic transitions FE_A, FE_B and FE_C at energies 3.4785 eV, 3.483 eV and 3.499 eV. We found evidence that the commonly observed (D°, X) transition consists of two donor bound transitions $(D^\circ, X)_{1,2}$ at energies 3.4718 eV and 3.4709 eV and linewidths of 0.5 meV and 0.7 meV, respectively. We assume different neutral donors to be the origin of these two transitions. Work on heteroepitaxial grown material yields excellent optical, electrical and structural properties. First results on electroluminescence of homotype *pn*-junctions in GaN are encouraging.

We like to acknowledge contributions from C. Kirchner, A. Thies, M. Schauler and F. Eberhard as well as the financial support from the German Federal Ministry of Education, Science, Research and Technology (BMBF) and the Volkswagen foundation. The project on the homoepitaxial growth has been performed in close cooperation with the Polish Academy of Science, namely H. Teisseyre, G. Karczewski, G. Nowak, M. Leszczynski, I. Grzegory and S. Porowski.

References

[1] S. Nakamura, M. Senoh, S. Nagahama, N. Iwasa, T. Yamada, T. Matsushita, H. Kiyoku and Y. Sugimoto, “Characteristics of InGaN multi-quantum-well-structure laser diodes”, *Jpn. J. Appl. Phys. Lett.*, vol. 74 (35), 3269–3271, 1996.

[2] H. Teisseyre, P. Perlin, T. Suski, I. Grzegory, S. Porowski, J. Jun, A. Pietraszko and T. D. Moustakas., “Temperature dependence of the energy gap in GaN bulk single crystals and epitaxial layers”, *Jpn. J. Appl. Phys.*, vol. 76, pp. 2429–2434, 1994.

[3] R. Dingel, D.D. Sell, S.E. Stokowski, and M. Illegems, “Absorption, reflectance and luminescence of GaN epitaxial layers”, *Phys. Rev. B*, vol. 4, pp. 1211–1218, 1971.

[4] B.Monemar, “Fundamental energy gap of GaN from photoluminescence excitation spectra, *Phys. Rev. B*, vol. 10, pp. 676–681, 1974.

[5] K. Pakula, A. Wysmołek, K.P. Korona, J.M. Baranowski, R. Stepniewski,I. Grzegory, M. Boćkowski, J. Jun, S. Krukowski, M. Wróbleski, S. Porowski, “Luminescence and reflectivity in the exciton region of homoepitaxial GaN layers grown on GaN substrates”, *Solid State Com.*, vol. 97, pp. 919–922, 1996.

[6] D. Kovalev, B. Averboukh, D. Volm, B. K. Meyer, H. Amano and I. Akasaki, “Free exciton emission in GaN”, *Phys. Rev. B*, vol. 54 (4), pp. 2518–2522, 1996.

[7] R. J. Molnar and T. D. Moustakas, “Growth of gallium nitride by electron-cyclotron resonance plasma-assisted molecular-beam epitaxy: the role of charged species”, *Jpn. J. Appl. Phys.*, vol. 76, pp. 4587-4595, 1994.

[8] C. Wang and R.F. Davis, “Deposition of highly resistive, undoped, and p-type, magnesium-doped gallium nitride films by modified gas source molecular beam epitaxy”, *Appl. Phys. Lett.*, vol. 63 (7), pp. 990–992, 1990

Electrical and Optical Properties of GaN Light Emitting Diodes

Arthur Pelzmann, Markus Kamp

Electroluminescence (EL), photoluminescsence (PL) and I-V characteristics of homotype GaN and heterotype GaN/InGaN pn-junctions were studied. A comparison between homotype light emitting diode (LED) structures, grown by metal organic vapour phase epitaxy (MOVPE) and gas-source molecular beam epitaxy (GSMBE) and InGaN LEDs (by MOVPE) is presented. Processed as well as non processed structures are examined.

1. Introduction

With a bandgap energy between 1.6 eV and 6.2 eV GaN and its related compounds offer the possibility to fabricate light emitting devices covering almost the whole visible spectrum down to ultraviolet (UV) wavelengths. Therefore, GaN based optoelectronic devices are predestinated for blue and green light sources in a wide range of application fields e.g. display technology, traffic lights, blue lasers for enhanced optical data storage. S. Nakamura's work on high brightness LEDs at NIchia Chemicals paved the way into a bright future of GaN based optoelectronic devices [1]. Recent progress in GaN device technology led to the first blue laser diodes operating in continous wave mode at room temperature (RT) for more than 30 h [2].

So far the best results in heteroepitaxial growth of group III nitrides were obtained by MOVPE techniques. However, excellent results have also been achieved by GSMBE [3, 4, 5]. We report on the electrical and optical properties of homo-and heterotype GaN pn-junction LEDs grown by both MOVPE and GSMBE techniques in our Department.

2. Device structures and formation of ohmic contacts

The examined LEDs were grown on c-oriented sapphire substrate material. To reduce the large lattice mismatch between the sapphire and GaN a thin GaN nucleation layer is deposited before growing the main GaN layer. Homojunction LEDs contain a silicon doped GaN layer as n-region followed by a magnesium doped GaN layer as p-region. The investigated MOVPE grown heterojunction has an undoped InGaN recombination layer located between the p- and the n-region. Fig. 1 and 2 show schematics of homo-and heterojunction LEDs.

Different approaches for ohmic contact formation on n-type and p-type material have been investigated. For n-type GaN, soldered In pellets or Ti/Al contacts are used. The p-type contacts are formed by evaporating Ni/Au, Cr/Ni/Au or simply by using an Au needle. Some structures were fully processed using lithography, dry etching and contact metallization. In the following we refer to those structures as processed structures. Figs. 1 and 2 illustrate various approaches used to form ohmic contacts to the layers.

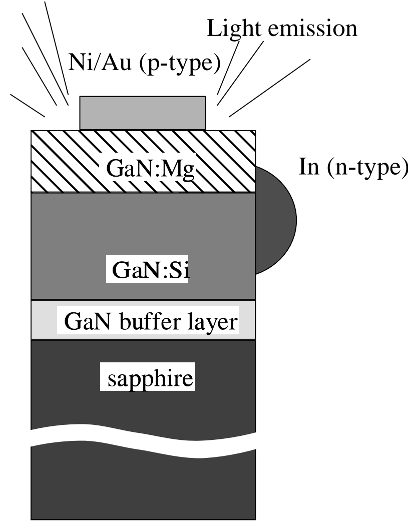

Fig. 1. Schematic of homotype GaN pn-junctions grown by GSMBE and MOVPE.

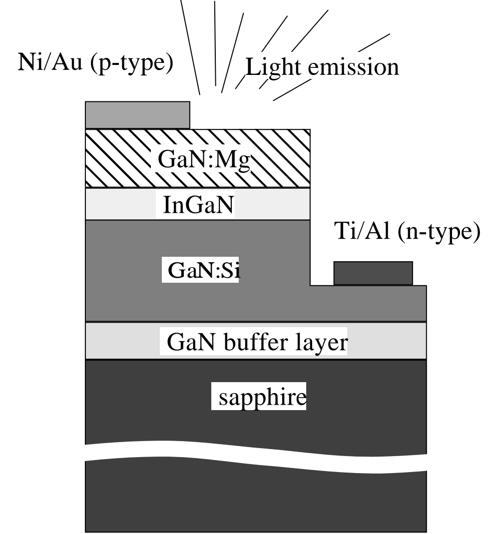

Fig. 2. Schematic of heterotype GaN/InGaN pn-junction grown by MOVPE.

3. Results and discussion

Photoluminescence spectra were taken at 22 K using a He-Cd laser emitting at 325 nm wavelength at a power density of $1.7\,\mathrm{mW/mm^2}$ for excitation. The resulting spectra depicted in Fig. 3 peak at 3.26 eV (380.5 nm) for the MOVPE grown junctions and at 3.27 eV (379.5 nm) for the GSMBE grown samples. The difference of 10 meV of the donor-acceptor pair transition (DAP) can be understood taking Coulomb interactions between the donors and acceptors into account. The energetic position E_n of the DAP shifts to higher energies with decreasing donor-acceptor distances and can be calculated from [6]

$$E_n = E_g - E_D - E_A + \frac{e^2}{\varepsilon R_n} - \frac{\alpha_W}{R_n^6} \quad , \tag{1}$$

where E_g, E_D and E_A are energy gap, donor and acceptor ionization energy respectively, ε is the dielectric constant and R_n is the donor-acceptor separation. The van der Waals interaction which plays a role only for very close donor-acceptor pairs is taken into account by $\alpha_W = 1000\,\mathrm{eV\AA^6}$. However, an effect of the residual strain in the layers grown by the two techniques cannot be excluded.

All spectra show additional LO-phonon replica approximately 90 meV below the DAP transitions. The phonon replica of the InGaN heterojunction appears at a remarkable high intensity. We assume that the measured spectral profile represents a convolution of the LO-phonon replica and InGaN lines corresponding to about 10 % In content [1].

Additionally to PL measurements EL spectra of the samples were recorded. For the RT EL measurements the samples were mounted on a sample holder and gold needles were used for current supply. Fig. 4 shows the RT EL spectra of a non-processed MOVPE homojunction using In contacts for the n-type material and Ni/Au contacts for the p-type material. Light

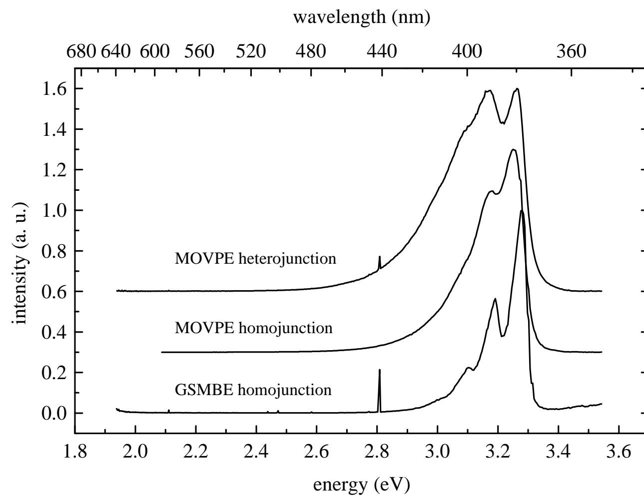

Fig. 3. Photoluminescence spectra of GaN pn homojunctions and a GaN/InGaN heterojunction at 22 K.

generation of the structures occurs under the p-contact. Therefore, the EL of the non-processed structures was measured through the transparent sapphire substrate.

The EL spectra for 0.5 mA, 1.5 mA and 2 mA forward bias current peak at 3.199 eV (387.5 nm) and no obvious current dependent peak shift is observed. Therefore, we assume electron-hole pair (EHP) recombination recombine in the Mg doped region. The energetic position agrees well with conduction-band-acceptor transitions (Mg level 200 meV above the valence band) observed in PL. With electron mobilities about 10 times higher than the holes this is not surprising since electrons penetrate much faster into the p-type region than vice versa when a forward bias is applied to the junction.

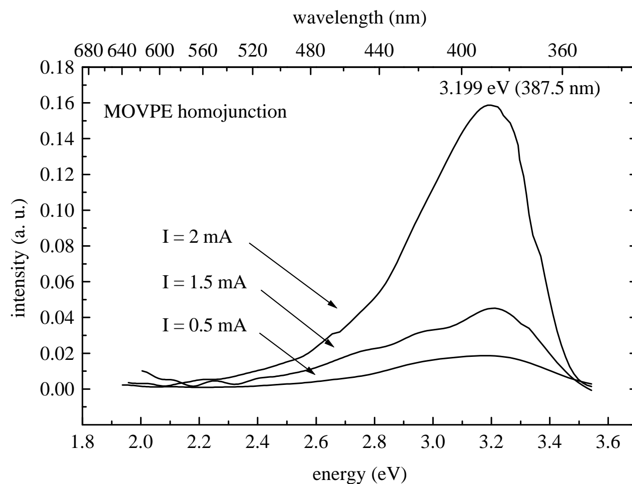

Fig. 4. Electroluminescence spectra of a non-processed GaN MOVPE pn homojunction at 300 K.

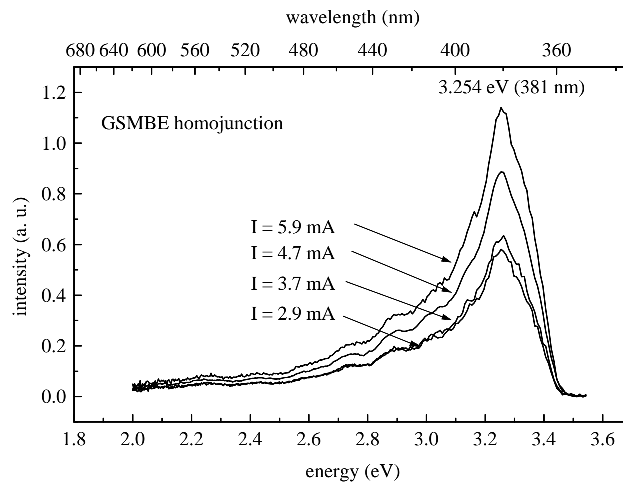

Fig. 5. Electroluminescence spectra of a non-processed GaN GSMBE pn homojunction at 300 K.

Fig. 5 depicts the RT EL of the processed GSMBE homotype pn-junction. Here, the spectra at four different currents were measured. The EL spectra of this sample are approximately 7 times more intensive than those of the non-processed diodes. This intensity gain is due to an enhanced p-type contact geometry which allows light output through the surface of the layer (pp. 92–95). As with MOVPE homojunction samples no current dependent peak shift was observed.

The MOVPE heterojunction RT EL depicted in Fig. 6 peaks at 2.988 eV (415 nm), 3.054 eV (406 nm) and 3.195 eV (388 nm) for forward currents of 1.4 mA, 1.6 mA and 2.2 mA, respectively. This blue shift could be explained by a convolution of a constant intensity InGaN peak and a DAP with increasing intensity for increasing current.

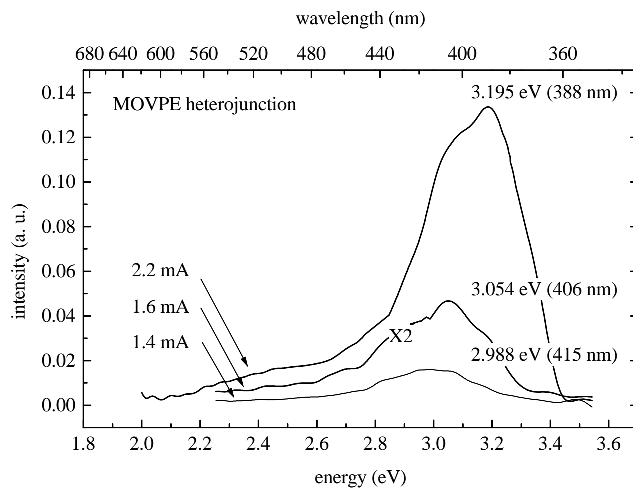

Fig. 6. Electroluminescence spectra of a processed GaN/InGaN MOVPE pn heterojunction at 300 K.

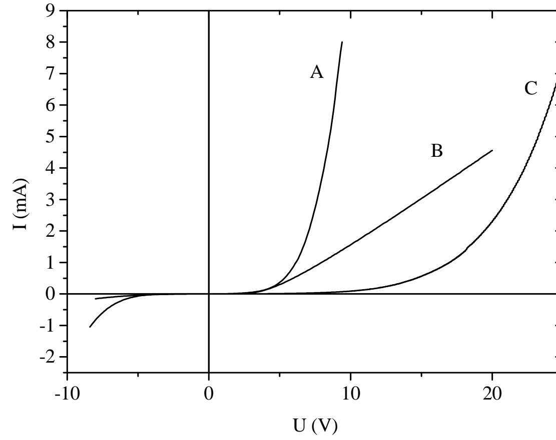

Fig. 7. I-V characteristic of the pn-junctions. Curve A belongs to the processed MOVPE heterojunction, curve B to the non-processed MOVPE homojunction and curve C to the processed GSMBE homojunction.

The I-V characteristics of the layer structures described above are shown in Fig. 7. To correct for the series resistances i.e. bulk resistances of p- and n-material and contact resistances a very simple estimation is used. A p-n junction with a series resistance R_s can be described by

$$I(U) = I_0(e^{\frac{q(U-R_sI)}{nk_BT}} - 1) \quad , \tag{2}$$

where I is the current, I_0 the reverse saturation current, q the electronic charge, U the applied voltage, k_B is Boltzmann's constant, T the temperature and n represents the ideality factor. For positive voltages larger than a few nk_BT/q, the exponential term is much larger than unity. Therefore the series resistance can be obtained by plotting the data versus I according to

$$\ln(I)\frac{nk_BT}{q} - U = -IR + \ln(I_0)\frac{nk_BT}{q} \quad . \tag{3}$$

The slope of this plot yields the series resistance. Ideality factors varying between 1 and 2 were used for fitting the curves but it turned out that its effect on the series resistances was negligible for high currents. Correcting the measured I-V characteristics for the series resistances calculated as indicated above yields turn on voltages of about 3.5 V. The non-processed MOVPE sample has a high resistance of 3.547 kΩ due to large spacing between contacts. The processed GSMBE homojunction has a series resistance of 1.1 kΩ whereas 377 Ω were calculated for the processed MOVPE grown heterojunction indicating good contact and material qualities.

4. Summary

MOVPE and GSMBE grown GaN homotype p-n junctions and MOVPE grown GaN/InGaN heterojunctions have been examined. Homotype LEDs show good agreement for PL and EL, both indicating DAP transitions being the recombination channels. The heterojunction current dependent EL indicates a saturable InGaN recombination and a DAP recombination, dominating

at higher currents. I-V mesurements show good p-n characteristics with turn on voltages of about 3.5 V. The series resistances are 377 Ω and 1.1 kΩ for the processed structures. Future work will include optimization of the vertical device structure and the p-contacts.

References

[1] S. Nakamura, "InGaN/AlGaN blue-light-emitting diodes", *J. Vac. Sci. Technol. A*, vol. 13(3), pp. 705–710, 1994.

[2] S. Nakamura, M. Senoh, N. Iwasa, S. Nagahama, T. Yamada, T. Matsushita, "InGaN-Based Multi-Quantum-Well-Structure Laser Diodes", *Jpn. J. Appl. Phys.*, vol. 35 (2), no. 1B, pp. L74–L76, 1996.

[3] U. Strauss, H. Tews, H. Riechert, R. Averbeck, M. Schiele, B. Jobst, D. Volm, T. Streibl, B. K. Meyer, W. W. Rühle, "Identification of a Cubic Phase in Epitaxial Layers of Predominantly Hexagonal GaN", *MRS Internet J. Nitride Semicond. Res.*, vol. 1, no. 44, 1996.

[4] M. Kamp, M. Mayer, A. Pelzmann, H. Y. Chung, H. Sternschulte, K. J. Ebeling, "Thermally cracked NH_3 for MBE Growth of GaN", in *Proc. Topical Workshop on III-V Nitrides*, Nagoya, Japan, 1995.

[5] M. Kamp, M. Mayer, A. Pelzmann, K. J. Ebeling, "On Surface Cracking of ammonia for MBE growth of GaN", in *Mat. Res. Soc. Symp. Proc.*, vol. 449, 1996.

[6] A. Wysmołek, J. M. Baranowski, K. Pakuła, K. P. Korona, I. Grzegory, M. Wróblewsi, S. Porowski, "Donor-Acceptor Pair Spectra in p-type Homoepitaxial GaN Layers", in *Intern. Symp. on Blue Laser and Light Emitting Diodes*, Chiba Univ., Japan, pp. 492–495, March 5–7, 1996.

Fabrication of GaN LEDs

Markus Schauler

In this report, the fabrication of blue light emitting diodes (LEDs) made out of GaN is described. The electrical and optical properties of the devices are discussed.

1. Introduction

Classical III-V semiconductors like GaAs, AlGaAs or InGaP have been used for years for the fabrication of light emitting devices. Due to the small bandgap of these materials, light emission in the blue or UV regime cannot be achived. Group-III nitrides (like GaN, AlN, InN and their alloys), however, cover a bandgap range from 1.6 to 6.2 eV, which makes them ideal candidates for the fabrication of LEDs and semiconductor lasers in the blue and UV spectral range.

The first nitride-based blue high-brightness LED grown by metal-organic vapor-phase epitaxy (MOVPE) was presented by S. Nakamura in 1994 [1]. Meanwhile a GaN-based UV semiconductor laser has been presented by the same group.

In the Department of Optoelectronics, GaN is grown in two different ways: either by molecular-beam epitaxy (MBE) (see pp. 79–85) using NH_3 as a precursor or by MOVPE [3]. In both cases, c-plane oriented sapphire is used as substrate material.

2. Process Technology

The LEDs have been fabricated out of MOVPE grown material. Details of the growth process are reported elsewhere in this report (pp. 75–78). In the first photolithographic step, the mesa structure is defined. This mesa is etched by chemically-assisted ion-beam etching. Using gas flows of 6 sccm Ar and 6 sccm Cl_2, an etch rate of 70 nm/min is achieved. In addition, steep side walls and a smooth semiconductor surface are created, as reported earlier [4]. Afterwards, to remove all organic depositions from the surface, the samples are boiled in acetone, isopropanol, and methanol. The n-contact areas are defined by the second lithographic step. The contact itself is made by lift-off technique and consists of 30 nm-thick Ti, strenghtend with a 150 nm-thick Au layer. The last photolithographic process is p-contact metalization. For contact formation, Ni/Au or Cr/Ni/Au layers are used. An overview of the process sequence is illustrated in Fig. 1.

Each unit cell of the mask design contains one large area LED ($400\,\mu\text{m} \times 400\,\mu\text{m}$), three small LEDs ($200\,\mu\text{m} \times 200\,\mu\text{m}$), one circular LED structure, and two circular test structures for contact resistance measurements, one on p-type, the other on n-type material. The measurement theory is described in [2]. Figure 2 shows an SEM micrograph of this unit cell.

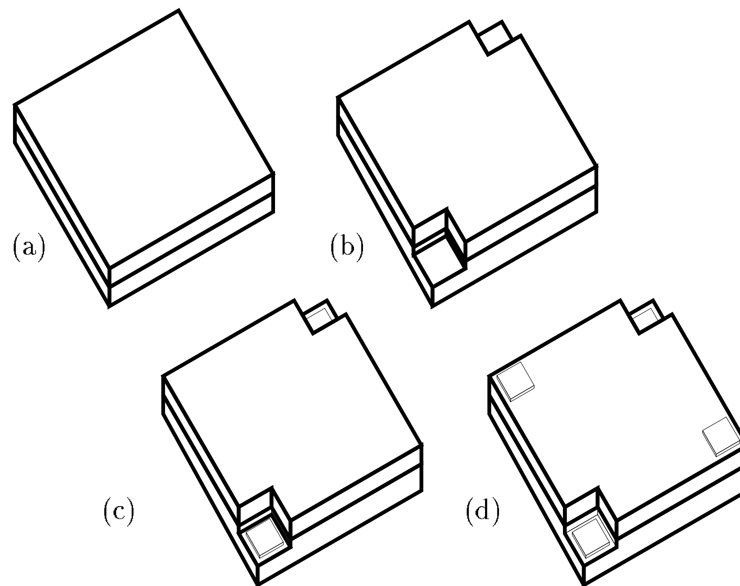

Fig. 1. Process steps for LED fabrication: (a) after epitaxial growth, (b) after mesa etching using chemically-assisted ion-beam etching, (c) after n-contact metalization, and (d) after p-contact metalization.

Fig. 2. Scanning electron micrograph of different LED structures and of circular transmission-line test structures. The total size of this picture is $850\,\mu$m $\times$ $800\,\mu$m. One unit cells contains three small rectangular LEDs (top left), one circular LED, one large area LED (down right) and two circular test structures for resistance measurements.

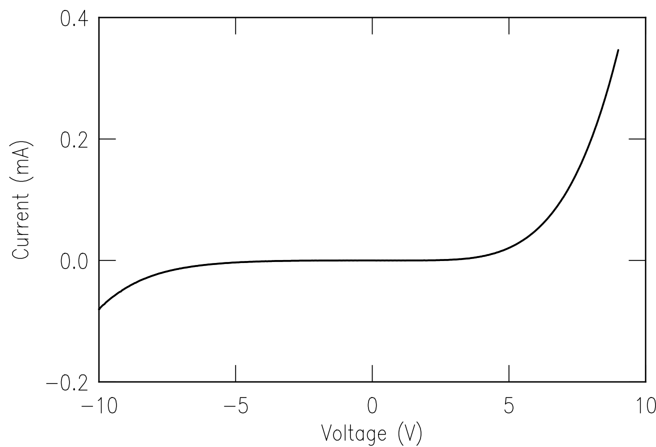

Fig. 3. *IV* characteristic of the blue GaN LED.

3. Results

The described process leads to blue emitting LEDs with *IV* characteristics like that shown in Fig. 3. The turn-on voltage of the devices is between 2.5 and 3 V. Breakdown occurs at a reverse voltage of approximately 6 V. The LED features a series resistance of 5.5 kΩ, which is quite high compared to the series restistance of commercial available devices.

The *n* contacts yield perfectly ohmic behavior with contact resistances down to $3{\cdot}10^{-5}\,\Omega\mathrm{cm}^{-2}$. In contrast, most contacts to *p*-type material expose rectifying characteristics with a breaktrough voltage of about 0.5 V. This prevents exact determination of the specific contact restistance. Using a simplified measurement technique, the *p*-contact resistance is found to be approximately $1 \cdot 10^{-3}\,\Omega\mathrm{cm}^{-2}$.

The devices start electrolumiscating from a driving voltage of about 3 V. A typical EL spectrum is shown in Fig. 4. Due to the long tail of the spectrum ranging form 450 to 550 nm, the emitted light appears not pure blue but blueish white. The intensity of the generated light has been significantly increased by changing the shape of the *p*-contact electrode. Instead of a simple

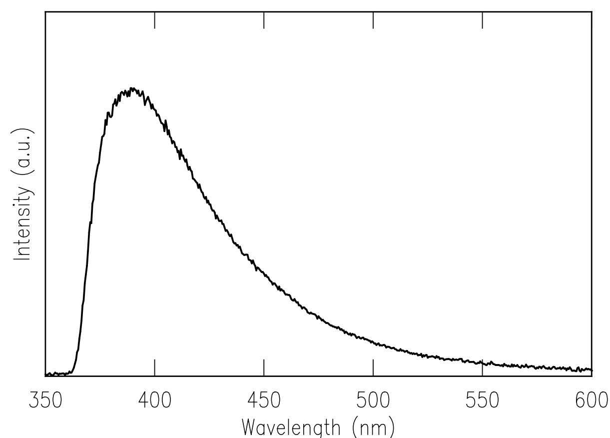

Fig. 4. Electroluminescence spectrum of the blue GaN LED.

Fig. 5. Photograph of the blue GaN LED. The driving current of 20 mA is injected through the two gold needles. The size of the light emitting area is $400\,\mu$m $\times$ $400\,\mu$m.

rectangular shape, the enhanced contact consists of a grid, formed by $10\,\mu$m separated $5\,\mu$m thick bars. This improved electrode is responsible for a very homogeneous current injection into the *p*-doped material and therefore induces a homogenous electroluminescence intensity over the whole device area. A photograph of this improved device is shown in Fig. 5. A more detailed analysis of EL spectra is given in pp. 86–91.

Although extensive life-time testing has not be done yet, the fabricated devices have shown electroluminescence for several days under cw conditions (20 mA operating current) without any visible degradation.

References

[1] S. Nakamura, M. Senoh, and T. Mukai, "Candela-class high-brighness InGaN/AlGaN double-heterostructure blue-light-emitting diodes", *Appl. Phys. Lett.*, vol. 64, no. 13, pp. 1687–1689, 1994.

[2] G. K. Reeves, "Specific contact resistance using a circular transmission line model", *Solid–State Electronics*, vol. 23, pp. 487–490, 1980.

[3] C. Kirchner, "MOVPE Growth of Group III Nitrides", *Department of Optoelectronics, University of Ulm, Annual Report 1995*, pp. 68–74, 1996.

[4] F. Eberhard, M. Schauler, "Sputter etching of GaAs and GaN", *Department of Optoelectronics, University of Ulm, Annual Report 1995*, pp. 96–101, 1996.

Chemically-assisted ion-beam etching of GaN

Franz Eberhard

Chemically-assisted ion-beam etching (CAIBE) of gallium nitride has been investigated using a 400 eV ion beam and a gas mixture of Ar and Cl_2. Increased etch rates have been obtained for samples etched with chlorine compared to those etched by Ar ion milling only. A variation of substrate temperature in the range of 0 to 100°C does not influence the etch rate.

1. Introduction

Wide-bandgap semiconductors like InN, AlN, GaN and their ternary alloys are very attractive for electronic applications and photonic devices. In the last few years, excellent progress has been made in the growth of these materials [1]. One limit for the achievement of better devices is the lack of suitable processing techniques, especially etching. It is well known that GaN is resistant to the most acids and bases at room temperature. Even at higher temperatures only small etching rates can be obtained [1]. A more sophisticated technique is the light-induced wet-chemical etching. This technique suffers from several drawbacks, e.g. the variation of etch rate with material quality and the roughness of the etched surfaces as shown in Fig. 1 [D-21]. In comparison, our dry-etched GaN surfaces are much smoother, as can be seen in Fig. 2, and the etch rate does not depend on the material quality.

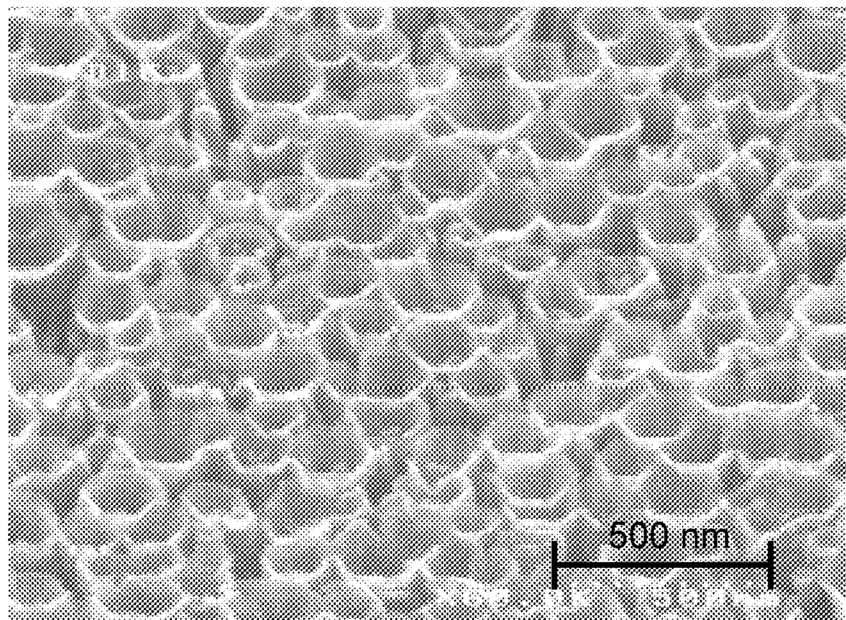

Fig. 1. Photoelectro-chemical etched surface of GaN (H_3PO_4:HNO_3:H_2O).

Fig. 2. CAIBE-etched surface of GaN.

2. Experimental

Epitaxial GaN layers grown on sapphire have been dry etched with a chemically-assisted ion-beam etching system. This system is equipped with an electron-cyclotron-resonance ion-beam source, a load lock system and a sample stage, that can be temperature controlled in the range of -20 to $125\,°C$. The stainless steel chamber is turbo pumped with a base pressure of less than $5 \cdot 10^{-8}$ mbar. The etching mask is provided by photoresist which has been patterned using optical contact lithography. The samples have been mounted on a transfer plate with a thermally conductive paste. All samples have been etched at normal incidence with an Ar flow of 10 sccm and a beam energy of 400 eV. The microwave power and the magnetic field have been maintained at 200 W and 110 mT, respectively.

The etch rates of GaN at various Cl_2 flows are shown in Fig. 3. For a chlorine flow of 0 sccm, the etching mode is ion milling and the material is removed only due to the momentum transfer of the inert Ar ions. By introducing chlorine through the gas feed ring into the chamber, the etch rate and the current density increases, with a maximum at a chlorine flow of 2 sccm. A further increase causes a reduction of both, etch rate and current density. But the ratio of etch rate to current density increases strongly with increased chlorine flow, and it can be concluded, that under the conditions of this work, there is a considerable chemical etching component. In contrast to [1], at our conditions the substrate temperature does not effect the etch rate, as can be seen in Fig. 4. Because of this behavior, there is no need for extensive heat sinking and substrate temperature control. With improved source parameters it is possible to increase the current density and the etch rate.

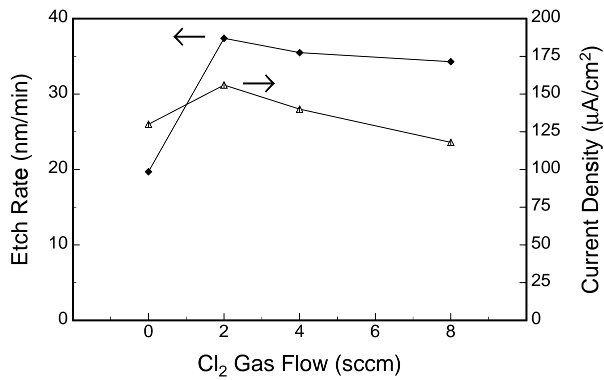

Fig. 3. Influence of chlorine flow on the current density and etch rate of GaN.

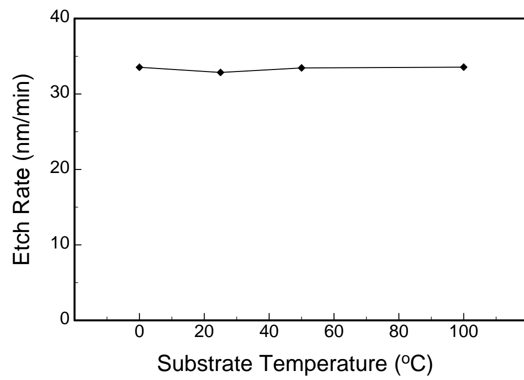

Fig. 4. Etch rate of GaN as a function of substrate temperature.

References

[1] I. Adesida, A. T. Ping, C. Youtsey, T. Dow, M. Asif Kahn, D. T. Olson, and J. N. Kuznia, "Characteristics of chemically assisted ion beam etching of gallium nitride", *Appl. Phys. Lett.*, vol. 65, pp. 889–891, 1994.

Ph.D. Theses

[Ph.D.-1] Kummetz, T., *AlGaInAs/InP-Molekularstrahlepitaxie für Metall-Halbleiter-Metall-Photodetektoren und -Modulatoren*, Ph.D. Thesis, Dept. of Optoelectronics, University of Ulm, 1996.

[Ph.D.-2] Sickmöller, M., *Korrelations- und Zeitbereichsverfahren zur Untersuchung des Kurzzeitverhaltens optisch anregbarer Halbleiter-Strukturen*, Ph.D. Thesis, Dept. of Optoelectronics, University of Ulm, 1996.

[Ph.D.-3] Michalzik, R., *Modellierung und Design von Laserdioden mit Vertikalresonator*, Ph.D. Thesis, Dept. of Optoelectronics, University of Ulm, 1996.

Diploma Theses and Semester Projects

[D-1] Jäger, Roland, *Wachstum und Charakterisierung von AlGaAs-Quantenfilmen für Laserdioden*, Diploma Thesis, Dept. of Optoelectronics, University of Ulm, 1996.

[D-2] Kemmner, Harald, *Gitterspektrometer mit CCD-Zeile*, Semester Project, Dept. of Optoelectronics, University of Ulm, 1996.

[D-3] Sauter, Stephan, *Untersuchungen an mit DFB-Laserdioden integrierten Multiquantum-well-Modulatoren*, Semester Project, Dept. of Optoelectronics, University of Ulm, 1996.

[D-4] Rinke, Titus, *Untersuchung von Mustereffekten und Emissionseigenschaften oberflächenemittierender Laserdioden bei Modulation mit 3 Gbit/s*, Semester Project, Dept. of Optoelectronics, University of Ulm, 1996.

[D-5] Meyer, Roman, *Optische und mechanische Verfahren zur Dickenmessung epitaktischer Nitridschichten*, Semester Project, Dept. of Optoelectronics, University of Ulm, 1996.

[D-6] Müller, Steffen, *Untersuchung der thermischen Kopplung von selektiv oxidierten Vertikallasern für Arrayanwendungen*, Semester Project, Dept. of Optoelectronics, University of Ulm, 1996.

[D-7] Golling, Matthias, *Entwicklung und Aufbau breitbandiger Mikrowellenverstärker und Bitmusterregeneratoren für Übertragungsraten von 2.5 Gbit/s*, Semester Project, Dept. of Optoelectronics, University of Ulm, 1996.

[D-8] Zips, Michael, *Elektrochemische Strom- und Wärmeerzeugung aus Biomasse - Eine Systemanalyse*, Diploma Thesis, Dept. of Optoelectronics, University of Ulm, 1996.

[D-9] Stangl, Markus, *Automatisierung der Meßdatenerfassung eines Meßplatzes zur Charakterisierung von Halbleiterlaserverstärkern*, Semester Project, Dept. of Optoelectronics, University of Ulm, 1996.

[D-10] Martin, Ulrich, *Computergesteuerter Meßplatz zur Charakterisierung von Vertikallaserdioden*, Semester Project, Dept. of Optoelectronics, University of Ulm, 1996.

[D-11] Koerbler, Ulrich, *Charakterisierung hochreflektierender Spiegel mittels Finesse-Messung*, Semester Project, Dept. of Optoelectronics, University of Ulm, 1996.

[D-12] Lehmann, Bernd, *Untersuchung der Rückwirkungseigenschaften von Vertikallaserdioden bei Übertragung von 2.5 Gbit/s Datenraten*, Diploma Thesis, Dept. of Optoelectronics, University of Ulm, 1996.

[D-13] Joos, Jürgen, *Herstellung und Charakterisierung von InAlGaAs/GaAs Hochleistungslaserdioden*, Diploma Thesis, Dept. of Optoelectronics, University of Ulm, 1996.

[D-14] Bidenbach, Reiner, *Untersuchungen zur direkten Verbindung von Halbleitern für optoelektronische Bauelemente*, Diploma Thesis, Dept. of Optoelectronics, University of Ulm, 1996.

[D-15] Keim, Thomas, *Spektrale Simulation des Sonnenlichtes*, Diploma Thesis, Zentrum für Sonnenenergie- und Wasserstoff-Forschung Baden-Württemberg, Stuttgart, 1996.

[D-16] Buck, Martin, *Untersuchung der Hochfrequenzeigenschaften hydrolytisch oxidierter Vertikallaserdioden*, Diploma Thesis, Dept. of Optoelectronics, University of Ulm, 1996.

[D-17] Sauter, Stephan, *Modellierung und Messung des thermischen Widerstandes von Vertikalresonator-Laserdioden*, Diploma Thesis, Dept. of Optoelectronics, University of Ulm, 1996.

[D-18] Tarin, Christina, *Digitale Video- und Datenübertragung*, Diploma Thesis, Dept. of Optoelectronics, University of Ulm, 1996.

[D-19] Thies, Achim, *Molekularstrahlepitaxie und Charakterisierung von nitridischen Verbindungshalbleitern*, Diploma Thesis, Dept. of Optoelectronics, University of Ulm, 1996.

[D-20] Engel, Robert, *Untersuchungen zum Emissionsverhalten von Mikroresonator-Leuchtdioden*, Diploma Thesis, Dept. of Optoelectronics, University of Ulm, 1996.

[D-21] Beierlein, Tilman, *Photoinduziertes, naßchemisches Ätzen von Galliumnitrid*, Semester Project, Dept. of Optoelectronics, University of Ulm, 1996.

[D-22] King, Roger, *Untersuchung der Rauscheigenschaften hydrolytisch oxidierter Vertikallaserdioden unter hochbitratiger Modulation*, Diploma Thesis, Dept. of Optoelectronics, University of Ulm, 1996.

[D-23] Wagner, Wolfgang, *Charakterisierung und Untersuchung von optischen Halbleiterlaserverstärkern auf InAlGaAs/GaAs-Basis*, Diploma Thesis, Dept. of Optoelectronics, University of Ulm, 1996.

[D-24] Schmid, Joachim, *Aufbau und Untersuchung von optischen Glasfaserverbindungsstrecken mit Vertikallaserdioden*, Semester Project, Dept. of Optoelectronics, University of Ulm, 1996.

[D-25] Korhon, Raimond, *Charakterisierung eines 10-Bit breiten parallelen optischen Datenbusses*, Semester Project, Dept. of Optoelectronics, University of Ulm, 1996.

[D-26] Zick, Werner, *Untersuchung der Emissionseigenschaften von oxidierten Laserdioden mit Vertikalresonator im* $Al_yGa_{1-y}As$ *Materialsystem*, Diploma Thesis, Dept. of Optoelectronics, University of Ulm, 1996.

[D-27] Rotter, Thomas, *Charakterisierung und Design von nitridischen III/V-Heterostrukturen im Hinblick auf Leuchtdioden*, Diploma Thesis, Dept. of Optoelectronics, University of Ulm, 1996.

Talks and Seminars

[T-1] H. Y. A. Chung, D. Sowada, T. Wipijewski, G. Stareev and K. J. Ebeling, "Epitaxial growth of highly strained InAsP/InGaP MQWs with GSMBE", *Talk at the National MBE Workshop*, Frankfurt a.d. Oder, Germany, 1996.

[T-2] A. Pelzmann, M. Mayer, C. Kirchner, T. Rotter, D. Sowada, M. Kamp and K. J. Ebeling, "Structural defects in GaN on c-oriented sapphire", *European GaN Workshop (EGW-1)*, Rigi, Switzerland, 1996.

[T-3] M. Kamp, M. Mayer, A. Pelzmann and K. J. Ebeling, "On surface cracking of ammonia for MBE growth of GaN", *IBM T. J. Watson Research Center*, New York, USA, Dec. 1996.

[T-4] M. Kamp, "Current Status on Group III-Nitrides in Europe", *Electronical Society Meeting*, Los Angeles, USA, May 1996.

[T-5] M. Kamp, M. Mayer, A. Pelzmann and K. J. Ebeling, "Ammonia for GaN MBE: How does it work", *International Workshop on GaN*, St. Louis, USA, Mar. 1996.

[T-6] H. Y. A. Chung, D. Sowada, G. Stareev, J. Mähnß and K. J. Ebeling, "Gas-Source MBE von alternierend tensil/kompressiv verspannten InGaP/InAsP MQWs", *11. DGKK-Arbeitskreis*, Marburg, Germany, Dec. 1996.

[T-7] C. Kirchner, A. Pelzmann, M. Mayer, M. Schauler, F. Eberhard, M. Kamp and K. J. Ebeling, "Eigenschaften von GaN pn-Dioden", *11. DGKK-Arbeitskreis*, Marburg, Germany, Dec. 1996.

[T-8] D. Sowada, H. Y. A. Chung, M. Grabherr, B. Weigl, T. Wipiejewski and K. J. Ebeling, "Oxidation aluminiumhaltiger Halbleiterschichten für Laseranwendungen", *11. DGKK-Arbeitkreis*, Marburg, Germany, Dec. 1996.

[T-9] B. Weigl, "Protonenimplantierte und lateral oxidierte Laserdioden mit Vertikalresonator", *DFG-Kolloquium'96, Optische Signalverarbeitung*, Jena, Germany, Mar. 5/6, 1996.

[T-10] C. Jung, M. Grabherr, B. Weigl, G. Reiner and K. J. Ebeling, "Herstellung von effizienten VCSELn durch hydrolytische Oxidation von AlGaAs/AlAS-Schichten", *BMBF-Arbeitskreis*, Jena, Germany, Mar. 1996.

[T-11] A. Pelzmann, M. Mayer, M. Kamp, K. J. Ebeling, H. Teisseyre, G. Nowak, S. Porowski and G. Karczewski, "Eigenschaften homoepitaktischer GaN-Schichten", *11. DGKK-Arbeitskreis*, Marburg, Germany, Dec. 1996.

[T-12] A. Thies, M. Mayer, A. Pelzmann, T. Rotter, M. Kamp and K. J. Ebeling, "GaN Epitaxie mit NH_3 in der GSMBE", *HL 30.70 Frühjahrstagung der DPG*, Regensburg, Germany, 1996, p. 1556.

[T-13] T. Rotter, A. Pelzmann, M. Mayer, A. Thies, C. Kirchner, M. Kamp and K. J. Ebeling, "Optische, kristallographische und elektrische Eigenschaften von Gruppe III-Nitriden", *HL 30.71, Frühjahrstagung der DPG*, Regensburg, Germany, 1996, p. 1557.

[T-14] M. Kamp, M. Mayer, A. Pelzmann, M. Schauler, P. Unger and K. J. Ebeling, "Molekularstrahlepitaxie von GaN Strukturen für Bauelementanwendungen", *Photonik Symposium der Volkswagen Stiftung*, Schwäbisch Hall, Germany, Oct. 1996.

[T-15] P. Unger, "Halbleiterdiodenlaser für hohe optische Leistungen", *Kolloquium "III-V Halbleitertechnologie" der Technischen Universität München*, Munich, Germany, Jan. 12, 1996.

[T-16] P. Unger, "Introduction to Diode Lasers", *Winter College on New Laser Sources*, Trieste, Italy, Feb. 14, 1996.

[T-17] P. Unger, "High power diode lasers", *Winter College on New Laser Sources*, Trieste, Italy, Feb. 16, 1996.

[T-18] P. Unger, "Hochleistungsdiodenlaserverstärker auf der Basis von InAlGaAs / GaAs", *2. Jahrestagung für Hochleistungsdiodenlaser und diodengepumpte Festkörperlaser*, Freiburg i.Br., Germany, Mar. 26, 1996.

[T-19] P. Unger, "Halbleiterdiodenlaser mit hoher optischer Ausgangsleistung", *Philips Forschungslaboratorium*, Aachen, Germany, May 10, 1996.

[T-20] P. Unger, "Halbleiterlaserdioden als effiziente Lichtquellen mit hoher optischer Ausgangsleistung", *Antrittsvorlesung an der Universität Ulm*, Ulm, Germany, June 26, 1996.

[T-21] P. Unger, "Optoelektronik", *7. Unternehmertag, Wissenschaftsstadt Ulm*, Ulm, Germany, Oct. 11, 1996.

Publications and Conference Contributions

[P-1] Z. Dai, R. Michalzik, P. Unger and K. J. Ebeling, "Impact of the residual facet reflectivity on beam profile filamentation in semiconductor laser amplifiers", in *Proc. Conf. on Lasers and Electro-Optics (CLEO'96), Paper CThK32*, Anaheim, CA, USA, 1996, pp. 416–417.

[P-2] Z. Dai, R. Michalzik, P. Unger and K. J. Ebeling, "Modeling of high-power semiconductor laser amplifiers with residual reflectivity", in *Proc. Progress in Electromagn. Res. Symp., PIERS'96*, Innsbruck, Austria, 1996, p. 82.

[P-3] Z. Dai and K. J. Ebeling, "Numerical simulation of large-area, high-power semiconductor laser amplifiers", submitted to *J. Quantum Electron.*, 1996.

[P-4] Z. Dai and P. Unger, "Simulation of beam profile filamentation in high-power semiconductor amplifier", in *Proc. Conf. on Lasers and Electro-Optics Europe (CLEO'96 Europe), Paper CThI30*, Hamburg, Germany, 1996, p. 266.

[P-5] K. J. Ebeling, B. Weigl, G. Reiner, U. Fiedler, R. Michalzik, C. Jung, D. Wiedenmann, P. Schnitzer and M. Grabherr, "Highly efficient vertical cavity laser diodes", in *Proc. Int. Quantum Electron. Conf.*, Sydney, Australia, 1996.

[P-6] K. J. Ebeling, U. Fiedler, R. Michalzik, G. Reiner and B. Weigl, "Efficient vertical cavity surface emitting laser diodes for high bit rate optical data transmission", *Int. J. Electron. Commun.*, vol. 50, pp. 316–326, June 1996.

[P-7] K. J. Ebeling, U. Fiedler, R. Michalzik, G. Reiner and B. Weigl, "Recent advances in semiconductor vertical cavity lasers for optical communications and optical interconnects", in *Proc. 22nd Europ. Conf. on Opt. Comm., invited*, Oslo, Norway, 1996, vol. 2, pp. 81–88.

[P-8] K. J. Ebeling, B. Möller, G. Reiner, U. Fiedler, R. Michalzik, B. Weigl, C. Jung and E. Zeeb, "Vertical cavity laser diodes and arrays for efficient fiber coupling and high speed data transmission in optical interconnects", in *Proc. 12th Int. Congress Laser 95: Laser in Research and Engineering.* 1996, pp. 783–794, Springer-Verlag, Berlin, Heidelberg, New York.

[P-9] U. Fiedler, B. Weigl, G. Reiner and K. J. Ebeling, "Noise behavior of sub mA threshold single-mode oxidized VCSELs", in *Proc. Conf. on Lasers and Electro-Optics Europe (CLEO'96 Europe)*, Hamburg, Germany, 1996, p. 13.

[P-10] U. Fiedler, B. Weigl, G. Reiner, B. Lehmann and K. J. Ebeling, "2.5 Gbit/s data link using oxidized sub mA threshold VCSELs", in *Proc. 22nd Europ. Conf. on Opt. Comm.*, Oslo, Norway, 1996, vol. 2, pp. 101–104.

[P-11] U. Fiedler, B. Weigl, G. Reiner, R. King and K. J. Ebeling, "Modal noise in 2.5 Gbit/s data links with oxidized VCSELs", in *Proc. LEOS 9th Annual Meeting*, Boston, USA, 1996, vol. 2, pp. 71–72.

[P-12] U. Fiedler, D. Wiedenmann, B. Weigl, C. Jung, G. Reiner, M. Buck and K. J. Ebeling, "High frequency behavior of oxidized single-mode single polarisation with elliptical current aperture", in *Proc. LEOS 9th Annual Meeting*, Boston, USA, 1996, vol. 1, pp. 211–212.

[P-13] U. Fiedler, D. Wiedenmann, B. Weigl, C. Jung, G. Reiner, M. Buck and K. J. Ebeling, "Stable linearly polarized light emission from VCSELs with oxidized elliptical current aperture", in *Proc. 15th Int. Semiconductor Laser Conf.*, Haifa, Israel, 1996, pp. 19–20.

[P-14] U. Fiedler, G. Reiner, P. Schnitzer and K. J. Ebeling, "Top surface-emitting vertical-cavity laser diodes for 10 Gbit/s data transmission", *IEEE Photon. Technol. Lett.*, vol. 8, pp. 746–748, 1996.

[P-15] U. Fiedler, G. Reiner, P. Schnitzer, D. Wiedenmann and K. J. Ebeling, "Höchstbitratige optische Kurzstreckenverbindungen mit Vertikallaserdioden", *Forschungsvorhaben MITI/NEDO*, 1996.

[P-16] M. Grabherr, B. Weigl, G. Reiner and K. J. Ebeling, "Comparison of proton implanted and selectively oxidized vertical-cavity surface-emiting lasers", in *Proc. Conf. on Lasers and Electro-Optics Europe (CLEO'96 Europe)*, Hamburg, Germany, Sept. 1996, p. 64.

[P-17] M. Grabherr, B. Weigl, G. Reiner, M. Miller and K. J. Ebeling, "High power top-surface emitting vertical-cavity lasers", in *Proc. LEOS 1996*, Boston, USA, 1996, vol. 1, pp. 203–204.

[P-18] M. Grabherr, B. Weigl, G. Reiner, M. Miller and K. J. Ebeling, "High power top-surface emitting oxide confined vertical-cavity laser diodes", *Electron. Lett.*, vol. 23, no. 18, pp. 1723, 1996.

[P-19] J. Heerlein, G. Jost, J. Joos, S. Morgott, G. Reiner and P. Unger, "Broad-area InGaAs/AlGaAs quantum well lasers with high efficiency", in *Proc. Conf. on Lasers and Electro-Optics Europe (CLEO'96 Europe)*, Hamburg, Germany, Sept. 1996, p. 266.

[P-20] C. Jung, W. Schmid, B. Weigl, G. Reiner, R. Michalzik and K. J. Ebeling, "Delayed self-heterodyne linewidth measurements of vertical-cavity surface-emitting laser diodes", in *Proc. Conf. on Lasers and Electro-Optics Europe (CLEO'96 Europe)*, Hamburg, Germany, 1996, p. 64.

[P-21] M. Kamp and K. J. Ebeling, "Europe's status in group III-nitrides", *Compound Semiconductor*, pp. 22–23, Sept./Oct. 1996.

[P-22] M. Kamp, M. Mayer, A. Pelzmann, A. Thies, H. Y. Chung, H. Sternschulte, O. Marti and K. J. Ebeling, "NH_3 as Nitrogen source in MBE growth of GaN", *Mat. Res. Symp. Proc., vol. 395, Material Research Society*, pp. 135–139, 1996.

[P-23] M. Kamp, M. Mayer, A. Pelzmann and K. J. Ebeling, "On surface cracking of ammonia for MBE growth of GaN", *Mat. Res. Soc. Symp. Proc.*, vol. 449, 1996.

[P-24] M. Kamp, M. Mayer and A. Pelzmann, "Photoluminiscence study on GaN homoepitaxial layers grown by molecular beam epitaxy", *Nitride Semiconductor Journal, MRS Proceeding*, 1996.

[P-25] R. Michalzik and K. J. Ebeling, "Comparative study of selectively oxidized short and long wavelength vertical-cavity surface-emitting laser diodes", in *Proc. Progress in Electromagn. Res. Symp., PIERS'96*, Innsbruck, Austria, July 1996, p. 214.

[P-26] R. Michalzik, G. Reiner, B. Weigl, U. Fiedler and K. J. Ebeling, "High efficiency VCSELs for optical interconnect applications", in *Proc. Engeneering Foundation Conference on High Speed Opto-Electronic Devices and Systems*, Snowbird, Utha, USA, Aug. 1996.

[P-27] M. Mayer, A. Pelzmann, M. Kamp and K. J. Ebeling, "Photoluminiscence study on GaN homoepitaxial layers grown by molecular beam epitaxy", *MRS Internet Journal, Nitride Semiconductor Research*, vol. 1, art. 13, 1996.

[P-28] M. Mayer, A. Pelzmann, M. Kamp, K. J. Ebeling, H. Teisseyre, G. Novak, M. Leszczynski, I. Grzegory, M. Bochowski, S. Krukowski, B. Lucznik, S. Porowski and G. Karczewski, "Homoepitaxial GaN layers grown by molecular beam epitaxy", submitted to *Appl. Phys. Lett.*, 1996.

[P-29] M. Albrecht, S. Christiansen, H.P. Strunk, C. Zanotti-Fregonara, G. Salriati, M. Mayer, A. Pelzmann, M. Kamp, and K.J. Ebeling, "Luminesence related to stacking faults in GaN/Al_2O_3 (0001)", submitted to *Phys. Rev. B*, 1996.

[P-30] P. Michler, M. Hilpert and G. Reiner, "Dynamics of dual-wavelength emission from a coupled semiconductor microcavity laser", submitted to *Appl. Phys. Lett.*, 1996.

[P-31] A. Pelzmann, M. Mayer, C. Kirchner, D. Sowada, T. Rotter, M. Kamp and K. J. Ebeling, "Determination of the dislocation densities in GaN on c-oriented sapphire", *MRS Internet Journal, Nitride Semiconductor Research*, vol. 1, art. 40, 1996.

[P-32] S. Christiansen, W. Dorsch, H-P. Strunk, A. Pelzmann, M. Mayer, M. Kamp and K.J. Ebeling, "Microstructure and growth morphology as related to electrooptical proberties of heteroepitaxial wurzite GaN on sapphire (0001) substrate", *Mat. Science and Technology B,* accepted, 1996.

[P-33] A. Pelzmann, S. Strite, A. Domman, C. Kirchner, M. Kamp, and K.J. Ebeling, "Improved optical activations of ion-implanted Zn acceptors in GaN by annealing under N_2 overpressure", in *European GaN Workshop*, Rigi, Switzerland, 1996.

[P-34] S. Christiansen, M. Albrecht, W. Dorsch, H. P. Strunk, C. Zanolti-Fregonara, G. Salviati, A. Pelzmann, M. Mayer, M. Kamp and K. J. Ebeling, "Microstructure, growth mechanisms and electro-optical properties of heteroepitaxial GaN layers on sapphire (0001) substrates", *MRS Internet Journal, Nitride Semiconductor Research*, vol. 1, art. 19, 1996.

[P-35] G. Reiner, B. Weigl, M. Grabherr and K. J. Ebeling, "High performance MBE-grown top surface-emitting vertical-cavity laser diodes", in *Proc. Int. Conf. on MBE*, 1996.

[P-36] W. Schmid, C. Jung, B. Weigl, G. Reiner, R. Michalzik and K. J. Ebeling, "Delayed self-heterodyne linewidth measurement of VCSELs", *IEEE Photon. Technol. Lett.*, vol. 8, no. 10, pp. 1288–1290, Oct. 1996.

[P-37] P. Schnitzer, U. Fiedler, M. Grabherr, C. Jung, G. Reiner, W. Zick and K. J. Ebeling, "Bias-free 1 Gbit/s data transmission using single-mode GaAs VCSELs at λ= 835 nm", *Electron. Lett.*, vol. 32, no. 23, pp. 2145–2146, Nov. 1996.

[P-38] P. Schnitzer, U. Fiedler, M. Grabherr, G. Reiner, B. Weigl, C. Tarin and K. J. Ebeling, "2.5 Gbit/s data rate transmission using low threshold GaAs (λ=830 nm) VCSELs", in *Proc. LEOS*, Boston, USA, 1996, vol. 2, pp. 73–74.

[P-39] D. Sowada, H. Y. A. Chung, M. Grabherr, B. Weigl, T. Wipiejewski and K. J. Ebeling, "Oxidation of InAlAs for long wavelength vertical-cavity laser diodes", in *Proc. Conf. on Lasers and Electro-Optics Europe (CLEO'96 Europe)*, Hamburg, Germany, Sept. 1996, p. 342.

[P-40] G. Stareev, A. Balter, Gawrilow and D. Sowada, "Laser excited fluorescence of perylene by using self-induced second-harmonic and sumfrequency radiation emanating from high-power AlGaAs double hetero-type diodes", *Appl. Phys. B62*, pp. 557–561, 1996.

[P-41] H. Teiseyre, G. Novak, M. Leszczynski, I. Grzegory, M. Bockowski, S. Kruhowski, S. Porowski, M. Mayer, A. Pelzmann, M. Kamp, K. J. Ebeling and G. Karczewski, "Photoluminiscence study on GaN homoepitaxial layers grown by molecular beam epitaxy", *MRS Internet Journal, Nitride Semiconductor Research*, vol. 1, art. 13, 1996.

[P-42] T. Wipiejewski, D. B. Young, B. J. Thibeault and L. A. Coldren, "Thermal crosstalk in 4x4 vertical-cavity surface-emitting laser arrays", *IEEE Photon. Technol. Lett.*, pp. 980–982, Aug. 1996.

[P-43] T. Wipiejewski, J. Ko, B. J. Thibeault and L. A. Coldren, "Molecular beam epitaxy regrowth of top reflectors for multiple wavelength vertical-cavity laser arrays", in *Proc. Conf. on Lasers and Electro-Optics (CLEO'96)*, Anaheim, CA, USA, June 1996, pp. 362–363.

[P-44] T. Wipiejewski, J. Ko, B. J. Thibeault and L. A. Coldren, "Multiple wavelength vertical-cavity laser array employing molecular beam epitaxy regrowth", *Electron. Lett.*, vol. 32, pp. 340–342, 1996.

[P-45] T. Wipiejewski, J. Ko, B. J. Thibeault, D. B. Young and L. A. Coldren, "2D vertical-cavity laser arrays for free-space and multimode fiber transmission systems", in *Proc. 46th ECTC*, Orlando, FL, USA, May 1996, pp. 1130–1135.

[P-46] T. Wipiejewski, M. G. Peters, B. J. Thibeault, D. B. Young and L. A. Coldren, "Size dependent output power saturation of vertical-cavity surface-emitting laser diodes", *IEEE Photon. Technol. Lett.*, vol. 8, pp. 10–12, 1996.

[P-47] T. Wipiejewski, M. G. Peters, D. B. Young, B. J. Thibeault, G. A. Fish and L. A. Coldren, "Thermal resistance of etched-pillar vertical-cavity surface-emitting laser diodes", in *Proc. SPIE Int. Symposium, Optoelctronic Packaging*, San Jose, USA, Jan. 1996.

[P-48] B. Weigl and K. J. Ebeling (Optoelectronics Department), I. Hörsch, R. Kusche and O. Marti, "Spectrally resolved near-field mode imaging of vertical cavity semiconductor lasers", *J. Appl. Phys. 79 (8)*, pp. 3831–3834, Apr. 1996.

[P-49] B. Weigl, G. Reiner, M. Grabherr and K. J. Ebeling, "High-power selectively oxidized vertical-cavity surface-emitting lasers", in *Proc. Conf. on Lasers and Electro-Optics (CLEO'96)*, Anaheim, CA, USA, 1996, p. 204.

[P-50] B. Weigl, G. Reiner, M. Grabherr and K. J. Ebeling, "Highly efficient selectively oxidized GaAs (λ = 830 nm) vertical-cavity lasers", in *Int. Semiconductor Laser Conf.*, Haifa, Israel, 1996, p. 81.

[P-51] B. Weigl, G. Reiner, M. Grabherr and K. J. Ebeling, "Oxidised GaAs QW vertical-cavity lasers with 40 % power conversion efficiency", *Electron. Lett.*, vol. 32, pp. 1784–1786, 1996.

[P-52] B. Weigl, M. Grabherr, C. Jung, R. Jäger, G. Reiner, R. Michalzik, D. Sowada and K. J. Ebeling, "High performance oxide confined GaAs VCSELs", submitted to *IEEE J. of Selected Topics in Quantum Electron.*, 1996.

[P-53] B. Weigl, M. Grabherr, G. Reiner and K. J. Ebeling, "CW operation of selectively oxidized vertical-cavity surface-emitting lasers from -80 C to 130 C", in *Proc. Conf. on Lasers and Electro-Optics Europe (CLEO'96 Europe)*, Hamburg, Germany, Sept. 1996, p. 27.

[P-54] B. Weigl, M. Grabherr, G. Reiner and K. J. Ebeling, "High efficiency selectively oxidised MBE grown vertical-cavity surface-emitting lasers", *Electron. Lett.*, vol. 32, no. 6, pp. 557–558, 1996.

[P-55] B. Weigl, M. Grabherr, R. Jäger, G. Reiner and K. J. Ebeling, "57 % wallplug efficiency wide temperature range 840 nm wavelength oxide confined GaAs VCSELs", in *Proc. 15th Int. Semiconductor Laser Conf., postdeadline paper PDP2*, Haifa, Israel, 1996.

[P-56] B. Weigl, M. Grabherr, R. Michalzik, G. Reiner and K. J. Ebeling, "High power single-mode selectively oxidized verical-cavity surface-emitting lasers", *IEEE Photon. Technol. Lett.*, vol. 8, pp. 971–973, 1996.

[P-57] D. Wiedenmann, B. Möller, R. Michalzik and K. J. Ebeling, "Performance characteristics of vertical-cavity semiconductor laser amplifiers", *Electron. Lett.*, vol. 32, no. 4, pp. 342–343, 1996.

[P-58] D. Wiedenmann, R. Michalzik, B. Möller and K. J. Ebeling, "Static and dynamic characteristics of vertical-cavity semiconductor laser amplifiers", in *Proc. Conf. on Lasers and Electro-Optics (CLEO'96)*, Anaheim, CA, USA, 1996, p. 518.

[P-59] Z. Dai, P. Unger and K. J. Ebeling, "Numerical simulation of tapered semiconductor laser amplifiers", in *Conf. on Laser and Electro-Optics 1997 (CLEO'97)*, submitted, Baltimore, USA, 1997.

[P-60] R. Jäger, M. Grabherr, C. Jung, R. Michalzik, G. Reiner, B. Weigl and K. J. Ebeling, "57 % Wallplug efficiency oxide-confined 850 nm wavelength GaAs VCSELs", *Electron. Lett.*, vol. 33, pp. 330–331, 1997.

[P-61] R. Michalzik, B. Weigl, G. Reiner, M. Grabherr and K. J. Ebeling, "Realization and modeling of extremely efficient VCSELs", in *Proc. Progress in Electromagn. Res. Symp., PIERS'97, in press*, Hong Kong, Jan. 1997.

[P-62] P. Michler, M. Hilpert and G. Reiner, "Dynamics of dual-wavelength emission from a coupled semiconductor microcavity laser", in *Conf. on Laser and Electro-Optics 1997 (CLEO'97),* submitted, Baltimore, USA, 1997.

[P-63] P. Schnitzer, U. Fiedler, G. Reiner, B. Weigl, W. Zick and K. J. Ebeling, "Bias-free 1 Gbit/s data transmission using top surface-emitting vertical-cavity laser diodes", *IEEE Photon. Technol. Lett.*, 1997, in press.

[P-64] P. Schnitzer, D. Wiedenmann and K. J. Ebeling, "Generation höchstfrequenter Bitraten von 10 Gbit/s mit Verikallaserdioden", in *Proc. MIOP97*, Sindelfingen, Germany, Apr. 1997.

[P-65] P. Schnitzer, M. Grabherr, R. Jäger, C. Jung, R. Michalzik, G. Reiner, B. Weigl, D. Wiedenmann and K. J. Ebeling, "Bias-free 1 Gb/s data transmission using high efficiency VCSELs", in *ECTC'97,* submitted, 1997.

[P-66] D. Wiedenmann, R. Michalzik, P. Schnitzer, U. Fiedler and K. J. Ebeling, "High bit rate data transmission with short wavelength oxidized VCSELs: towards bias-free operation", submitted to *IEEE J. of Selected Topics in Quantum Electron.*, 1997.